Investigations on CdZnTe-Semiconductor-Detectors for the Search of the Neutrinoless Double Beta Decay

Daniel Gehre
Institut für Kern- und Teilchenphysik
Technische Universität Dresden

A thesis submitted for the degree of
Doctor rerum naturalium, Dr. rer. nat.

2017, December

1. Reviewer: Prof. Dr. Kai Zuber, TU Dresden

2. Reviewer: Prof. Claus Gößling, TU Dortmund

Day of the defense:

Signature from head of PhD committee:

Abstract

The Cadmium-Zinc-Telluride 0-Neutrino-Double-Beta Research Apparatus (COBRA-Experiment) investigates the theoretically predicted neutrinoless double beta decay ($0\nu\beta\beta$-decay) to indirectly determine the effective Majorana mass of the electron-neutrino by a measurement of the half-life of the $0\nu\beta\beta$-decay using room-temperature semiconducting Cadmium-Zinc-Telluride-detectors (CZT). The detectors are made of elements containing several isotopes that decay via double beta decay ($\beta\beta$-decay). In such a configuration the detector itself becomes the source of the decay and, hence, the efficiency for the detection of such events rises.

This work covers the investigations and characterizations made on the CZT detectors used in the COBRA-Experiment, currently running. Prior to installation the physical properties of the detectors are analyzed and during operation the stability of the detectors is monitored. For the laboratory analysis three dedicated setups are developed that allow for detailed investigations of different properties of the detectors. Beside the working point determination and the analysis of the temperature dependence of the detector performance, the spatial detector response to localized irradiation is analyzed and a setup to generate a library of specific pulse shapes is designed and operated. Furthermore, an investigation for a possible discrimination of α- and β-decay events based on pulse shape discrimination is performed as well as an analysis of the long term stability of underground operated CZT detectors.

Contents

1 Introduction **1**

2 Theoretical and Methodical Background **5**

2.1 Phenomenological Principles 5

2.1.1 Neutrinos 5

2.1.2 Single Beta Decay 6

2.1.3 Double Beta Decay 8

2.2 The Concept of the COBRA-Experiment 12

2.2.1 CZT in the COBRA-Experiment 12

2.2.2 General Remarks on CZT 16

2.2.3 Single Charge Sensitive Devices 17

2.3 Pulse Shape Analysis on CZT Detectors 23

2.3.1 Anode Side events 23

2.3.2 Single/Multi Site Events 23

2.3.3 Lateral Surface Events 25

3 Investigations on CZT-Detectors for the COBRA-Experiment **29**

3.1 Determination of the Zinc Content 29

3.1.1 Non-destructive Measurements with EDX and XRF 29

3.1.2 Destructive Measurement with ICP-MS 32

3.2 Working Point Determination 34

3.2.1 Experimental Setup for Working Point Determination 34

3.2.2 HV/GB Scanning and weighting factor determination 36

3.2.3 Determination of Total Detector Efficiency 39

3.3 Temperature Scaling Experiments 43

3.3.1 Experimental setup 43
3.3.2 Temperature Dependency of the Mobility-Lifetime-Product . . . 46
3.4 Spatial resolved Analysis of Charge Transport Properties in CZT 53
3.4.1 Experimental Setup for Localized Irradiation 54
3.4.2 2D-Mapping of the Charge Collection Efficiency 57
3.5 Compton Coincidence Experiment 61
3.5.1 Theory and Experimental Setup 61
3.5.2 180° Back-Scattering of ^{60}Co photons 64
3.5.3 Angular Compton Scatter Experiments 66
3.6 Investigations on a possible α/β-Discrimination at the Cathode 68
3.6.1 The Origin of ^{190}Pt and ^{210}Po at the Cathode 68
3.6.2 Analysis of the Pulse Shapes of α- and β-Events 71
3.7 Investigations on the Long-term Stability of Underground Operated CZT Detectors 81
3.7.1 Measurement Strategy 81
3.7.2 Selection Criteria and Measurements 81
3.7.3 Observed ^{113}Cd Decay Rate Variations 84
3.7.4 Results of the Stability Analysis 90

4 Discussion **93**

Bibliography **99**

A The Experimental Setup of the COBRA Demonstrator **113**
A.1 The Laboratori Nazionali del Gran Sasso 113
A.2 Experimental Setup at the LNGS 115
A.3 Shielding of the COBRA Demonstrator Setup 117
A.4 The Electronics of the COBRA Demonstrator Setup 125

B Follow-up Operation of the 2D-Scanning Test Rig **135**
B.1 Analysis of the Localized Detector Response of the COBRA-XDEM Detectors 135
B.2 CCE Mapping of the COBRA-XDEM Detectors 137

1

Introduction

A scientific theory describing a natural phenomenon is only valid until a counter-evidence is presented. That does not mean, that the original theory is generally wrong but adjustments or extensions of this theory may be required. In some cases the 'old' theory must be replaced by a generally new approach, which respects and explains the new observations that can not be described by its predecessor.
The *Newtonian Mechanics* (NM) has dominated physics for more than 200 years and is still valid for most of the everyday mechanical and celestial phenomena [New87]. In 1687 Newton described the movement of planets with surpassing accuracy – until in the 19$^{\text{th}}$ century the precession of the perihelion of Mercury around the Sun was discovered. For a long time the reason for this anomalous behavior was unclear, until in 1915 Einstein explained it by his newly developed *General Theory of Relativity* (GRT) [Ein15]. The development of the GRT was a fundamental step forward in the understanding of the working principle of gravity and replaced NM ever since.
In the 20$^{\text{th}}$ century the Standard Model of particle physics (SM) has proved to be a valid description for the majority of the observed phenomena in nuclear and particle physics. The theoretical construct of the SM is experimentally validated for decades and is the basis of our current understanding of the composition of matter and the basic interactions. Nevertheless, astronomical observations and physical experiments yield results that can not be described by the SM and that require at least an extension of it or – even more likely – the development of a completely new theory: a physics beyond the SM. One reason for such a demand is, that the fundamental force of gravity is not respected in the SM. On microscopic scale the gravitational force is negligible compared to the strong, the weak or the electromagnetic force. But on macroscopic scale astronomical observations result strong hints, that the amount of visible matter in the universe is not sufficient to explain the movement and the cohesion of galaxies. A non-visible, hardly interacting *Dark Matter*, that reveals its presence by gravitational interaction, only, is needed to explain the observed behavior. This *Dark Matter* currently does not exist in the SM.
Another irrefutable proof for a physics beyond the SM is the observation of neutrino oscillations between the different neutrino flavors (section 2.1.1). But the oscillation

process is only possible if neutrinos have a non-vanishing rest-mass and such a requirement is not consistent with the SM, that describes the neutrino to be a massless fermion. In 1937 MAJORANA suggested the existence of fermions that do not carry any charge and are their own antiparticle. This property clearly distinguishes it from the DIRAC–fermions of the SM, that can carry charge and do have an antiparticle. Currently it is not clear, whether neutrinos are MAJORANA– or DIRAC–fermions. One possible way to decide, whether neutrinos are the one or the either, is the proof of the existence of the *neutrinoless double beta decay* ($0\nu\beta\beta$-decay, section 2.1.3). This special β-decay is not accompanied by neutrino emission and is impossible in the SM as the lepton number conservation is violated in the $0\nu\beta\beta$-processes.
Beside the decision wether the neutrino is a MAJORANA– or a DIRAC–fermion, another major question of modern physics could be answered by the measurement of a half-life of any $0\nu\beta\beta$-decay. The measurement of the half-life of this decay would allow to determine the absolute mass of the neutrinos. Currently, the experimentally determined upper limit for the electron-antineutrino mass is given with $m_{\bar{\nu}_e} < (0.15..0.33)\,\mathrm{eV/c^2}$ [Col17] which is consistent with cosmological observations that claim, that the sum of the mass of all neutrino flavors must be less than $\sum m_{\nu_i} < 0.3\,\mathrm{eV/c^2}$ [GHMT06]. The measurement of either neutrino mass would directly determine the mass of the other two neutrino flavors as the relative mass ratios between the three flavors are known. Therefore, the process of $0\nu\beta\beta$-decay is of great relevance in modern physics and is searched for approximately 50 years in many experiments worldwide. Even though there are reports for the discovery of $0\nu\beta\beta$-decay [KKDB$^+$01] newer results disapprove this claim [Col17].
The known specifics of the $0\nu\beta\beta$-decay make it a very rare process with half-lives well in the $T_{1/2} > 10^{25}\,\mathrm{yr}$ region and beyond. To measure such long half-lives the experimental requirements are extraordinary but can be recapped to two fundamental demands. First: due to the long half-life of it, a huge number of potential decaying source atoms under investigation is required. Secondly, in order to be sure that the observed decay is the desired one, the measurement must be free of background contributions in the presumed area.
For that search different experimental approaches are in use. In the conventional setup a sample of the decaying material is put next to a detector that is triggered by the emitted particles. In $0\nu\beta\beta$-decay the searched particles are mainly electrons or positrons that have a limited range in matter and must be detected with their initial energy, ideally. Therefore, the source thickness is very limited, which rises problems to the requirement for a large number of potential source atoms.
For $0\nu\beta\beta$-decay searches the more efficient way is to make the detector itself the source of the decay. Almost all currently running and future planned $0\nu\beta\beta$-decay experiments are based on this approach. The big advantage of this detector-equals-source approach is, that the efficiency for the detection of the searched signals is increased substantially. The limited range of the particles that are emitted in the $0\nu\beta\beta$-process, allows to increase the size of the detector with basically no limitation and to increase the number of potential source atoms, accordingly. Once a certain detector size is reached, it is not

of relevance anymore if the experiment is formed from a single huge detector or if it is assembled of a large number of single sub-detectors. Both concepts have their own advantages and drawbacks and it is not possible to prefer the one or the other. For $0\nu\beta\beta$-decay search three concepts with the detector-equals-source approach are in use. They are based on the scintillation of liquids, the bolometric measurement of energy depositions in cooled crystals or the calorimetric measurement of particle interactions in semiconducting devices.

Currently, the physically largest setup for $0\nu\beta\beta$-search is the SNO+ experiment that makes use of the scintillation of organic liquids [Seg16]. In this experiment the $\beta\beta$-decaying isotope is dissolved in the observed liquid. The scintillation light is generated by recombination processes in the liquid after ionization processes that are caused by particles from the radioactive decay. The detection of the scintillation light is performed by photomultipliers that are installed outside of the vessel. This allows to construct a huge detector that can contain many tons of the isotope of interest. The self shielding setup screens external radiation and can be used as a veto-system to suppress unwanted signals. Statistical analysis enables to differentiate between $\beta\beta$-signals and interactions of background contributions. The main drawback of the scintillation based experiments is the limited energy resolution. This is problematic as it is needed to separate the unavoidable $2\nu\beta\beta$-background from the searched $0\nu\beta\beta$-signals (section 2.1.3). Nevertheless, the huge amount of source atoms and, hence, the expected good statistic is a clear benefit of this approach.

In contrast to the scintillation based measurements, the bolometric measurement of energy depositions is a method with superior energy resolution. In bolometric setups a crystal, that contains the isotope of interest, is cooled down to milli-Kelvin temperatures. The energy released in the $\beta\beta$-decay is deposited in the crystal and heats it up by energy dissipation. The change in temperature causes a well measurable change in resistivity which is the root cause for the excellent energy resolution. This approach is realized in the CUORE experiment [A$^+$16a]. The main drawback of this approach is that the size of the crystals is technically and physically limited to assure the surpassing energy resolution, but, as described above, the detector can be assembled from many sub-detectors which allows to construct a large scale experiment, too. Another restriction is the limited size of the isolating cryostat and the necessary holding structures for the crystals. The cryostat and the supports need to be made from ultra pure materials to assure the low background needed for $\beta\beta$-research.

The third method to measure the emitted particles of the $\beta\beta$-decay is the use of semiconducting devices. Semiconductors are widely used as radiation detectors and the processes happening in the detectors are well understood. The most common semiconducting detector material for highly efficient detection of ionizing radiation is germanium. The low bad gap of germanium requires a continuous liquid nitrogen cooling of the detector. Germanium has a $\beta\beta$-decaying isotope that makes it a great material for $0\nu\beta\beta$-search. It is used in many experiments, such as GERDA [AAB$^+$16] or MAJORANA [EGG$^+$11]. The detection is caused by an ionization processes in the detector crystal and by energy equivalent charge transport to attached preamplifiers. The draw-

back is that the necessary enrichment of the isotope of interest for the manufacturing of the high purity germanium detectors for $0\nu\beta\beta$-search is extremely costly and the operation in the needed cryostat is complex.
Another very promising candidate for $0\nu\beta\beta$-search is Cadmium-Zinc-Telluride (CZT). CZT is a further development of CdTe, which was reported as γ-detector for the first time in 1967 by Akutagawa et. al. [AZM67]. At this time CdTe suffered from very poor charge transport properties and it was hardly possible to detect full energy deposition of α-interactions. During the optimization of the production process of CdTe it was found, that the addition of a few percent of zinc to CdTe results in increased bulk resistivity and a wider band gap of the compound. Both properties are crucial for the operation at room-temperature. Additionally, the increased bulk resistivity reduced the electronic noise of the detectors, which led to improved energy resolution. First reports of the use of CZT as radiation detector can be found in [CZT93].
CZT got in the focus of $0\nu\beta\beta$-search activities, as it contains a total of nine $\beta\beta$-decaying isotopes (section 2.2.1). This property enables CZT for the above described detector-equals-source approach, too. The great advantage of CZT over germanium is the higher mean atomic number and density, which leads to better absorption of ionizing radiation, and the wider band gap, that allows for the operation at room temperature. Although the manufacturing of CZT is tricky, it is also a self-purifying process, that ensures great radiopurity and, hence, low intrinsic background – a major requirement for $0\nu\beta\beta$-search. However, due to the complex phase diagram of this ternary compound, the manufacturing of CZT is still challenging. The main problems are the different melting points of the three constituents and the ionic binding of the crystal lattice. Therefore, even small disturbances during the crystal growth can result in the formation of precipitates or lattice defects that affect the detector performance. Despite the achieved improvements in large scale manufacturing of CZT, still every boule is unique and each detector sliced from it has its specific properties.
Currently, the COBRA-experiment [Zub01] is the only $\beta\beta$-experiment that makes use of CZT detectors. The COBRA Demonstrator setup is assembled out of $64\times1\,\mathrm{cm}^3$ detectors in CoPlanar Grid configuration (section 2.2.3). Due to the limited size of the CZT crystals, a large scale COBRA setup would be assembled out of many sub-detectors, too. This is not necessarily a drawback, as it allows for advanced background analysis of external radiation or for the analysis of radiative deexcitation of $\beta\beta$-decays to excited states, depositing energy in adjacent detectors.
This work describes the investigations that are performed at the COBRA Demonstrator detectors prior installation. For these investigations three different experimental setups were developed, manufactured and operated at the Technische Universität Dresden. All detectors of the currently running COBRA Demonstrator setup are characterized for their specific working points, their total efficiencies and their spatial detector response. Furthermore, a possibility to differentiate α- from β-interactions based on pulse shape analysis is investigated. Finally, the operation of the detectors in the COBRA Demonstrator setup was monitored for more than 3 years and the long-term stability of the detectors is analyzed.

2

Theoretical and Methodical Background

2.1 Phenomenological Principles

2.1.1 Neutrinos

Since their postulation in 1930 by Pauli, neutrinos are exceptional members of the particle zoo [Pau30]. Initially a theoretical construct to preserve the law of energy conservation in β-decay, it took more than 25 years until Reines and Cowan proved their existence experimentally. In 1955 they performed an experiment next to a nuclear reactor, that emitted huge amounts of electron anti-neutrinos. For their experiment the inverse β-decay (section 2.1.2)

$$\bar{\nu}_e + p \longrightarrow e^+ + n \tag{2.1}$$

was used. The identification of the reaction was performed by detecting prompt positron annihilation radiation of two photons with an energy of $E_\gamma = 511\,\mathrm{keV}$ and the delayed deexcitation radiation of $^{114}\mathrm{Cd}^*$, originating from the neutron capture reaction of $^{113}\mathrm{Cd(n,}\gamma)^{114}\mathrm{Cd}^*$. Due to the huge cross-section of ^{113}Cd for this reaction, with $\sigma_{(n,\gamma)} = 20\,\mathrm{kbarn}$ and the intense deexcitation radiation, ^{113}Cd was well suited for this investigation [RC56].
Neutrinos are probably the most abundant particles in the universe but still many of their properties are unknown, such as if they carry a magnetic moment or if sterile neutrinos exist. In the standard model of particle physics (SM) neutrinos are assumed to be massless fermions. They occur in three doublets, each with charged leptonic and anti-leptonic partners.

$$\begin{pmatrix}\nu_e\\ e^-\end{pmatrix}\begin{pmatrix}\nu_\mu\\ \mu^-\end{pmatrix}\begin{pmatrix}\nu_\tau\\ \tau^-\end{pmatrix} \mathit{and} \begin{pmatrix}\bar{\nu}_e\\ e^+\end{pmatrix}\begin{pmatrix}\bar{\nu}_\mu\\ \mu^+\end{pmatrix}\begin{pmatrix}\bar{\nu}_\tau\\ \tau^+\end{pmatrix} \tag{2.2}$$

Each family has a fixed and conserved lepton-number $L_{e,\mu,\tau} = 1$ and $L_{e^+,\mu^+,\tau^+} = -1$. In the SM the transformation of particles between the families is not allowed. The particles and their anti-particles are bi-unique and distinguishable [Sch97].
Already in 1957 PONTECORVO suggested neutrino oscillation between neutrino ν and anti-neutrino $\bar{\nu}$, as which later turned out not being true [Pon57]. In 1962 MAKI, NAKAGAWA and SAKATA began to theoretically investigate neutrino oscillation between different lepton families, such that a relation between Mass-Eigenstates $|\nu_i\rangle$ $(i = 1, 2, 3)$ and the Eigenstates $|\nu_\alpha\rangle$ $(\alpha = e, \mu, \tau)$ are given by

$$|\nu_\alpha\rangle = \sum_i U_{\alpha i} |\nu_i\rangle \quad \text{or} \tag{2.3}$$

$$\begin{pmatrix} \nu_e \\ \nu_\mu \\ \nu_\tau \end{pmatrix} = \begin{pmatrix} U_{e1} & U_{e2} & U_{e3} \\ U_{\mu 1} & U_{\mu 2} & U_{\mu 3} \\ U_{\tau 1} & U_{\tau 2} & U_{\tau 3} \end{pmatrix} \begin{pmatrix} \nu_1 \\ \nu_2 \\ \nu_3 \end{pmatrix} \tag{2.4}$$

where $U_{\alpha i}$ is the leptonic mixing or PMNS matrix (Pontecorvo, Maki, Nakagawa, Sakata) [MNS62]. The existence of neutrino oscillations has been proven in several experiments, such as Super-Kamiokande, KamLAND and SNO. In 2015 Takaaki Kajita (Kamiokande) and Arthur B. McDonald (SNO) were honored with the Nobel-Prize for their work on experimentally revealing neutrino oscillations [Fuk98] and explaining the *Solar Neutrino Deficit* [A$^+$02]. With the observation of neutrino oscillation it became evident that neutrinos must have a non-vanishing rest mass.
The proof of the non-vanishing neutrino mass was a necessary requirement for the prediction of the extremely rare process of the $0\nu\beta\beta$-decay. Nevertheless, it is still unknown how mass generation on neutrino works. Therefore, the analysis of the $0\nu\beta\beta$-decay is the only way to simultaneously determine both, whether the neutrino is a MAJORANA- or DIRAC-particle and its absolute mass. If being MAJORANA-particles neutrinos would open path to physics beyond the validity of the SM and they would be the only fermions being their own anti-particle. The proof of existence of the $0\nu\beta\beta$-decay and determination of the half-life of any $0\nu\beta\beta$-decay could help to answer many questions on properties of neutrinos. Comprehensive discussions on neutrino properties and neutrino masses can be found in [BV92], [KP93], [Sch97], [Zub11].

2.1.2 Single Beta Decay

Radioactive nuclei decay via emission of particles, such as α- and β-particles and neutrinos and they can deexcite via γ-emission. All these processes lead to a lower energetic state of the nucleus.
A β^--decay is the transformation of a d- to u-quark via emission of an electron e, an electron-anti-neutrino $\bar{\nu}_e$ and the release of energy Q. On nuclear level it corresponds

to a transformation of a neutron to a proton with emission of the same secondary particles. A β^+-decay is a transformation of an u- to d-quark via positron emission or by electron capture (EC). Beside the e^+ or X-ray emission, both processes are accompanied by electron-neutrino ν_e emission and the release of energy Q. The occurrence of β^+-emission or electron capture depends on the available energy excess. For positron-emission a Q-value of at least 1.022 MeV is necessary. In both β^+-decays on nuclear level a proton is transformed into a neutron. The three decays can be described like:

$$\beta^-\text{decay}: \quad {}^A_Z\mathrm{X} \longrightarrow {}^A_{Z+1}\mathrm{Y} + e^- + \bar{\nu}_e + Q \tag{2.5}$$

$$\beta^+\text{decay}: \quad {}^A_Z\mathrm{X} \longrightarrow {}^A_{Z-1}\mathrm{Y} + e^+ + \nu_e + Q \tag{2.6}$$

$$\text{electron capture}: \quad {}^A_Z\mathrm{X} + e^- \longrightarrow {}^A_{Z-1}\mathrm{Y} + \nu_e + Q \tag{2.7}$$

whereas A is atomic mass, Z the atomic number and Q is the released energy. In all cases Q can be determined as follows

$$Q = [m(Z,A) - Z \cdot m_e]c^2 - [m(Z+1,A) - (Z+1) \cdot m_e + m_e]c^2 \tag{2.8}$$

In equations 2.9 and 2.10 the semi-empirical Bethe-Weizsäcker mass formula describes the mass deficit of nuclei. The parameters of equation 2.10 are given in table 2.1.

$$M(A,Z) = (A-Z) \cdot m_n + Z \cdot (m_p + m_e) - E_B/c^2 \tag{2.9}$$

$$E_B(A,Z) = a_V A - a_S A^{2/3} - a_C \frac{Z(Z-1)}{A^{1/3}} - a_A \frac{(A-2Z)^2}{A} - \delta A^{1/2} \tag{2.10}$$

Table 2.1: The parameters of the BETHE-WEIZSÄCKER mass formula of equation 2.10

symbol	value	description
a_V	15.75 MeV	volume term: proportional to the total number A, densest packing of nucleons
a_S	17.80 MeV	surface term: binding energy is reduced proportional to the surface $A^{2/3}$
a_C	0.711 MeV	Coulomb term: electrostatic repulsion between protons reduces the binding energy proportional to the radius $A^{1/3}$ of the sphere.
a_A	23.70 MeV	asymmetry term: unequal number of protons and neutrons reduces E_B
δ	$\begin{cases} -11.18\,\text{MeV}, & \text{e-e nuclei} \\ 0, & \text{e-o or o-e} \\ +11.18\,\text{MeV}, & \text{o-o nuclei} \end{cases}$	pairing term: effect of spin-coupling, even number of nucleons is more stable than an odd number due to the Pauli principle

2.1.3 Double Beta Decay

In 1935 GÖPPERT-MAYER suggested the existence of *neutrino accompanied double beta decay* ($2\nu\beta\beta$-decay) [GM35].

$$ {}^{A}_{Z}\mathrm{X} \longrightarrow {}^{A}_{Z+2}\mathrm{Y} + 2e^- + 2\bar{\nu}_e + Q \tag{2.11} $$

Such a decay becomes possible, if the single beta decay is energetically suppressed but still a nuclei with a lower binding energy does exist. These circumstances can be found on split mass parabolae for isobaric even-even and odd-odd nuclei as described by the parameter δ in formula 2.10. According to figure 2.1 the decay of ^{116}Cd to ^{116}In is not possible as mass deficit of ^{116}Cd is lower than those of ^{116}In.

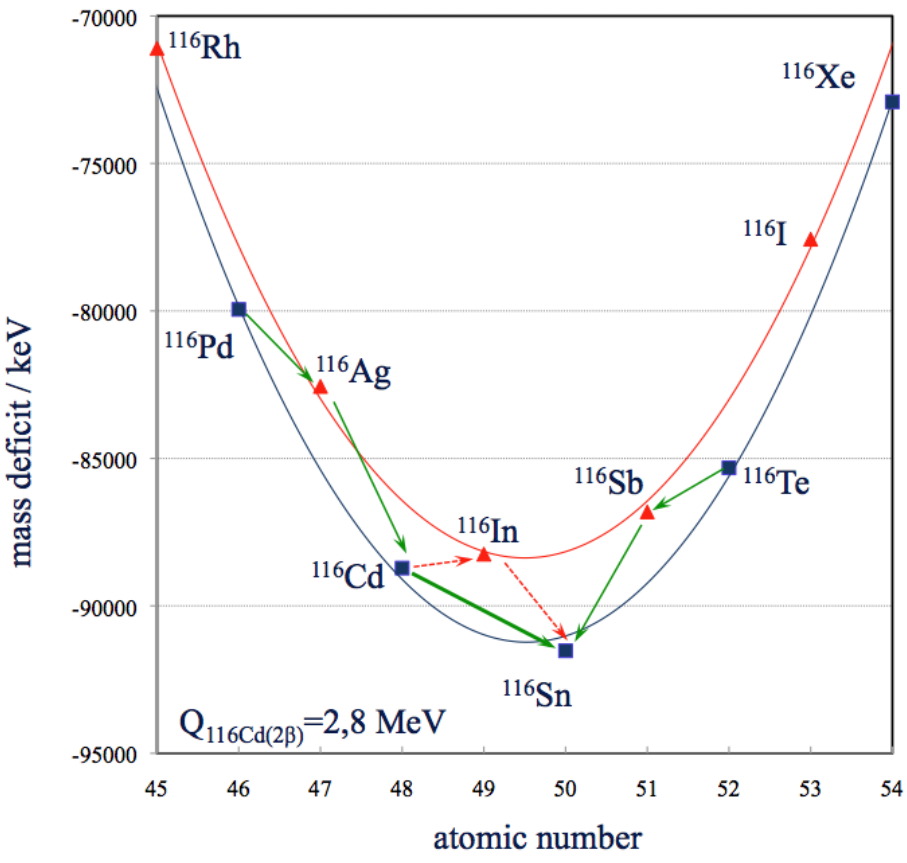

Figure 2.1: The A=116 isobar and the split of the mass parabola in two branches: odd-odd configuration in red, even-even configuration in blue; allowed single β-decay is shown in thiner green arrows; the decay of ^{116}Cd to ^{116}Sn via ^{116}In in two single β-decay processes is forbidden (red dashed arrows) but instantaneous $\beta\beta$-decay is possible (bold green arrow), values from [FBC96].

Nevertheless, ^{116}Sn shows an even lower mass deficit than ^{116}Cd. Hence, a second order process is required to instantaneously change the atomic number by two units: the $2\nu\beta\beta$-decay. Such $\beta\beta$-decay processes are possible for all types of β-transitions: β^--, β^+- and EC-processes. In total 35 isotopes are known that can undergo $\beta^-\beta^-$-decay, whereas only six $\beta^+\beta^+$-configurations can be found. The $\beta^+\beta^+$-transitions are always accompanied by β^+-EC and EC-EC-modes. For the 2ν-processes a continuous energy spectrum of the emitted particles is expected. It is based in the fact, that such decays are multi-particle processes with momentum transfer to the electrons/positrons and the escaping electron (anti-)neutrinos. The momentum transfer to the daughter nuclei is neglected. The first proof of $2\nu\beta\beta$-decay was performed in 1987 by Elliot et al for the decay of ^{82}Se$\rightarrow^{82}$Ge [EHM87] (figure 2.2 left side). The determined half-life was $T^{2\nu}_{1/2} \simeq 10^{20}$ yr, making it the rarest ever observed nuclear transition at this time.
Already in 1939 Furry suggested $0\nu\beta\beta$-processes [Fur39]. For such a process a mechanism to adopt the mismatching helicity is required, allowing to absorb the emitted right-handed $\bar{\nu}_R$ from one neutron as a left-handed ν_L at another neutron ($\nu_L \equiv \bar{\nu}_L$ and $\nu_R \equiv \bar{\nu}_R$) [Sch97] [BV92] [Zub11] (figure 2.2 right side).

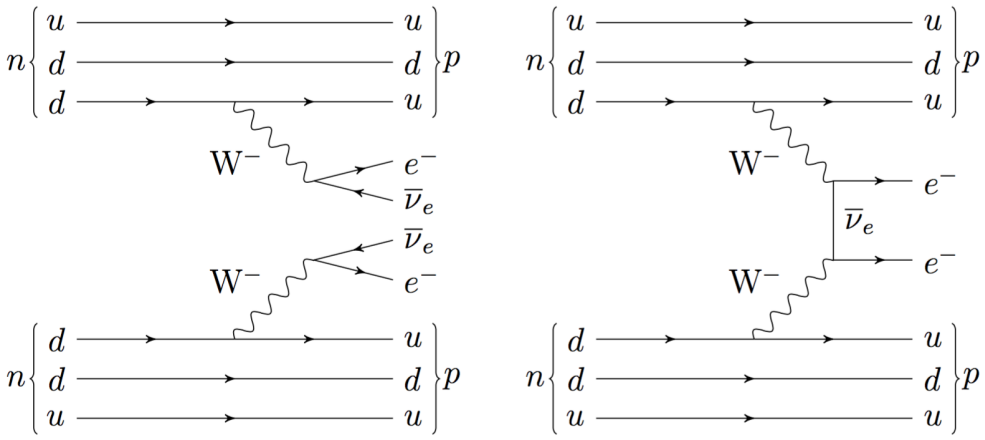

Figure 2.2: Feynman diagram for $\beta^-\beta^-$-processes. Left: neutrino accompanied case - allowed in the standard model. Right: neutrinoless double beta decay - forbidden in the standard model

In contrast to the continuous spectrum of the $2\nu\beta\beta$-decay in case of the $0\nu\beta\beta$-decay the full Q-value is transferred to the emitted electrons only - the momentum transfer to the much heavier daughter nucleus is neglected, too. If the two emitted electrons deposit their energy in the same detector, a peak at the Q-value of the decay is expected (figure 2.3). Under experimental conditions the unavoidable $2\nu\beta\beta$-decay generates background for $0\nu\beta\beta$-process search. Therefore, the energy resolution of the detector has to be as good as possible to separate 0ν- from 2ν-events. In figure 2.3 an energy resolution of the detector of 1% at the Q-value of ^{116}Cd, a half-life of $2.88 \cdot 10^{19}$ yr for $2\nu\beta\beta$-decay [Bar15] and $2 \cdot 10^{26}$ yr for $0\nu\beta\beta$-decay is assumed. As the $0\nu\beta\beta$-process is strongly suppressed, the expected peak is scaled up to be visible. The determination of the

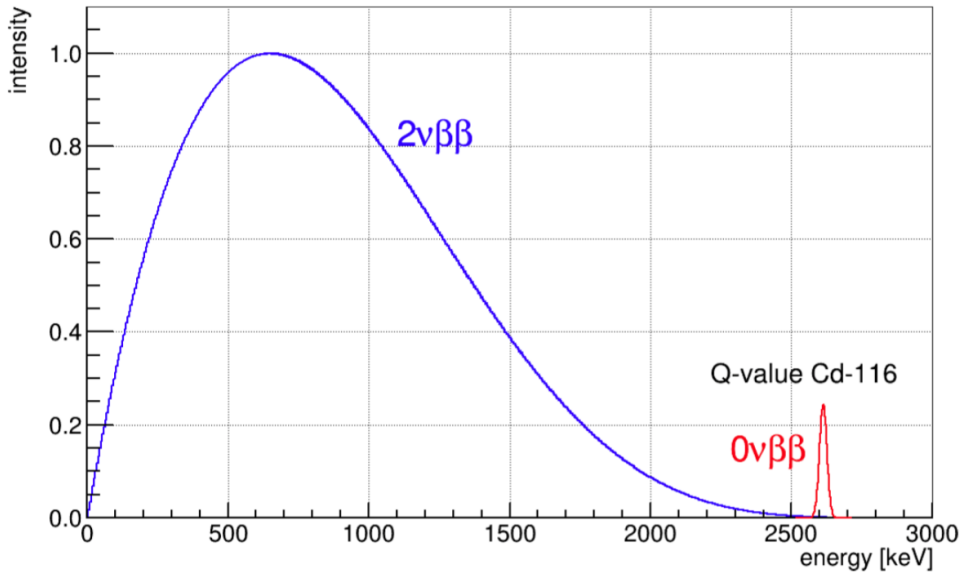

Figure 2.3: Principal shape of neutrino accompanied and neutrinoless double beta decay. The intensity of expected $0\nu\beta\beta$-decay is scaled up by 10^6. [Köt12]

half-life of a $0\nu\beta\beta$-decay allows to deduce the effective Majorana neutrino mass $\langle m_{\nu_e} \rangle$ as the half-life and the neutrino mass are directly related [Zub11]:

$$\left(T^{0\nu}_{1/2}\right)^{-1} = G^{0\nu}(Q,Z) \ \left|M^{0\nu}_{GamowTeller} - M^{0\nu}_{Fermi}\right|^2 \ \left(\frac{\langle m_{\nu_e} \rangle}{m_e}\right)^2 . \tag{2.12}$$

In formula 2.12 the $G^{0\nu}(Q,Z)$ describes the phase space integral, depending on the Q-value of the decay and the nuclear matrix elements (NME) $M^{0\nu}_{GamowTeller}$ and $M^{0\nu}_{Fermi}$. The Q-value can be determined precisely, e.g. by penning trap measurements. For NME different models have been established leading to varying but comparable results. The results vary by a factor of two, depending on model and isotope [DRZ11]. Nevertheless, a direct measurement of the half-life of a $0\nu\beta\beta$-decay would allow to determine the effective Majorana mass $\langle m_{\nu e} \rangle$ as described in formula 2.3.
Up to this day, only lower limits for $0\nu\beta\beta$-half-lives have been given from various experiments, as stating a measured half-life for an isotope would be equal to discovery of $0\nu\beta\beta$-decay and the decision of neutrino being either MAJORANA- or DIRAC-particle. Neutrino-oscillation-experiments can reveal information on squared mass differences of neutrinos only, whereas $0\nu\beta\beta$-experiments are able to determine the absolute mass.
Several $\beta\beta$-decay experiments are currently ongoing, covering a number of isotopes and applying diverse detector concepts. Table 2.2 contains a selection of recent results. Further experiments with different detection concepts are ongoing or in preparation, mostly featuring enhanced effective detector mass. The different concepts have specific advantages and drawbacks. Large scintillation detectors, like the upcoming SNO+ ex-

periment, feature an enormous amount of the $\beta\beta$-isotope ^{130}Te but suffers from limited energy resolution. In contrast, detector concepts with superb energy resolution, like semiconducting solid state detectors, are limited on supply and operational capabilities for enriched detectors.

Table 2.2: Selection of currently ongoing $0\nu\beta\beta$-experiments, isotopes and sensitivities. The latest COBRA-Demonstrator results are given too [EFG$^+$16]. Additionally, two measured half-life values for the neutrino accompanied $\beta\beta$-decay of ^{116}Cd are given.

isotope	sensitivity	experiment
^{70}Zn	$T^{0\nu}_{1/2} > 6.8 \cdot 10^{18}$ yr	COBRA-Demonstrator experiment, semiconducting detector [EFG$^+$16]
^{76}Ge	$T^{0\nu}_{1/2} > 5.3 \cdot 10^{25}$ yr	GERDA-Germanium Detector Array, semiconducting detector [Col17]
^{114}Cd	$T^{0\nu}_{1/2} > 1.6 \cdot 10^{21}$ yr	COBRA-Demonstrator experiment, semiconducting detector [EFG$^+$16]
^{116}Cd	$T^{0\nu}_{1/2} > 1.1 \cdot 10^{21}$ yr	COBRA-Demonstrator experiment, semiconducting detector [EFG$^+$16]
^{116}Cd	$T^{0\nu}_{1/2} > 1.9 \cdot 10^{23}$ yr	Aurora-Experiment, solid-crystal scintillation detector [Do16]
^{116}Cd	$T^{0\nu}_{1/2} > 1.0 \cdot 10^{23}$ yr	NEMO-3 - Neutrino Ettore Majorana Observatory, combined tracking-calorimetric device [A$^+$16b]
^{128}Te	$T^{0\nu}_{1/2} > 1.9 \cdot 10^{21}$ yr	COBRA-Demonstrator experiment, semiconducting detector [EFG$^+$16]
^{130}Te	$T^{0\nu}_{1/2} > 6.1 \cdot 10^{21}$ yr	COBRA-Demonstrator experiment, semiconducting detector [EFG$^+$16]
^{130}Te	$T^{0\nu}_{1/2} > 4 \cdot 10^{24}$ yr	CUORE-0 - Cryogenic Underground Observatory for Rare Events, bolometric detector [A$^+$16a]
^{136}Xe	$T^{0\nu}_{1/2} > 2.6 \cdot 10^{25}$ yr	KamLAND-Zen - Kamioka Liquid Scintillator Antineutrino Detector zero-neutrino double-beta decay, liquid scintillation detector [Gan12]
^{136}Xe	$T^{0\nu}_{1/2} > 1.6 \cdot 10^{25}$ yr	EXO - Enriched Xenon Observatory, time-projection-chamber [A$^+$12]
^{116}Cd	$T^{2\nu}_{1/2} = (2.62 \pm 0.14) \cdot 10^{19}$ yr	Aurora-Experiment, solid-crystal scintillation detector [Do16]
^{116}Cd	$T^{2\nu}_{1/2} = (2.74 \pm 0.22) \cdot 10^{19}$ yr	NEMO-3 - Neutrino Ettore Majorana Observatory, combined tracking-calorimetric device [A$^+$16b]

2.2 The Concept of the COBRA-Experiment

2.2.1 CZT in the COBRA-Experiment

The **C**admium Zinc Telluride **0**-Neutrino Double **B**eta **R**esearch **A**pparatus (COBRA) is an experiment to investigate the existence of $0\nu\beta\beta$-decay (section 2.1.3) and was proposed by ZUBER in 2001 [Zub01]. In the COBRA approach the detector itself partly consists of the isotope of interest. The COBRA Demonstrator is assembled out of $64\times1\,\mathrm{cm}^3$ Cadmium-Zinc-Telluride (CZT, section 2.2.2) detectors in a $(4 \times 4 \times 4)$-detector array. A schematic drawing is shown in figure 2.4. The detailed description of the experimental setup of the COBRA Demonstrator can be found at Appendix A.2.

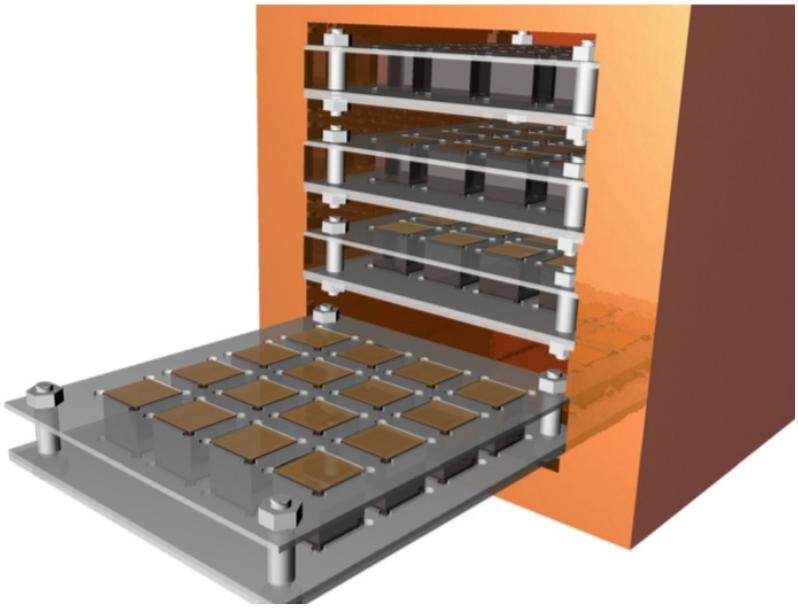

Figure 2.4: Rendering of the COBRA Demonstrator detector assembly with 64 CZT detectors arranged in 4 detector layers. [Mue07]

For $\beta\beta$-research CZT is interesting as it contains a total of nine $\beta\beta$-isotopes (table 2.3). Not all of the mentioned isotopes are suited for $\beta\beta$-research. The most promising isotope is ^{116}Cd with a Q-value of $Q_{116\mathrm{Cd}} = 2813.5\,\mathrm{keV}$.
The highest naturally occurring gamma line is that of ^{208}Tl at $E = 2614.5\,\mathrm{keV}$, which is part of the decay-chain of ^{232}Th and, hence, present all over in nature. Above the gamma line of ^{208}Tl no other natural gamma line with notable intensity can be found, accordingly, at the Q-value of ^{116}Cd, no natural γ-background is present and thus, the overall background is greatly reduced. Another well suited isotope for $\beta\beta$-decay search in the COBRA-experiment is ^{130}Te. Even though its Q-value of $Q_{130\mathrm{Te}} = 2526.97\,\mathrm{keV}$ is lower than the full-energy-peak (FEP) of ^{208}Tl, it lies in between the FEP and the Compton edge of the ^{208}Tl-FEP at $E = 2381.7\,\mathrm{keV}$ and is also mostly background

Table 2.3: List of intrinsically abundant $\beta\beta$-isotopes contained in CZT; abundance values from [FBC96] with uncertainties in parenthesis, Q-values from recent publications

isotope	decay mode	natural abundance	Q-value [keV]
Zn-64	β^+/EC; EC/EC	48.6(3)%	1095.70(7) [BBC$^+$09]
Zn-60	$\beta^-\beta^-$	0.6(1)%	998.50(22) [BBC$^+$09]
Cd-106	$\beta^+\beta^+$; β^+/EC; EC/EC	1.25(4)%	2775.01(56) [S$^+$12]
Cd-108	EC/EC	0.89(2)%	272.04(55) [S$^+$12]
Cd-114	$\beta^-\beta^-$	28.73(28)%	542.3 [G$^+$17]
Cd-116	$\beta^-\beta^-$	7.49(12)%	2813.50(13) [REE$^+$11]
Te-120	β^+/EC; EC/EC	0.096(2)%	1714.81(13) [S$^+$09]
Te-128	$\beta^-\beta^-$	31.69(1)%	865.87(13) [S$^+$09]
Te-130	$\beta^-\beta^-$	33.80(1)%	2526.97(23) [REE$^+$11]

free. ^{130}Te is also the isotope of interest at bolometric measurements at CUORICINO, CUORE-0 and upcoming CUORE $\beta\beta$-experiment at LNGS [A$^+$16a] or SNO+ at SNOLAB underground laboratory [Seg16].
From the point of high Q-value, ^{106}Cd is a promising candidate, too. In contrast to ^{116}Cd, which is a neutron-rich nucleus and decays via $\beta^-\beta^-$-decay, ^{106}Cd is a neutron-poor nucleus and undergoes $\beta^+\beta^+$-decay. Due to its high Q-value, three different decay schemes are possible, which are $\beta^+\beta^+$, β^+/EC and EC/EC modes. In β^+-decay the emission of a positron is always accompanied with annihilation radiation. The two photons with an energy of $E_\gamma = 511\,\text{keV}$ are emitted at the end-point of the random walk of the positron. Even if CZT is a dense material, the 511 keV photons have a good chance of escaping the source detector or to undergo Compton scatter processes out of the detector, so, that only a part of the primary energy is deposited in the detector. Due to the two annihilation processes of both emitted positrons, the likeliness for at least one of the four photons to escape is high. As a result, not the full Q-value of the $0\nu\beta^+\beta^+$-decay is deposited in the source detector. The great advantage of the COBRA approach is the high granularity of the setup. This allows to analyze neighboring detectors for time coincident energy depositions that could be attributed to positron annihilation processes or escaping electrons from adjacent detectors.
The β^+/EC and EC/EC modes are even more complex to identify. Electron capture processes are connected with high energetic emissions of gamma rays from the excited daughter nucleus and low energy X-ray emission of electron shell recombination processes. The excited nucleus emits specific gamma radiation in the several hundred to thousand keV range, which are also likely to escape the source detector. In case of ^{106}Cd$\rightarrow^{106}$Pd the lowest two excited states of ^{106}Pd can be found at E_1=511.8 keV and E_2=1128.0 keV. The excited states deexcite almost instantaneously within a few pico-seconds after the electron capture process and could be used as analysis trigger for time coincident low energy X-ray events. The X-ray emission of K-shell refilling of

palladium can be found at $E_{K\alpha 1} = 21.2\,\mathrm{keV}$, but at present, the lower detection limit of the COBRA Demonstrator is at about $E_{det} \sim 50\,\mathrm{keV}$. Due to their low Q-values, the other possible $\beta\beta$-isotopes are affected by the overlay of many background contributions, such as natural ^{40}K and further isotopes of the uranium- and thorium-decay chain, their deexcitation-lines and other contamination sources, that emit alpha- and beta-particles.
The sensitivity of an experiment for detecting a half-life ($T^{\mathrm{exp}}_{1/2}$) for a specific isotope can be estimated to be

$$T^{\mathrm{exp}}_{1/2} \simeq a \cdot \epsilon \cdot N_0 \cdot \sqrt{\frac{M \cdot t}{\Delta E \cdot B}} \quad . \tag{2.13}$$

The three parameters with direct proportionality to the half-life-sensitivity are the abundance of the isotope under investigation $a/[\%]$, the total detection efficiency of the detector assembly $\epsilon/[\%]$ and the total number of target atoms per unit mass $N_0/1$. The parameters under the square-root are the total mass of the experiment $M/[\mathrm{kg}]$ and the total life-time $t/[\mathrm{yr}]$ of the experiment in the nominator, and the energy resolution $\Delta E/[\mathrm{keV}]$ and the background-index $B/[1/\mathrm{keV{\cdot}kg{\cdot}yr}]$ in the denominator.
As to be seen, the most efficient way to improve the half-life-sensitivity of the experiment is to increase the abundance a of the isotope of interest in the detector. The natural abundance of ^{116}Cd is only 7.49%. Hence, the sensitivity can easily be increased by a factor of 12 by manufacturing the detectors out of 90% enriched ^{116}Cd as proposed by the COBRA collaboration. Such step is very effective, but enriching is an expensive process. ^{130}Te has already a natural abundance of 33.8% but also has a ten times higher background in the region of interest.
The total efficiency ϵ of the setup mainly depends on the effective atomic number Z, density ρ of the detector material and the overall size of the detector. Z and ρ define the stopping power for charged particles and, hence, the escape probability of the particles. Both, Z and ρ, are given by the properties of CZT detectors and vary only slightly, depending on zinc content of the crystal (section 2.2.2). Therefore, the only possibility to improve detection efficiency is to increase the size of the detector. The COBRA Demonstrator setup is assembled from $(1.0 \times 1.0 \times 1.0)\,\mathrm{cm}^3$ sized CZT cubes (figure 2.5). As the detector itself is made from the decaying isotopes, a good intrinsic efficiency is given. GEANT4 based simulations have shown, that for the $(1.0 \times 1.0 \times 1.0)\,\mathrm{cm}^3$ CZT detectors the full energy efficiency is 49.3% to detect both electrons of $\beta\beta$-decay, each emitted at half Q-value of ^{116}Cd [Köt12]. With the change from the $1\,\mathrm{cm}^3$ detectors to the larger $(2.0 \times 2.0 \times 1.5)\,\mathrm{cm}^3$ detectors the intrinsic efficiency rises accordingly, resulting in a 63% efficiency for full energy deposition of $\beta\beta$-decay of ^{116}Cd in the larger crystal. The given efficiencies are worst case scenarios, as different frameworks and physics lists result in deviating efficiencies [Köt12]. Investigations are ongoing to identify the root cause of the discrepancies.
Another positive effect on changing from $(1.0 \times 1.0 \times 1.0)\,\mathrm{cm}^3$ to $(2.0 \times 2.0 \times 1.5)\,\mathrm{cm}^3$ detectors is the 0.55 times smaller surface to volume ratio and the reduced number of needed read-out channels per detector volume. The number of read-out channels

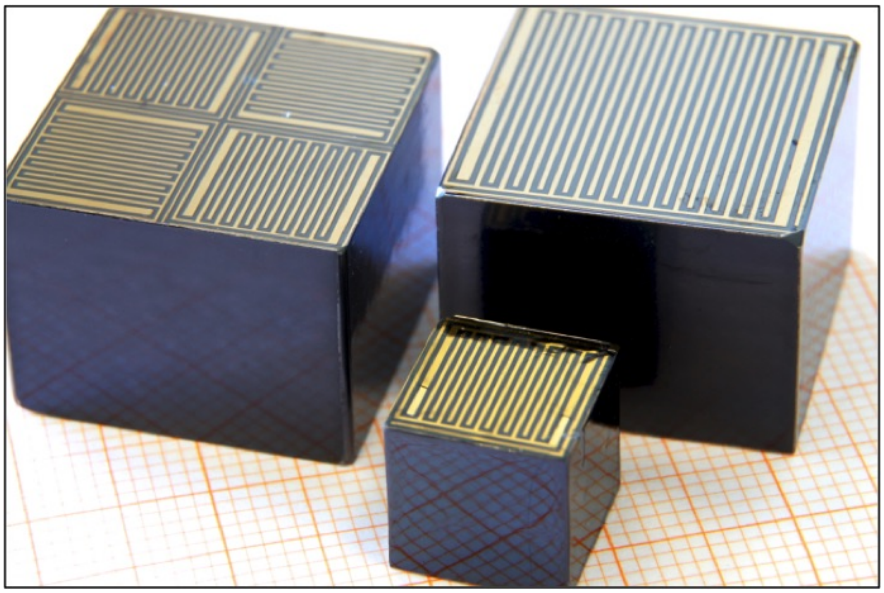

Figure 2.5: Comparison of $(1.0 \times 1.0 \times 1.0)\,\mathrm{cm}^3$ (front) with two different versions of the $(2.0 \times 2.0 \times 1.5)\,\mathrm{cm}^3$ CZT detectors used in the COBRA experiment. The COBRA Demonstrator at LNGS is assembled from $64{\times}1\,\mathrm{cm}^3$ detectors. The COBRA-XDEM will be assembled from $9{\times}6\,\mathrm{cm}^3$ detectors in quad anode configuration (left side), the monolithic single anode $6\,\mathrm{cm}^3$ detector (right side) is not in use.

is reduced by 1/3 for the $6\,\mathrm{cm}^3$ detectors with the quad-layout compared to the same installed total detector volume based on $1\,\mathrm{cm}^3$ detectors. The $6\,\mathrm{cm}^3$ detectors will be assembled in COBRA extended Demonstrator (XDEM) in a $3{\times}3$ array to evidence the improved performance of the larger detectors for COBRA purposes. It is scheduled to be installed in early 2018. A comprehensive study on the performance of the large volume CZT detectors can be found in [EGG+16a].
The total number of target atoms N_0 depends on the molar weight M_{CZT} of the detector material and, hence, on its stoichiometry. CZT is typically made from 45% cadmium, 5% zinc and 50% tellurium. The molar weight of CZT can be calculated to be $M_{CZT} = 235.31\,\mathrm{g/mol}$ for 5% zinc concentration. The variable concentration of zinc is discussed in section 3.1.
To be sensitive to expected half-lives greater than $T_{1/2} > 10^{25}\,\mathrm{yr}$, a large number of source atoms in the detector is needed. As the stoichiometry of the detector material is an almost fixed parameter and the natural abundance is in case of ^{116}Cd an effective but limited regulator, the only way to increase the number of source atoms is to massively scale up the total detector mass M. Additionally, the data taking has to run for several years life-time t to collect a significant $0\nu\beta\beta$-signal over the expected background B. To be able to detect the very rare events of $\beta\beta$-decay it is a major requirement to be free of natural and artificial background at the peak position. The factor ΔE in equation 2.13 is the width of the energy acceptance window in the region of interest (ROI). For ^{116}Cd the ROI ranges from $E = (2723 \ldots 2904)\,\mathrm{keV}$. The width

of this window depends on the energy resolution of the detector and must be chosen accordingly. An energy resolution of about 1% at the Q-value of ^{116}Cd is needed to separate the expected $0\nu\beta\beta$-events from the $2\nu\beta\beta$-events close to the endpoint of the spectrum with high efficiency. Figure 2.6 shows the calculated sensitivities for different experimental setups and life-times. To be sensitive to the predicted half-life of $T_{1/2} > (2 \cdot 10^{26})$ yr for ^{116}Cd several requirements have to be fulfilled. The detectors have to be enriched to 90% ^{116}Cd and a total detector mass of $m_{\text{tot}} = 420$ kg has to be installed. With the XDEM detectors the high intrinsic detection efficiency of $\epsilon = 63\%$ is given. First experiments have shown, that a relative energy resolution of $\Delta E \leq 1\%$ at $Q_{116\text{Cd}} = 2813.5$ keV can be achieved, too. The background index in the region of interest is due to be determined with the underground operation of COBRA-XDEM [EFG+16].

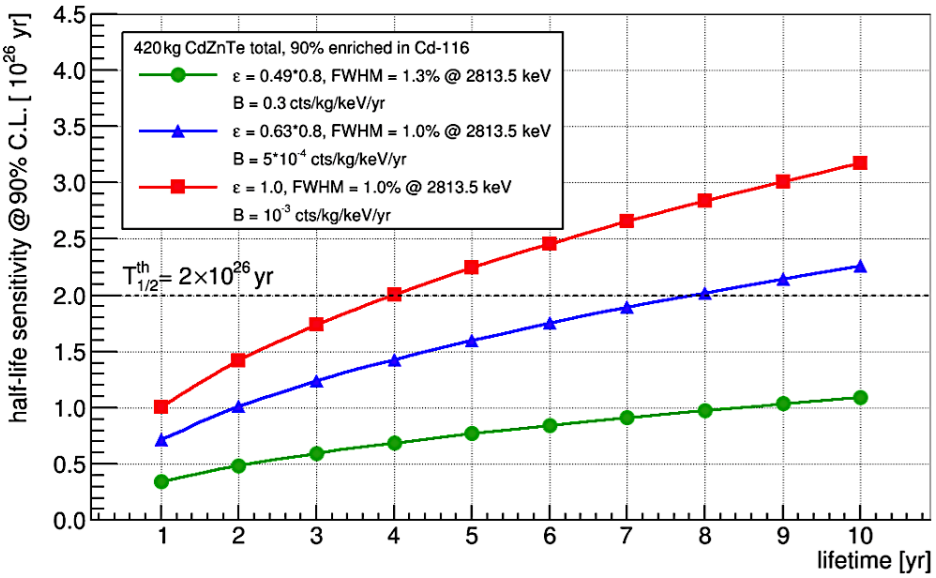

Figure 2.6: Based on equation 2.13 three different scenarios have been calculated for a 420 kg COBRA experiment with 90% enriched ^{116}Cd detectors. Option 1 (green) - current COBRA Demonstrator (1 cm^3 detectors) scaled up; Option 2 (blue) - COBRA-XDEM (6 cm^3 detectors) scaled up; Option 3 - ideal setup [Zat14]

2.2.2 General Remarks on CZT

Radioactive isotopes decay via the emission of particles, such as α- and β–particles or of heavy fission-products in the case of spontaneous fission. In many cases this is accompanied by the emission of photons, such as γ–radiation for nuclear deexcitation or X–rays in case of electron shell deexcitation and subsequent recombination. To detect radioactive decay of a nucleus, the emitted particle has to undergo an interaction with an appropriate detector and to deposit energy in it. A detailed discussion of the particle–detector–interaction can be found in [Kno00, Leo92].

For the analysis of γ–radiation the state-of-the-art detectors are semiconducting high-purity germanium detectors (HPGe). Those detectors offer a superior energy-resolution in the range of about 1 keV at 1330 keV and a good efficiency due to the high atomic number Z_{Ge}=32 and density ρ_{Ge}=5.33 g/cm³. Because of their great performance these detectors have obtained a wide spread in the field of nuclear analytics. The main drawback of HPGe is its low band gap of $E_{g(Ge)} = 0.67\,\text{eV}$, requiring permanent liquid nitrogen or electric cooling during operation.
A possible successor of HPGe is CZT. CZT is used as radiation detector in a wide field of applications, ranging from utilization for medical image reconstruction and industrial radiation detection devices over space craft instrumentation for low energy gamma ray imaging up to scientific radiation detection applications. CZT is an intrinsic, ternary II-VI-semiconductor like ZnS, HgI or Cd(Zn)Se. In contrast to its material–physically origin, Cadmium-Telluride (CdTe), the cadmium content in CZT is partially replaced by zinc, whereas the zinc content varies from $c_{Zn} = (5 \ldots 10)\,\text{at\%}$. In contrast to germanium, which is grown in large monocrystalline ingots via the well established Czochralski process, CZT can not be manufactured this way, as it is a ternary phase with a complex phase diagram [Nip04]. Several methods exist to grow this material, that all have in common to freeze out the crystal from a well adjusted stoichiometric melt. Here the high– and low–pressure bridgeman process (HPB, LPB) and the traveling heater method (THM) are to be mentioned as the methods with the highest output [BDLA93, STY$^+$01, AMC$^+$10]. Other approaches like the growth from the vapor phase (PVT) or from solutions (PBSE) exist too [CVH$^+$09, PDB$^+$05]. The HPB– or VPB–growth of CZT ingots happen at very slow rates of usually a few millimeters a day. Due to the week ionic binding in II-VI-semiconductors and the high diffusion rate of Zn in CZT, the zinc concentration of the ingots differ from the seed to the top of the crystal [Cro04]. In comparison to germanium, CZT offers a fairly good energy resolution of ∼25 keV at 1330 keV and has an even higher mean atomic number of $Z_{CZT} \sim 50$ and density ρ_{CZT}=5.78 g/cm³. Due to its wide band gap of $E_{g(CZT)}$=1.57 eV CZT based devices can usually be operated at room temperature. This offers great opportunities for wide fields of applications, such as the development of handheld spectroscopic devices. A listing of the main physical properties of widely used semiconductor detector materials can be found in table 2.4.

2.2.3 Single Charge Sensitive Devices

As described in table 2.4, the mobility–lifetime–product $\mu\tau$ of Germanium is in the range of about $\mu\tau_{e/h}|_{\text{Ge}} = 1\,\text{cm}^2/\text{s}$ for electrons and holes, respectively. Despite the latest improvements in CZT crystal growth and improved detector quality, the charge transport properties of CZT are inherently much worse. In CZT the mobility–lifetime–product of holes is roughly $\mu\tau_h|_{\text{CZT}} \simeq 5 \cdot 10^{-5}\,\text{cm}^2/\text{s}$ and those of electrons $\mu\tau_e|_{\text{CZT}} = (3...5) \cdot 10^{-3}\,\text{cm}^2/\text{s}$. Such, the $\mu\tau$ of electrons and holes differs by a factor of ∼100× which is also known as the *ballistic deficit*. This ballistic deficit clearly impacts the raw–signals from the detector and requires a more complex analysis of data taken with such devices. Additionally, the high density of trapping zones and

Table 2.4: Properties of CZT, CdTe, Si and Ge measured at room temperature [Mue07]

Property	CZT	CdTe	Ge	Si
Atomic number Z	48, 30, 52	48, 52	32	14
Density ρ_m / (g/cm^3)	5.78	5.85	5.33	2.33
Band Gap E_g/ (eV)	1.572	1.5	0.67	1.12
e^-h^+-Creation Energy E_{pair}/ (eV)	4.64	4.43	2.95	3.62
Resitivity ρ/ (Ωcm)	3×10^{10}	1×10^{9}	50	$<10^4$
Electron Mobility μ_e / (cm^2/Vs)	1000	1100	3900	1400
Hole Mobility μ_h / (cm^2/Vs)	50-80	100	1900	480
Electron Lifetime τ_e/ (s)	3×10^{-6}	3×10^{-6}	$> 10^{-3}$	$> 10^{-3}$
Hole Lifetime τ_h/ (s)	1×10^{-6}	2×10^{-6}	10^{-3}	2×10^{-3}
Mob.–Lifetime–Product e $\mu\tau_e$ / (cm^2/s)	(3-5)$\times10^{-3}$	3.3×10^{-3}	>1	>1
Mob.–Lifetime–Product h $\mu\tau_h$ / (cm^2/s)	5×10^{-5}	2×10^{-4}	>1	∼1

the thereby caused charge loss affects the detected signal negatively. Due to this limitations the detected signal strongly depends on the depth of interaction between the electrodes. This problem is very similar to gas–ionization chambers, that suffer from good electron–transport properties but poor ion–transport properties. To address this problem, Frisch introduced a grid in-between the cathode and the anode that electrostatic shields the anode [BCH49]. Shielded by this grid, the moving carriers do not induce any charge at the anode during their drift between the electrodes. As the electrons pass trough the grid, a charge is induced at the anode. The introduction of the so called Frisch–Grid improved the gas–ionization-chambers massively, as the detected signal is now mostly independent on the point of interaction within the device. In 1994 Luke proposed a similar approach for solid-state detectors [Luk94]. He introduced a coplanar grid (CPG) at the anodes consisting of two interleaved, isolated comb–structured electrodes instead of a single, plain one (figure 2.7). In contrast to the Frisch-Grid approach, which requires great efforts to be implemented in semiconductor devices, a CPG can easily be deposited on CZT devices. The drawback is, that the operation and the signal readout of such a detector is more complex, compared to the operation of a planar detector, as an additional anode has to be read out and a second (grid-) bias voltage has to be applied.
The electric field in a planar device is a straight forward field throughout the detector. The induced signal due to moving charge carriers can be calculated based on the Shockley-Ramo-Theorem [Ram39]:

$$Q = -q\,\Delta\,\varphi_W\,(\vec{r}), \tag{2.14}$$

whereas Q is the induced charge at the electrode, q is the charge of the carrier and $\varphi_W(\vec{r})$ is the electric potential in the detector in case that the respective electrode is

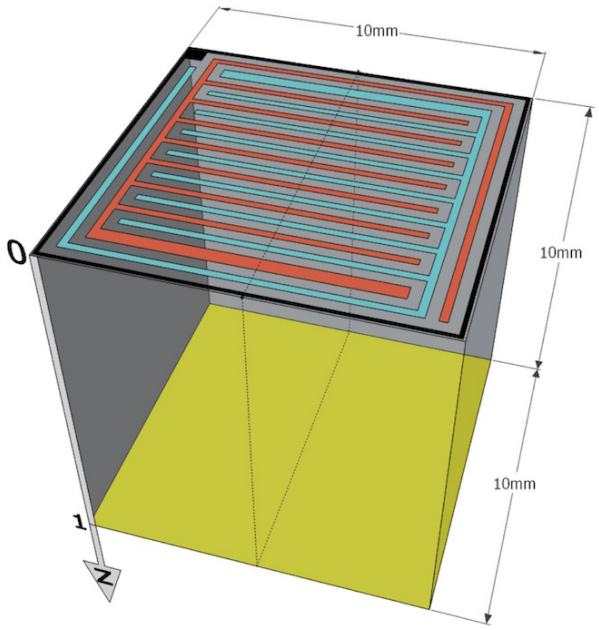

Figure 2.7: Schematic layout of the two interleaved electrodes of the CPG detectors. The anode at the bottom covers the full crystal area. Dimensions are given for the COBRA Demonstrator detectors [Fea13].

held at unit potential, with all other electrodes grounded. It is important to notice, that the weighting potential $\varphi_W(\vec{r})$ is just a dimensionless mathematical instrument and not directly correlated to the real electrical field in the detector.
For the calculation of the weighting potential of CPG detectors, only a pair of electrodes is considered, the other electrodes are set to zero. Hence, every electrode has its own weighting potential depending on the specific design of the anode layout. The amplitudes of the two anode signals can be calculated by Shockley-Ramo-Theorem:

$$\Delta q_{CA} = \frac{1}{2} Q_0 \left(z_0 + 1\right) \quad \text{and} \quad \Delta q_{NCA} = \frac{1}{2} Q_0 \left(z_0 - 1\right) \tag{2.15}$$

Here $\Delta q_{CA/NCA}$ represents the amplitude of the signal at the corresponding anode, Q_0 is the released charge by the ionizing process, and z_0 is the interaction depth between the two electrodes. For the COBRA Demonstrator detectors the weighting field calculations are performed by Fritts et al. and Durst[1] and can be seen in figure 2.8.
To calculate the deposited energy, the depth dependency can be removed by subtraction of the two signals, the reconstruction of the depth of interaction z_0 can be performed analogous:

$$Q_0 = \Delta q_{CA} - \Delta q_{NCA} \quad \text{and} \quad z_0 = \frac{\Delta q_{CA} + \Delta q_{NCA}}{\Delta q_{CA} - \Delta q_{NCA}} \tag{2.16}$$

[1] J. Durst, ECAP, Erlangen, presentation at COBRA-Collaboration meeting, June 2011, Hamburg

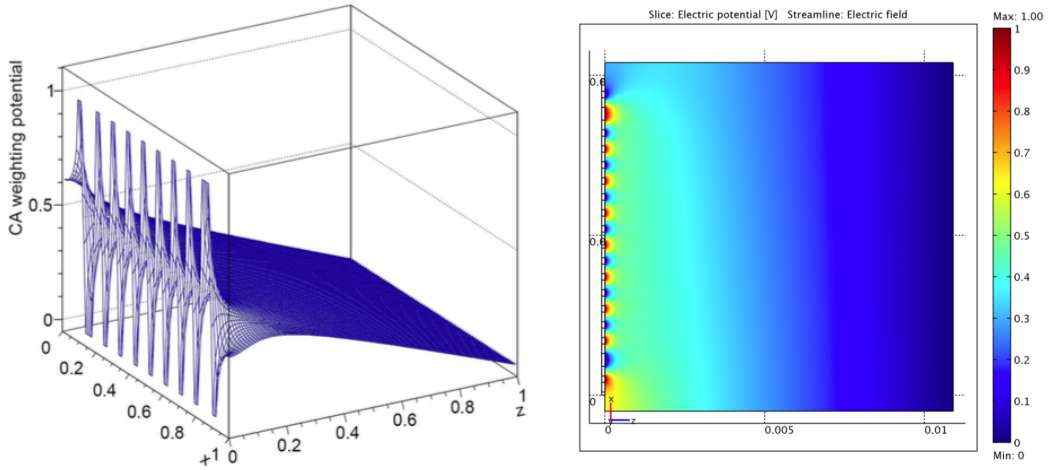

Figure 2.8: Graphical representation of the weighting potential for the collecting anode. Lefthand side: calculation of FRITTS [Fea13]. Righthand side: Finite element calculations using COMSOL by J. DURST, ECAP, ERLANGEN

The equations (2.15) and (2.16) are valid for an ideal detector, only. For the above described impact of charge trapping and recombination during the charge transport, a correction factor w was introduced by LUKE. The deposited charge Q is now represented by:

$$Q_0 = \Delta q_{CA} - w \cdot \Delta q_{NCA} \quad . \tag{2.17}$$

The w is the so called *weighting factor* and corrects for the electron trapping and charge loss during the transport. The raw signal of the charge transport needs to be amplified and is sensed in the FADCs (section A.4). In post processing the actual signal height is calculated by moving two 256 sample wide windows (256 samples apart) along the event to smooth out the noise and high frequencies. The maximum of the difference between the two windows is taken as pulse height of the event for each corresponding anode. A typical single site interaction at high depth is shown in figure 2.9. The red signal (CA) and blue signal (NCA) are sampled by the FADC, the green signal (Diff) is calculated by subtracting NCA signal from CA. The cathode signal is not sampled but can be reconstructed by adding CA and NCA. The effect of charge trapping can be demonstrated by plotting the pulse-height signal of the non collecting anode versus collecting anode (figure 2.10).
For an ideal detector without any charge loss and trapping the signal intensity would be independent of the depth of interaction in the detector and, hence, signal amplitude for CA and NCA would be the same for all depths. Based on the linear approximation of the full-energy interaction lines in the NCA-vs-CA plots, the weighting factor for the detectors can be determined. The slope of this linear approximation is the searched weighting factor w. This factor is detector specific and has to be determined for each detector, respectively. The typical range is $w = 0.95...0.6$, depending on detector qual-

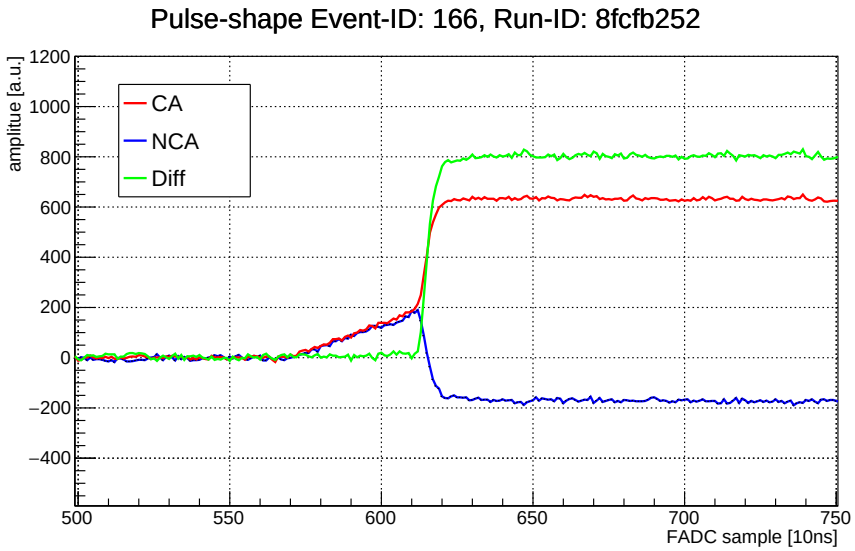

Figure 2.9: Pulse shape of a single site event in high depth. The rise time between $t = 5.4\,\mu s$ and $t = 6.1\,\mu s$ represents the drift of the charge cloud through the detector, the sharp increase between at $t = 6.1\,\mu s$ is caused by the grid bias field in the vicinity of the CA.

ity. Higher values for w represent better charge transport properties of the detector resulting in better energy resolution. The exponential decrease of the charge cloud magnitude in relation to drift distance is given in the following relation:

$$Q = Q_0 \cdot e^{-d/\lambda} \tag{2.18}$$

with d as the drift distance and λ as a free, but detector dependent parameter. Both values are dimensionless and given in relative detector thickness. The parameter λ is directly related to the mobility-lifetime product of the specific crystal. It can be expressed by:

$$\lambda = \frac{1+w}{1-w} \quad . \tag{2.19}$$

Based on the empirically determined parameter λ the electron mobility-lifetime product $\mu\tau_e$ can now be estimated to:

$$\mu\tau_e = \frac{L^2 \cdot \lambda}{V_{bulk}} \quad . \tag{2.20}$$

For the detectors used in COBRA Demonstrator Layer1 and Layer2 the mean electron mobility-lifetime product turned out to be $\mu\tau_e = (1.1 \pm 0.15) \cdot 10^{-2}\,\mathrm{cm}^2/\mathrm{V}$, which is in good agreement with literature values given for CZT detectors [Mue07]. Taking the above described relations into account, a zeroth order trapping corrected depth reconstruction for the used detectors can be deduced:

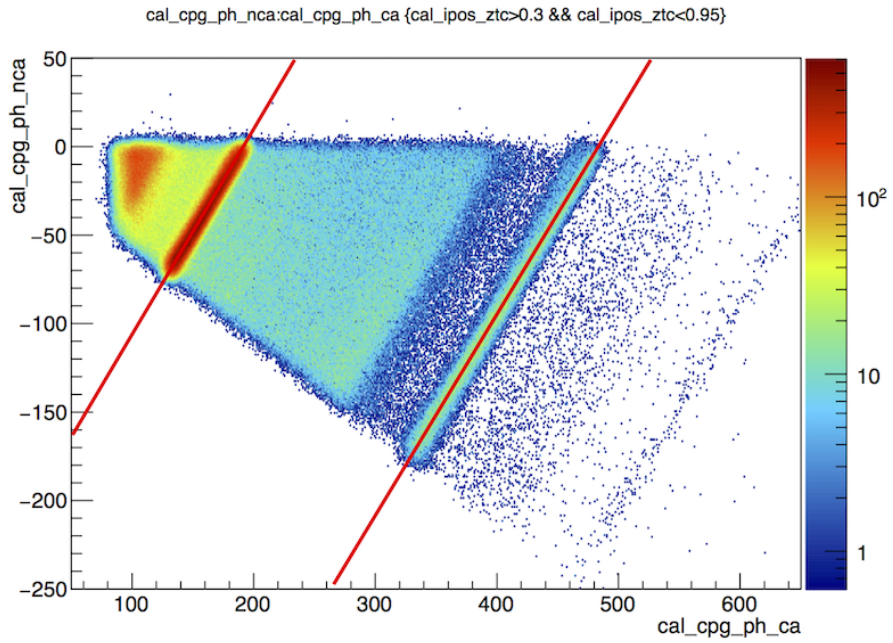

Figure 2.10: Plot of NCA versus CA of a ^{22}Na calibration run. The two lines representing the linear fits of the weighting factor determination at the 511 keV annihilation line and the 1275 keV deexcitation of ^{22}Ne originating from β-decay of ^{22}Na.

$$z_0 = \lambda \ln\left(1 + \frac{1}{\lambda} \cdot \frac{\Delta q_{ca} + \Delta q_{nca}}{\Delta q_{ca} - \Delta q_{nca}}\right) \quad . \tag{2.21}$$

Fritts et al. also considered the impact of the much weaker hole drift that contributes to the anode and cathode signals, too [Fea13]. The lifetime of holes is only about 1% of that of electrons in CZT but due to the long time window for event acquisition in COBRA DAQ with $t = 1024\,\mu s$ it contributes, too. For energy reconstruction the contribution of hole drift in the bulk region of the detector cancels out as the induced charge on CA and NCA is the same and energy is reconstructed by subtraction of CA and NCA signal in equation 2.16. The impact of hole drift is more complex for depth reconstruction. For depth reconstruction, the sum of CA and NCA is evaluated, hence a positive signal induced on both, CA and NCA, leads to an overestimation of interaction depth (equation 2.21). The hole effect must be considered the same way as that of electrons and has to be added to both anode signals:

$$\Delta q_{holes} = \frac{1}{2} Q_0 \, \rho \left(1 - e^{-(1 - z_0/\rho)}\right) \quad . \tag{2.22}$$

The value ρ in equation 2.22 is equivalent to the dimensionless λ in equation 2.18 for electrons and is typically in the range of $\rho \sim 0.1$. The hole contribution is depending on the point of interaction in the detector and must be respected for reconstruction of the

depth of interaction. For interactions very close to the cathode ($z_0 \to 1$) the expression is negligible as the holes have no distance to drift. In case of interactions in the bulk of the detector the additional value $\frac{1}{2}Q_0\rho$ adds to the CA and NCA signals. The described implications for depth reconstruction are implemented in the post processing of COBRA Demonstrator data.

2.3 Pulse Shape Analysis on CZT Detectors

The pulse shape analysis is a key feature for data analysis and data cleaning procedures in ultra low background physics. The precise analysis of pulse shapes allows the identification of different types of events in the detector. The COBRA experiment is designed to sample and store every event triggered in the detectors. No online event preselection is done. This allows an offline analysis and reevaluation of the complete data set if new analytical methods are developed. This section describes methods to reduce background contributions at the detector surface, to identify lateral sidewall events and work performed on differentiation of single site and multi site events.

2.3.1 Anode Side events

The described approach for Q_0– and z_0–reconstruction (section 2.2.3) is valid for straight-forward electrical fields in infinite detectors only. As shown in figure 2.8, the weighting fields of CPG detectors are complex in the vicinity of the anodes or next to the detector sidewalls, hence additional effects have to be considered. Such an effect is the hole attraction of NCA rails for interactions occurring between the CA and NCA rails. At this place the holes do not drift towards the cathode but rather being attracted by NCA, that is on negative potential relative to CA. The result is a doubling in reconstructed energy as the electrons are collected at CA and holes at NCA instead of cathode. The holes induce a negative signal at NCA of nearly the same amplitude as the electron induced signal at CA. The subtraction of the negative NCA signal effectively doubles the reconstructed energy (figure 2.11). That effect has to be considered for interpretation of events in the vicinity of the anodes and can be found in figure 3.43, too.
The pulse shapes in figure 2.9 and 2.11 are single site events (SSE), which means, that the interacting particle, whether alpha, beta or gamma, deposits its full energy in a narrow volume. Due to the dense ionization process of alpha particles, its appearance is always single site, independent of primary energy. The localization of the interaction of beta particles with matter is more energy dependent, but still most of the interactions are single site.

2.3.2 Single/Multi Site Events

Beside photo electric absorption, high energetic photons can also interact via Compton scattering, depositing only a part of its initial energy in the first interaction. With a certain chance a second interaction of the scattered photon can happen in the same

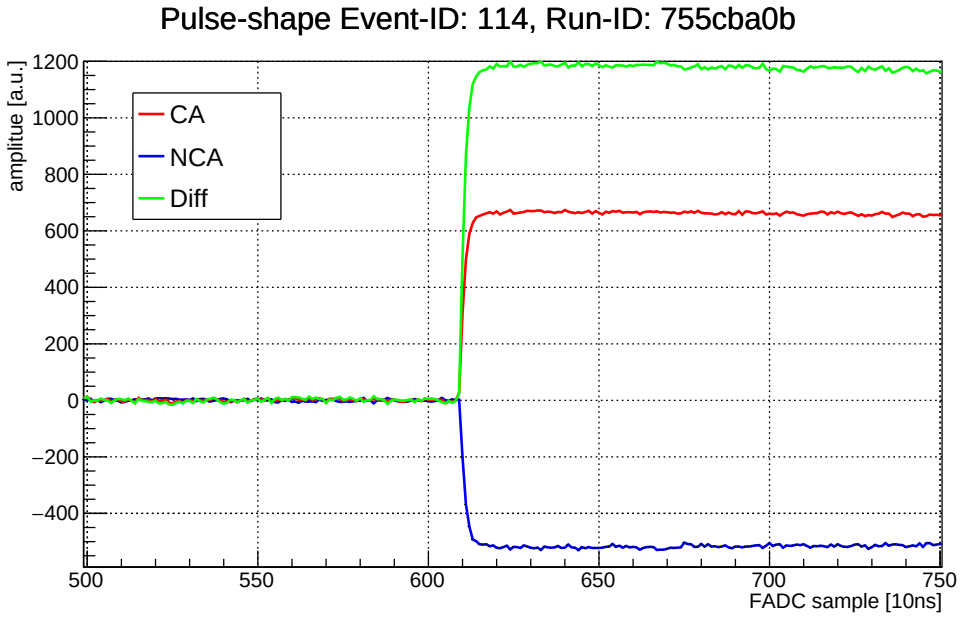

Figure 2.11: An energy deposition in between the CA and NCA rail close to the detector surface can effectively double the reconstructed energy.

detector but at different location. This second interaction happens in a several tens pico-second time scale. For COBRA DAQ, with 100MHz sampling rate (10 ns time resolution) and the slow drift of the charge carriers in the CZT, the second interaction is detected in the same event record as the initial interaction. Due to the different points of interaction, the two charge clouds are reaching the scope of the grid bias at a different time causing an additional rise of the CA signal and drop of NCA signal. Such events are characterized as multi site events (MSE). The identification of MSE can be performed by analyzing the derivative of the difference signal (black line in figure 2.12). By setting a threshold to the amplitude of the derivative signal (pink line in figure 2.12) relative to the root mean square (RMS) of the baseline of the event, a MSE event can easily be identified. If the threshold is exceeded at least twice, the event is very likely MSE caused by a Compton scattered photon or absorption of an annihilation photon. Such identification is important, if events with energy depositions in the range of $0\nu\beta\beta$-energies are detected. By nature $0\nu\beta\beta$-events are single site events, assuming full energy deposition in the same detector. If a $0\nu\beta\beta$-candidate is identified as to be MSE, the event can be dismissed for further considerations. It must be noted, that the sensitivity to distinguish two discrete interactions happening in almost the same depth is identified to be roughly 10% of total detector thickness. Zatschler optimized the MSE cut and implemented it in the Multiple-Analysis Toolkit for the COBRA Experiment (MAnTiCORE) [Zat14].
The application of the MSE cut to a ^{228}Th calibration spectrum is demonstrated in figure 2.13. In the decay chain of ^{228}Th a very high energetic gamma line at 2.614 MeV

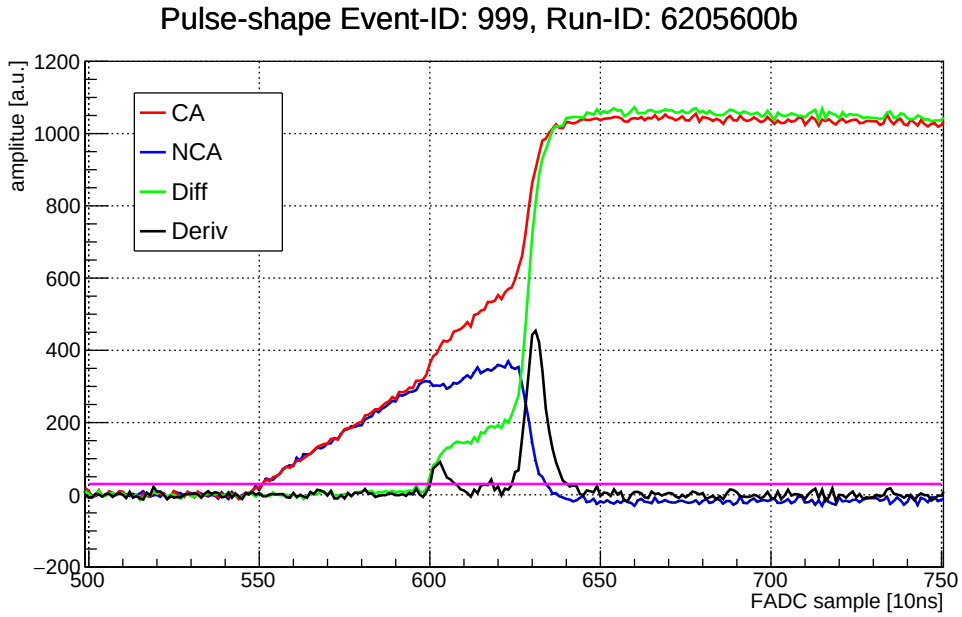

Figure 2.12: Pulse shape of a 2.61 MeV multi site event sampled during a ^{228}Th calibration run.

is emitted, originating from deexcitation of ^{208}Tl. Due to the high energy of this photon, in the interaction a pair creation takes place. Both particles deposit energy close to the point of interaction, which appears to be a single site interaction. At the end of the positrons random walk it annihilates and emits two 511 keV photons. If these two photons also interact in the same detector, full energy deposition at 2.614 MeV (full energy peak - FEP) can be observed. As the two photons are emitted diametrical, it is very likely that they interact in different depths in the detector. Hence, the interaction is likely to be MSE. If one 511 keV photon escapes the detector, an energy deposition at 2.1 MeV - the so called single escape peak (SEP) is observed, if both 511 keV photons escape, the 1.6 MeV double escape peak (DEP) is populated. Such, the SEP must have significant MSE excess whereas the DEP must be mainly SSE. The analysis of the ^{228}Th calibration spectrum supports the phenomenological expectation (figure 2.13). Also the nearly 100% MSE fraction for the events above the 2.6 MeV and the massively increased MSE fraction between FEP and Compton edge are supporting the validity of the identification method.

2.3.3 Lateral Surface Events

As shown in figure 2.8 the weighting potential of the CPG detectors is discontinuous at the sidewalls. For COBRA Demonstrator detectors in floating guard ring configuration the CA forms the outer electrode on two detector sides, at the other two sides the NCA is outer electrode. Thus, for interactions close to the sidewalls, implications to

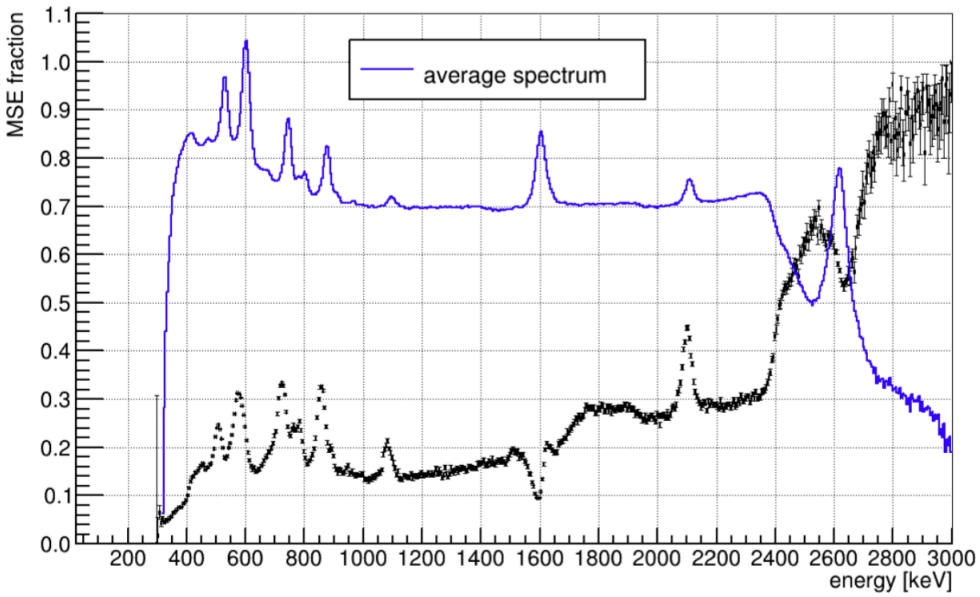

Figure 2.13: ^{228}Th calibration spectrum (blue) with MSE fraction (black) superimposed. Characteristic γ–lines are in coincidence with increased MSE fraction. The dip in MSE fraction for the double escape peak at 1.6 MeV, where both photons escape, and the increased MSE fraction at 2.1 MeV, where only a single photon escapes, is in excellent agreement with phenomenological expectation [Zat14].

the pulse shapes may be expected. The identification of lateral sidewall events (LSE) is important, as they can be caused by α–active contaminations at the detector surface. Fritts and Tebrügge performed extensive investigations to develop methods to identify lateral surface events and to find quantities for automated event identification [Fea14]. Therefore a test-rig has been designed to irradiate the detector sidewalls with α–particles. The observed pulse shapes of CA and NCA lateral side walls showed characteristic distortions compared to bulk events. Again the difference pulse was used to develop the identification method as the effect is most prominent here. The LSE at the CA side is characterized by a slow rise relatively early in the pulse, followed by the standard fast rise. The slow rise is caused by an early split of CA and NCA signal well in advance of the grid bias scope. Such event is referred to as a early rise time event (ERT). For analysis, the number of samples of the pulse rise time from 3% to 50% signal level is evaluated (figure 2.14). The empirical determined value for ERT events are `cal_cpg_diff_ert>8` samples for fast detectors and `cal_cpg_diff_ert>12` samples for slow detectors. The identification of LSE at NCA side is performed at the difference–pulse, too. In case of NCA as outer wall electrode, the difference signal drops significantly below baseline before final signal rise to full amplitude. Here the analyzed value for DIP event identification are ADC channels. Typical DIP events show drops of the difference signal below the baseline of `cal_cpg_diff_rdip<(-50)` (figure 2.15).

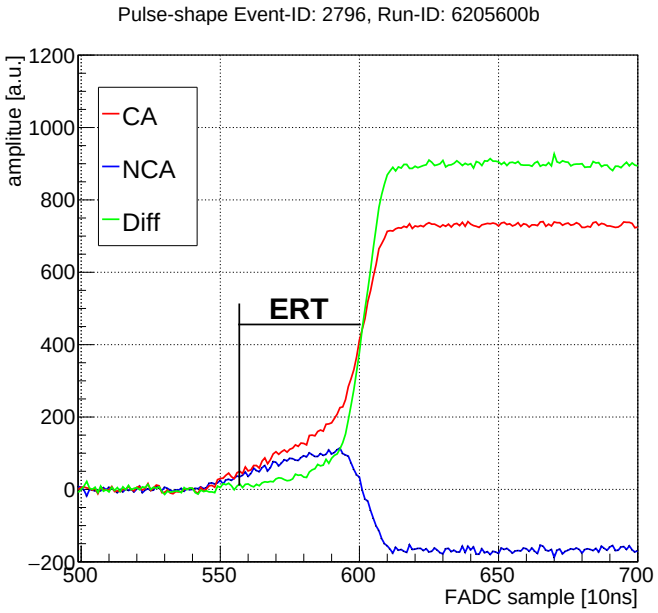

Figure 2.14: Pulse shape sample of an ERT event. The analyzed value is the slow rise of the difference signal before the CA/NCA signal split for the ERT pulse, set to 3% to 50% rise time.

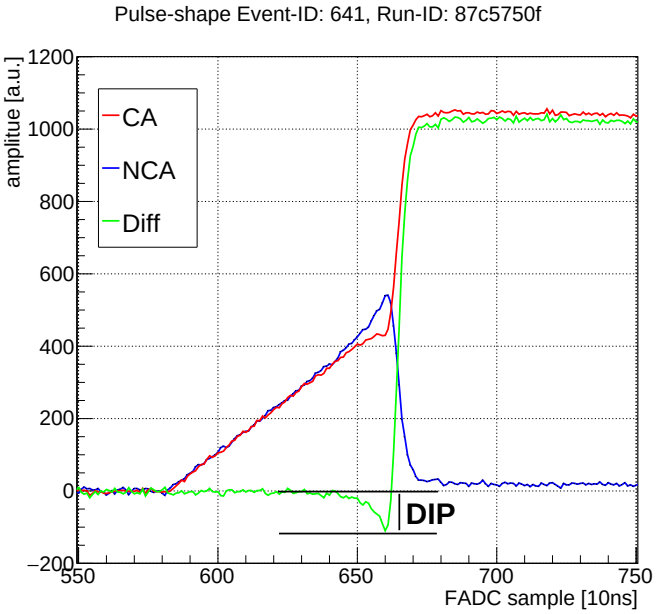

Figure 2.15: Pulse shape sample of a DIP event. The analyzed value is the drop of the difference signal below the baseline level.

3

Investigations on CZT-Detectors for the COBRA-Experiment

3.1 Determination of the Zinc Content

In the periodic table the element zinc, $Z_{Zn} = 30$, is listed in the same chemical main group like cadmium, $Z_{Cd} = 48$, and offers the same number of electronic bonds like cadmium. Hence, it does not act as a dopant, like e.g. lithium in germanium diodes or phosphor in silicon, but simply substitutes the cadmium in the crystal lattice and reduces the total amount of cadmium in the detector. This is important to notice, as the half-life determination of radioactive isotopes depends on the exact knowledge of the total number of source-atoms in the detector. The failure of the unknown zinc concentration is contributing significantly to the uncertainty of the determined half-life of the analyzed cadmium isotopes.

3.1.1 Non-destructive Measurements with EDX and XRF

The determination of the zinc content can be performed with destructive or non-destructive solid-state-analytical methods of which each has its own advantages and disadvantages. The destructive methods, like secondary ion mass spectrometry (SIMS), glow discharge optical emission spectroscopy (GDOES) or inductive coupled plasma mass spectrometry (ICP-MS) can be used for inoperative detectors, only.
The available nondestructive methods are secondary electron microscopy in combination with energy dispersive X–ray spectroscopy (EDX-SEM) or pure X–ray fluorescence spectroscopy (XRF). Both methods analyze the emitted prompt X–rays from the material constituents that are excited by different probes. Both analytical methods require a plain sample surface without any coverage. Hence, the analyzed detector must be stripped off from its protective encapsulation. Therefore, detectors of earlier experiments are used for this investigation as an removal of the encapsulation was needed which leads to rapid performance deterioration. After the analysis, the detectors are reworked by the manufacturer. To remove the red encapsulation lacquer, the detector

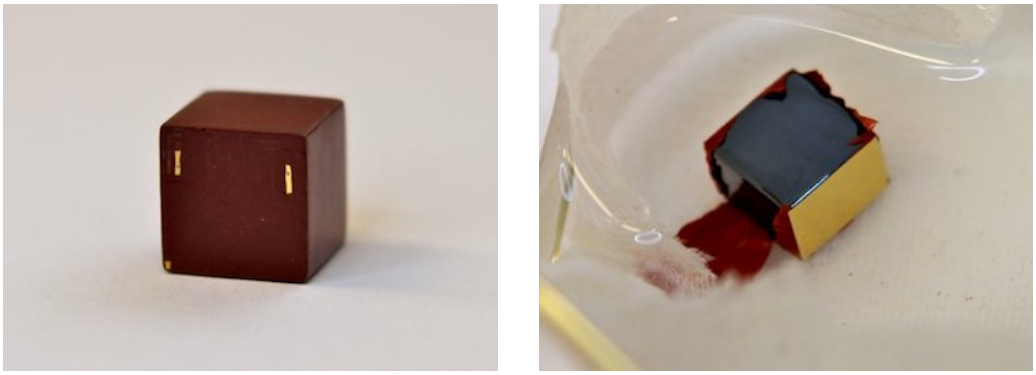

Figure 3.1: Detector preparation for EDX and XRF measurements – prior and during lacquer removal in acetone bath, left: anode side with openings for CA/NCA contacts, right: partially removed lacquer, full coverage gold/platinum-cathode

are bathed in acetone (figure 3.1). After the lacquer removal the detector (detector–ID: 631938-05) is rinsed with 2-propanol and ultra pure water and is dried with clean, compressed air. The EDX measurements are performed at the Technische Universität Dresden at the Institute for Solid-State-Physics. For this analysis the Raster Electron Microscope *CamScan CS44* equipped with an *EDAX Econ3.4 SiLi* detector is used. In the case of EDX-SEM the scanning probe is a 20 keV slightly defocussed electron beam. A spot size of roughly 1 µm^2 is chosen to avoid an overestimation of unrevealed local inhomogeneities. The depth of information (DOI) is inherently limited by the range of the primary electrons and the attenuation of the low energetic X-rays in the analyzed material. A typical EDX-spectra of a CZT-detector is plotted in figure 3.2. For this

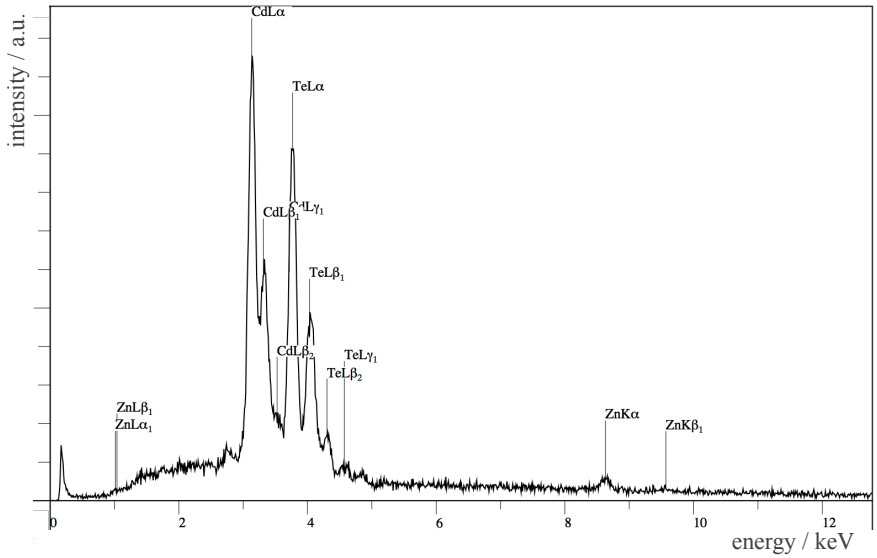

Figure 3.2: Typical EDX-spectra of a CZT-detector. The analyzed area is 1 µm^2. Measurement taken at TU Dresden, Institute for Solid-State-Physics.

Table 3.1: EDX results: sidewall composition of crystal 631938-05, the uncertainty of values below 10 at% is given with 20% relative error

Measurement Pos.	Cd-conc. / (at%)	Zn-conc. / (at%)	Te-conc. / (at%)
1	47.3	4.8	47.8
2	47.3	5.7	47.0
3	47.2	6.0	46.8
4	46.5	4.3	49.2
5	48.7	6.4	44.9
6	47.1	5.5	47.4
7	46.8	4.9	48.3
8	48.7	5.0	46.3
9	45.9	5.9	48.2

setup the DOI is about 1 µm. This illustrates that this technique is not suited to probe for the overall composition of the detector and yields only the near surface stoichiometry. From the measured X–ray intensities the composition of the analyzed material can be deduced. For the quantification, the relative attenuation of the different X-rays in the material have to be taken into account and a homogeneous material composition is assumed. A total of 9 measurements, each 100 sec acquisition time, are taken to analyze the local composition of the detector on the sidewall between the anodes and the cathode. The measured concentration values can be found in table 3.1, figure 3.3 illustrates the surface distribution. The error for the determined concentrations

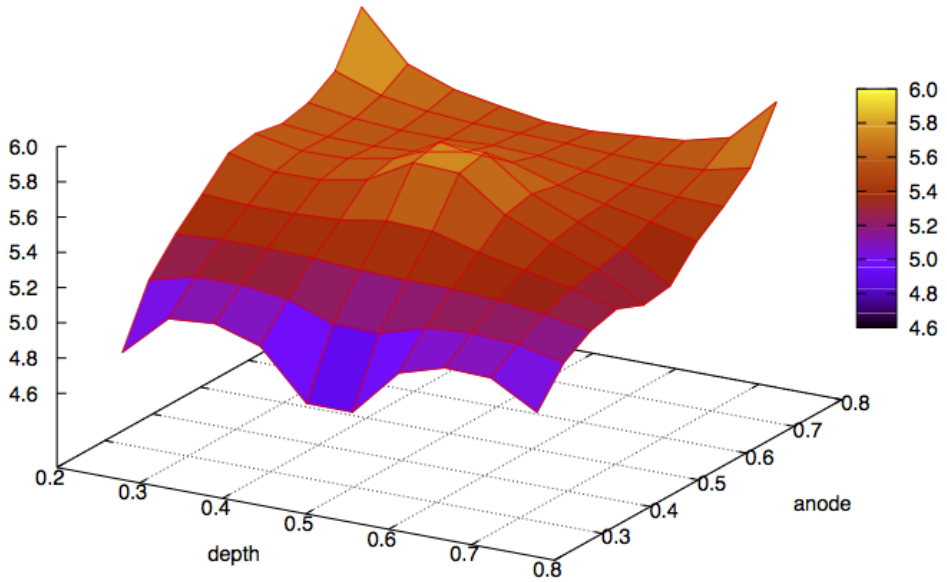

Figure 3.3: Surface-Plot of the measured zinc concentrations of the detector in at%, measurement raster was 2.5, 5 and 7.5 mm in both directions, anode at right side.

is given with 20% relative error of the absolute value, if the values are below 10 at%. The analysis shows, that the gradient of the zinc concentration is not related to the anode–cathode–orientation of the detector. The reason is, that the detector–crystals are cut from the ingot such, that the yield is best, independently of the crystal orientation. In the analyzed sample a zinc concentration gradient is visible. It ranges from $4.6(\pm 0.8) \ldots 5.8(\pm 1.1)$ at% if a plane is assumed.
The X-ray fluorescence (XRF) measurements are performed at *Helmut Fischer GmbH - Institut für Elektronik und Messtechnik (Sindelfingen)*, with a *Fischerscope X-Ray XDV-SDD* spectrometer. For XRF spectroscopy a focused, primary X-ray beam is scanned over the sample surface to induce fluorescence radiation of the materials in use. The energy of the scanning beam has to be high enough to ionize the constituents of the sample. During recombination characteristic X-rays are emitted that can be used to identify elements and to quantify their composition, similar to SEM-EDX measurements. Two different samples are analyzed to quantify the absolute cadmium, zinc and tellurium concentration and to estimate the thickness of the cathode metallization by attenuation measurements. The detected zinc concentrations correlate well with the expected absolute ranges. The first sample (detector-ID 631972.06) shows zinc concentration variations from $c_{zinc} = 5.7(\pm 0.31) \ldots 6.0(\pm 0.31)$ at%. The second sample (detector-ID 631869-06) shows zinc concentration variations from $c_{zinc} = 5.35(\pm 0.56) \ldots 5.92(\pm 0.56)$ at%.

3.1.2 Destructive Measurement with ICP-MS

The third and most sensitive method to quantify the absolute zinc content of a detector is the destructive method *inductive coupled plasma mass spectrometry* (ICP-MS). The measurements are performed at *VKTA - Strahlenschutz, Analytik & Entsorgung* at Helmholtz-Zentrum Dresden-Rossendorf (HZDR). For ICP-MS the detector material has to be pulverized and dissolved in a liquid carrier medium. By obvious reasons, this method was used for a broken, non reworkable detector. The carrier medium is injected in a plasma chamber, where the dissolved material of the CZT detector is ionized, reextracted and analyzed by an attached mass spectrometer. ICP-MS is one of the most sensitive methods, to determine trace contaminants in the parts per million (ppm) to parts per billion (ppb) range. Beside the determination of the zinc content, as the macro-component of the detector, also the analysis of other contaminations, such as thorium and uranium is performed. The result of the zinc analysis reveals for the analyzed detector (detector-ID: 682871-07) a mean zinc concentration of (3.53 ± 0.36)at%. This detector is from a batch that is installed at Layer4 at the COBRA Demonstrator setup at LNGS. For thorium and uranium only a sensitivity of the measurement was given: $m_{Th} < 0.45\,\mu g/kg$ and $m_U < 0.45\,\mu g/kg$. For several other elements measured concentrations are given in table 3.2. Concluding, it has to be noticed, that the available, non–destructive methods (EDX-SEM and XRF) can yield only very local information about the zinc concentration of the detectors. The available DOI is in both cases not sufficient to get integral values for the concentrations of the elements that the whole detector is composed of. The inhomogeneities of the detector and the unclear

Table 3.2: Results of ICP-MS trace component analysis at detector 682871-07 performed by VKTA at HZDR. Determined concentrations in (mg/kg) or the respective sensitivities.

element	(mg/kg)	element	(mg/kg)	element	(mg/kg)	element	(mg/kg)
Li	0.0715	Fe	<0.06	Ag	0.302	Er	<0.005
Be	<0.007	Co	<0.002	In	2.3	Tm	<0.005
B	<0.25	Ni	0.185	Sn	0.169	Yb	<0.02
Na	<4	Cu	0.086	Sb	0.115	Lu	<0.005
Mg	<2	Ga	0.212	Cs	0.025	Hf	0.011
Al	<1	Ge	<0.02	Ba	0.023	Ta	0.032
Si	<1	As	<0.025	La	0.64	W	0.184
P	<0.5	Se	<0.05	Ce	3.42	Re	<0.005
S	<1	Rb	0.015	Pr	4.2	Os	<0.005
K	<2	Sr	0.009	Nd	<0.5	Ir	0.009
Ca	<4	Y	0.001	Sm	<0.5	Pt	0.004
Sc	<0.007	Zr	0.004	Eu	<0.005	Au	<0.025
Ti	<0.25	Nb	0.118	Gd	<0.01	Hg	<0.025
V	3	Mo	<0.003	Tb	<0.005	Tl	<0.005
Cr	<0.06	Ru	0.01	Dy	<0.005	Pb	0.029
Mn	0.011	Pd	0.066	Ho	<0.005	Bi	<0.005

orientation of the zinc gradient makes it basically impossible to obtain values of the total zinc concentration in the specimen better than the currently used 5±2 at%. The destructive method (ICP-MS) yields integral values for the whole detector and is more precise than the non–destructive methods but can be applied only for broken detectors or fragments from the ingot. The observed values for the zinc concentration vary over a wide range for the analyzed detectors. This variation can only partially be attributed to inaccuracies of the measurement method but is mostly generated by inherent variations of the zinc concentration of the grown ingots. For a precise quantification of the number of source atoms as needed for $\beta\beta$-decay search, it is crucial to order fragments from the ingot the detectors are made of. From these fragments ICP-MS measurements result the most accurate information about the integral zinc content of the detector. Table 3.3 concludes the results of the zinc determination results.

Table 3.3: Determined zinc concentrations of different detectors

analytical method	detector–ID	zinc concentration [at%]
EDX-SEM	631938-05	4.6±0.8 . . . 5.8±1.1
XRF	631972.06	5.70±0.31 . . . 6.00±0.31
	631869-06	5.35±0.56 . . . 5.92±0.56
ICP-MS	682871-07	3.53±0.36

3.2 Working Point Determination

The working point of a detector is defined as the point at which the combination of all adjustable operational parameters of a detector result in the best performance of it. In the below discussed case, the working point of the detector is the point with the best energy resolution. This point can differ between detectors, even if they are from the same ingot. The reason for the differing working points of the crystals is based on the physical properties of CZT. The manufacturing of the ternary compound CZT is still a challenging process. During growth, the ionic bound lattice is very susceptible to distortions and tends to form a variety of non-uniformities, such as voids, grain boundaries, dislocations or precipitates that act as charge traps. With the change from High-Pressure-Bridgeman (HPB) to Traveling-Heater-Method (THM) for CZT growth, the number of crystal distortions could be reduced significantly, but the physical effect of the different melting points of the three components ($T_{m(\mathrm{Cd})}$=321°C, $T_{m(\mathrm{Zn})}$=419°C, $T_{m(\mathrm{Te})}$=449°C) can not be compensated.
Charge traps in CZT are dominantly tellurium inclusions formed during crystal growth. In the slow cool-down phase of the stoichiometric melt and the formation of the CZT crystal the high-melting tellurium freezes out early at impurities or lattice distortions and forms inclusions in the crystal that act as trapping zones for charge carriers. CZT manufacturers try to dissolve these inclusions by applying additional annealing steps during the manufacturing process of the CZT boule. That is possible, as the formed CZT-phase has a melting point of $T_{m(\mathrm{CZT})}$=(1100...1150)°C, depending on its stoichiometry. Infrared imaging microscopy shows that this treatment successfully dissolves the tellurium inclusions but the remaining voids still affect the electronic performance. Even if the remaining inclusions are only on size of (10...30) µm their electronic effects are long ranging and can last up to a millimeter around the defect. Moreover, all the other distortions of the crystal, such as the remaining voids, lattice dislocations, grain boundaries and non-dissolvable impurities still degrade the charge transport properties - especially for the slow moving holes. Due to this intrinsic variations, every boule is unique and even the single crystals sliced from the same ingot differ in performance. Hence, each detector has its specific working point that has to be determined separately.

3.2.1 Experimental Setup for Working Point Determination

For the analysis of the working points and the efficiencies of the detectors a dedicated test setup and test procedure is developed. Every detector used in the COBRA Demonstrator, is evaluated for its specific working point and total detection efficiency and is placed in the detector layer according to its performance. The four best performing detectors of the batch are used as inner core of the 4×4 layer, the other 12 detectors are used to shield the inner core. To allow for a nondestructive installation and removal of the detector, a needle based contacting method was used. The needles are made from a corrosion resistant copper-beryllium alloy to ensure a good electrical contact to the electrodes of the collecting anode (CA), non-collecting anode (NCA) and cathode

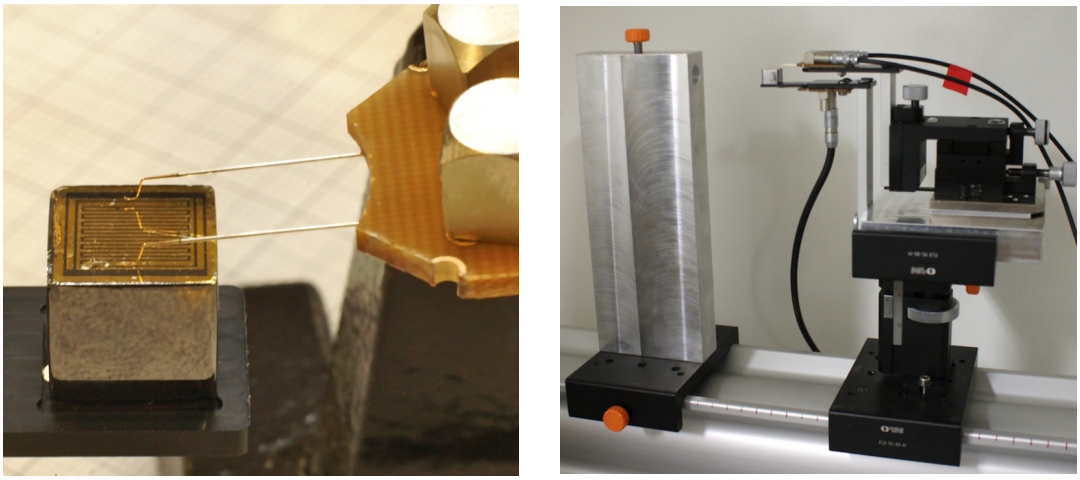

Figure 3.4: Left: Illustration of the non-destructive contacting mechanism of the COBRA detectors for laboratory experiments. The contacting needles are long enough to allow a gentle touch down without inflicting too much strain onto the detector surface. Cathode side contacting is performed accordingly. Right: test setup for working point determination and performance measurements. The radioactive source is placed in the source holder (left side), the detector assembly with the micro manipulator is placed right side. Both devices are mounted on an optical bench for precise alignment.

(CATH) of the detector. The needles are mounted on a printed circuit board - the probe card - that carries the electrical connections to the preamplifier box (figure 3.4). The probe card is installed on a micro-manipulator that allows to move the contact point of the needles in three directions independently and with great precision. It is equipped with a magnetic fixation to install and remove the manipulator quickly without a previous lifting of the needles. The position of the probe card is kept with high accuracy, such, that a quick detector replacement is possible. The combination of probe card and micro-manipulator is used for all subsequently described laboratory experiments performed at TU Dresden (figure 3.4, right side).
For the automated adjustment of the high voltage (HV) and grid bias (GB) the remote controlled power supply unit ISEG SHQ 226L is used. The GB for NCA operation is varied in the range from $U_{\mathrm{GB}} = (40...120)\,\mathrm{V}$, the HV (cathode bias) is varied from $U_{\mathrm{HV}} = (700...1400)\,\mathrm{V}$. The GB was changed in 10 V increments, the HV in 100 V increments. During operation the leakage currents of HV and GB are sensed by the power supply unit, too. Tipping points are set to shut down the power supply if certain leakage currents are exceeded ($I_{max(\mathrm{GB})} < 100\,\mathrm{nA}$; $I_{max(\mathrm{HV})} < 50\,\mathrm{nA}$). Especially for the GB high currents are critical, since the distance between the CA and NCA rails is only 400 µm and extensive leakage could harm the detector.
For each combination of HV and GB the detector is irradiated homogeneously for 600 sec from 5.5 cm distance with a 262 kBq ^{137}Cs source. The test procedure is script controlled and runs completely unattended. The acquisition of the full parameter space of HV and GB takes about a day per detector.

3.2.2 HV/GB Scanning and weighting factor determination

To determine the working point of each detector, the full range of HV and GB is scanned and the energy resolution of the detector is analyzed for each HV/GB combination. In parallel, the optimal weighting factor for each measuring point is evaluated.
The energy resolution is determined at full-width-half-max (FWHM) of the full-energy peak of ^{137}Cs. The fit of the full-energy peak is explained in section 3.4.2. To analyze the energy resolution at its optimal point, the weighting factor w has to be optimized accordingly. The weighting factor is extracted from the two-dimensional plots of the pulse height information of CA and NCA (figure 2.10). Following, the optimal w is evaluated by reprocessing the raw data with different weighting factors and analyzing the achieved energy resolution for the different w for each HV/GB combination. In figure 3.5 this procedure is displayed for three different HV/GB combinations. The

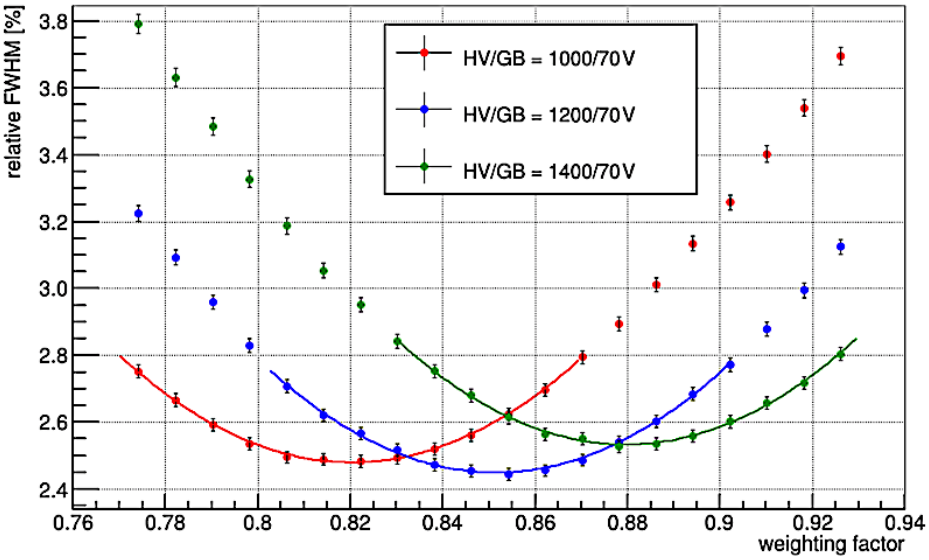

Figure 3.5: FWHM variation as a function of the HV/GB combination and optimized weighting factor w. The working point of the detector is found at the global minimum of FWHM. This defines the optimal HV/GB combination and the corresponding w [Zat14].

optimal weighting factor for the corresponding HV/GB combination is obtained by an application of a quadratical fit to achieve the best energy resolution for the detector. The extraction of the point of minimal FWHM from all measured combinations results in the optimal HV/GB combination and the corresponding weighting factor – the working point of the detector. The determined working points, weighting factors and corresponding energy resolution of the detectors used at COBRA Demonstrator are listed in table 3.4. The measured energy resolution in dependency of the GB/HV-combination with optimized w of detector Det40 is shown in figure 3.6.
In the second step, the full energy efficiency of each detector at its working point is analyzed. This is done by an evaluation of the number of full-energy peak entries in

3σ, covering 99.7% of the counts (figure 3.7). This analysis is performed for all detectors used in the COBRA Demonstrator installed at the LNGS. The detectors are operated at their specific working point if no contrary reasons are given (e.g. increased noise due to enhanced leakage). The measured energy resolutions of the detectors used in COBRA Demonstrator at their optimal working conditions are in the range of $E_{res} = (1.7 \ldots 4.9)\,\%$ at 662 keV.
For future large scale applications a more time efficient approach has to be developed to determine the optimal working point of the detectors in use. An improved approach could be based on a measurement of the leakage currents during calibration runs of the readily installed detectors. The installed electronics allows for such investigation.

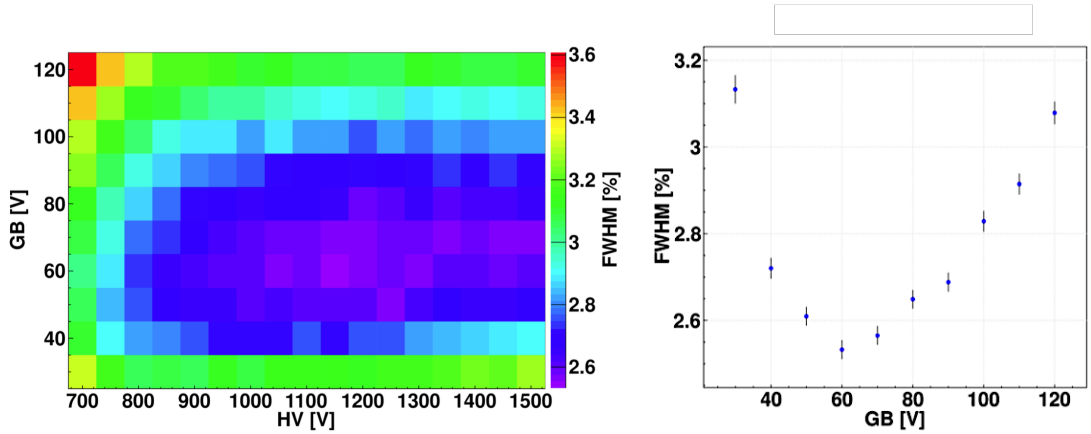

Figure 3.6: Left: Energy resolution distribution of Det40 as a function of HV/GB variation. The performance is best at $U_{HV} = 1150\,\text{V}$ and $U_{GB} = 60\,\text{V}$. Right: energy resolution as a function of the GB at fixed HV [Wes12].

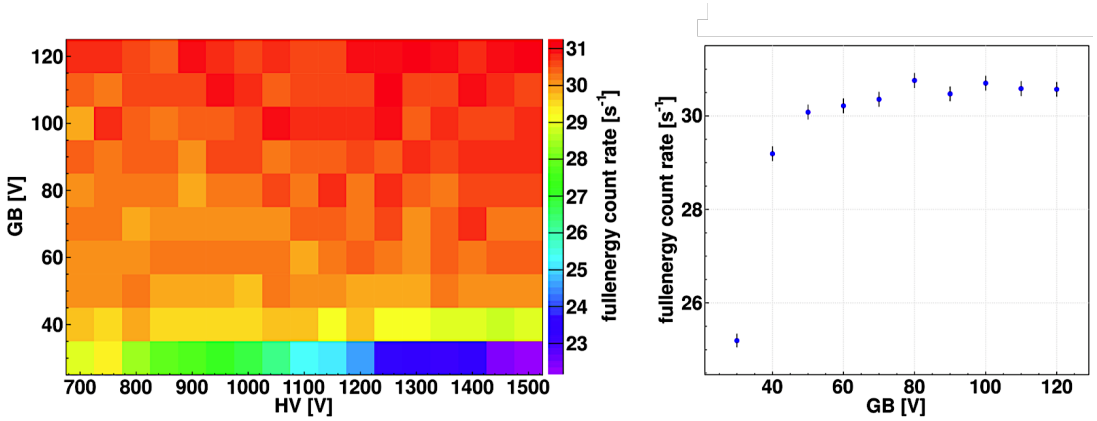

Figure 3.7: Left: full-energy peak count-rate distribution of Det40 as a function of HV/GB variation. A trent to better performance is found for higher GB and HV values. Right: full-energy count-rate as a function of the GB at fixed HV [Wes12].

Table 3.4: Results of working point determination of the detectors of Layer1 to Layer4 of the detectors currently installed at COBRA Demonstrator at LNGS.

Det_ID	HV (V)	GB (V)	weight.-factor w	energy res. (%)	Det_ID	HV (V)	GB (V)	weight.-factor w	energy res. (%)
Det1	1300	90	0.80	3.80	Det33	1000	50	0.71	3.23
Det2	1300	90	0.87	2.70	Det34	1200	40	0.82	2.89
Det3	1500	80	0.83	3.58	Det35	1500	90	0.80	3.06
Det4	1300	90	0.83	3.60	Det36	1100	40	0.74	3.12
Det5	900	60	0.90	2.60	Det37	1500	100	0.76	2.77
Det6	1200	70	0.95	2.38	Det38	1400	80	0.75	2.65
Det7	1200	80	0.91	2.50	Det39	1500	90	0.81	2.27
Det8	1200	90	0.88	2.70	Det40	1400	110	0.74	2.67
Det9	1200	70	0.83	2.95	Det41	1500	70	0.75	2.77
Det10	1100	100	0.82	2.40	Det42	1500	80	0.78	2.66
Det11	1100	90	0.95	2.38	Det43	1400	100	0.74	2.52
Det12	1300	100	0.84	2.70	Det44	1400	80	0.74	2.70
Det13	1400	50	0.88	3.70	Det45	1300	50	0.78	3.28
Det14	1300	80	0.89	2.80	Det46	1500	100	0.71	2.86
Det15	1100	70	0.86	2.70	Det47	1100	40	0.75	3.04
Det16	1300	90	0.83	3.45	Det48	1300	50	0.80	3.11
Det17	1100	50	0.86	3.50	Det49	1500	50	0.82	3.11
Det18	1300	90	0.79	2.56	Det50	1100	40	0.93	2.01
Det19	1500	90	0.91	2.70	Det51	1300	60	0.91	2.04
Det20	1300	70	0.81	3.10	Det52	1200	80	0.90	2.19
Det21	1100	50	0.81	2.74	Det53	1500	90	0.80	2.58
Det22	1000	70	0.90	2.38	Det54	1200	40	0.93	1.86
Det23	1200	70	0.83	2.70	Det55	1100	60	0.90	1.71
Det24	1500	60	0.82	3.27	Det56	1400	60	0.87	2.23
Det25	1150	60	0.85	2.60	Det57	1500	50	0.81	2.57
Det26	1100	70	0.89	2.50	Det58	1200	40	0.90	1.89
Det27	1300	80	0.92	2.40	Det59	1200	60	0.90	1.99
Det28	1100	80	0.64	4.90	Det60	1500	40	0.88	2.18
Det29	1200	70	0.80	3.80	Det61	1500	50	0.86	2.51
Det30	1000	40	0.89	3.10	Det62	1100	50	0.78	2.13
Det31	1300	110	0.86	2.80	Det63	1500	60	0.82	2.88
Det32	1200	110	0.79	3.60	Det64	1100	50	0.80	3.22

3.2.3 Determination of Total Detector Efficiency

The total detection efficiency describes the ratio of the number of incident particles to the number of detected events with full energy deposition. It is a very critical parameter, as the sensitivity of the COBRA experiment is directly proportional to the detector efficiency (equation 2.13). In the half-life calculation usually the detector mass is considered, assuming the full detector to be sensitive for event registration. The assumed efficiency ϵ in equation 2.13 represents the probability for full energy deposition of the two electrons emitted in the expected $0\nu\beta\beta$-decay and is derived from particle transport simulations with GEANT4. As described above, CZT suffers from inhomogeneities that affect the efficiency of charge transport and total efficiency not included in the GEANT4 simulations. For this reason a screening of the detectors is performed prior installation.
For the determination of the total detection efficiency the same setup as described in section 3.2.2 is used. The detectors are irradiated homogeneously with the γ-radiation of a ^{137}Cs-source from five distances, ranging from $d = (5 \ldots 15)\,\mathrm{cm}$, and for a duration of 10 min. For the total efficiency determination the events in the full-energy peak of the ^{137}Cs are evaluated. In this configuration the radioactive source can be treated as a point source, the attenuation in the air is dismissed. The detectors are operated at their specific working point (section 3.2). Under this conditions the number of events in the full-energy peak only depends on the distance between the detector and the radioactive source and can be described as:

$$N_{FEP} = A \cdot t \cdot \epsilon \cdot \frac{F}{4\pi r^2}. \tag{3.1}$$

N_{FEP} is the number of entries in the full-energy peak, A is the activity of the radioactive source, F is the irradiated area of the detector, here $F = 1\,\mathrm{cm}^2$, and r is the distance between source and detector. The only variable in this equation is the efficiency ϵ, which is used as fitting parameter (figure 3.8).

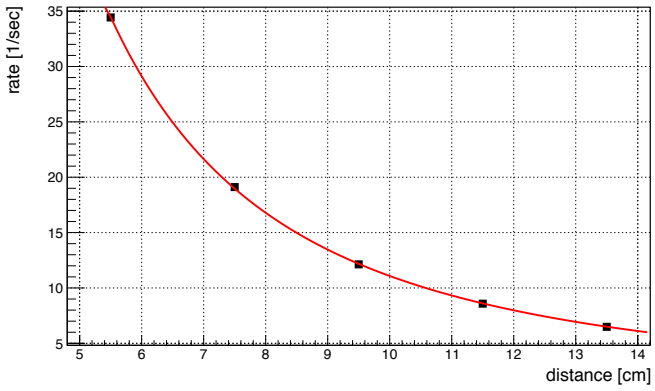

Figure 3.8: Fit of the count rate for the $E = 662\,\mathrm{keV}$ full-energy deposition in a single $1\,\mathrm{cm}^3$ CZT COBRA Demonstrator detector irradiated with a 262 kBq ^{137}Cs source at different distances.

The average total efficiency for the detection of 662 keV γ-rays of Layer1 and Layer2 detectors is determined to be $\epsilon_{(662\,\mathrm{keV})} = (5.28 \pm 0.21)\%$ (table 3.5). This value is valid only for the full-energy detection of the 662 keV γ-rays and must not be compared to the detection efficiency for β-processes. The GEANT4 simulated value of $\epsilon_{(2\beta)} = 49\%$ is valid for the kinetics of the neutrinoless double-beta decay of ^{116}Cd at Q=2.16 MeV in the 1 cm^3 CZT detectors of the COBRA Demonstrator. The values differ, as the $\epsilon_{(662\,\mathrm{keV})}$ describes the probability of a photon at this energy to interact in the CZT, whereas the $\epsilon_{2\beta}$ describes the chance of the electrons generated in the CZT to deposit their full energy in the detector. Nevertheless, the determined $\epsilon_{(662\,\mathrm{keV})}$ is a valuable result to relatively compare the detectors in use. In table 3.5 the measured total efficiencies, the detector mass prior passivation and the relative efficiency of the detectors of Layer1 and Layer2 are listed. The normalization of the total efficiency to the mass of the detector allows to identify detectors that differ from average layer performance.

Table 3.5: Total efficiencies of detectors of Layer1 and Layer2

Det_ID	batch_ID	layer pos.	total efficiency/(%)	mass/(g)	rel. efficiency/(%/g)
Det1	668004-06	LNGS-L1-P1	5,61	5,900	0,951
Det2	668007-01	LNGS-L1-P2	5,41	5,889	0,919
Det3	681165-17	LNGS-L1-P3		6,242	
Det4	668004-02	LNGS-L1-P4	5,73	5,906	0,970
Det5	667467-05	LNGS-L1-P5	5,15	5,858	0,879
Det6	667470-03	LNGS-L1-P6	5,13		
Det7	667467-03	LNGS-L1-P7	5,17	5,833	0,886
Det8	667467-04	LNGS-L1-P8	5,10	5,852	0,871
Det9	668005-01	LNGS-L1-P9	5,39	5,893	0,915
Det10	668007-05	LNGS-L1-P10	5,27	5,905	0,893
Det11	667470-02	LNGS-L1-P11	5,18		
Det12	668006-01	LNGS-L1-P12	5,54	5,903	0,939
Det13	667617-03	LNGS-L1-P13	5,42	5,861	0,925
Det14	668007-02	LNGS-L1-P14	5,15	5,906	0,872
Det15	668005-03	LNGS-L1-P15	5,22	5,867	0,890
Det16	668004-04	LNGS-L1-P16	5,69	5,905	0,964
Det17	667617-02	LNGS-L2-P1	5,32	5,869	0,907
Det18	668005-05	LNGS-L2-P2	5,14	5,874	0,875
Det19	667470-01	LNGS-L2-P3	5,18		
Det20	668005-02	LNGS-L2-P4	5,38	5,877	0,915
Det21	668005-04	LNGS-L2-P5	5,01	5,866	0,854
Det22	667467-02	LNGS-L2-P6	5,21	5,854	0,890
Det23	668005-06	LNGS-L2-P7	5,10	5,905	0,864
Det24	682872-05	LNGS-L2-P8		5,724	
Det25	667989-02	LNGS-L2-P9	5,43		
Det26	667468-02	LNGS-L2-P10	5,28		
Det27	667468-01	LNGS-L2-P11	5,09		
Det28	632083-02	LNGS-L2-P12	5,33	6,529	0,816
Det29	667989-03	LNGS-L2-P13	5,56		
Det30	667615-04	LNGS-L2-P14		5,860	
Det31	667989-01	LNGS-L2-P15	4,89	5,885	0,831
Det32	667467-01	LNGS-L2-P16	5,03	5,867	0,857

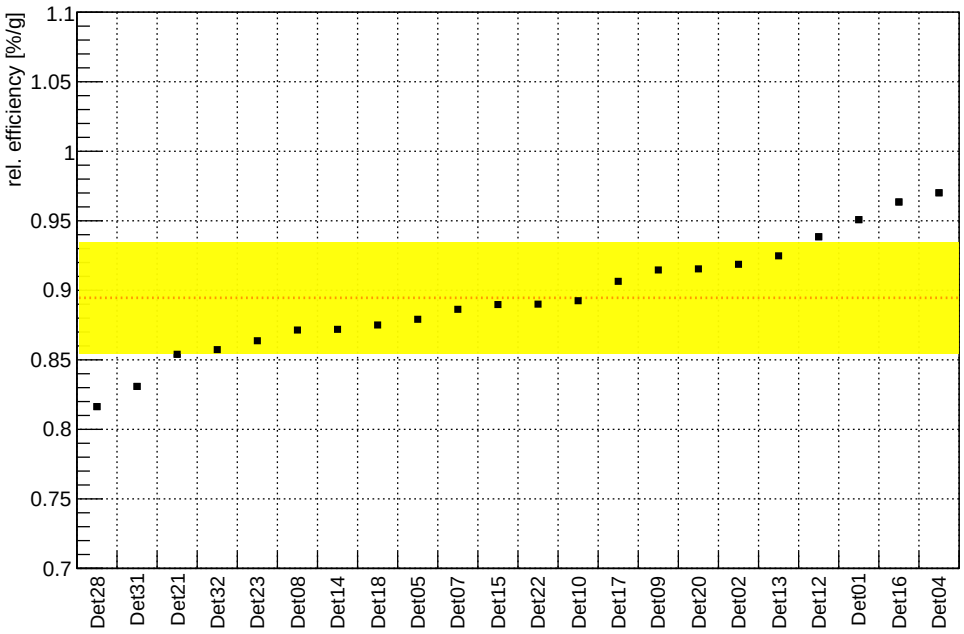

Figure 3.9: The total efficiency normalized to detector mass of detectors from Layer1 and Layer2. The detectors are ordered with regard to their relative efficiency. The mean relative efficiency is $\epsilon_{rel} = (0.89 \pm 0.04)\%/\mathrm{g}$ for the full-energy detection of 662 keV photons.

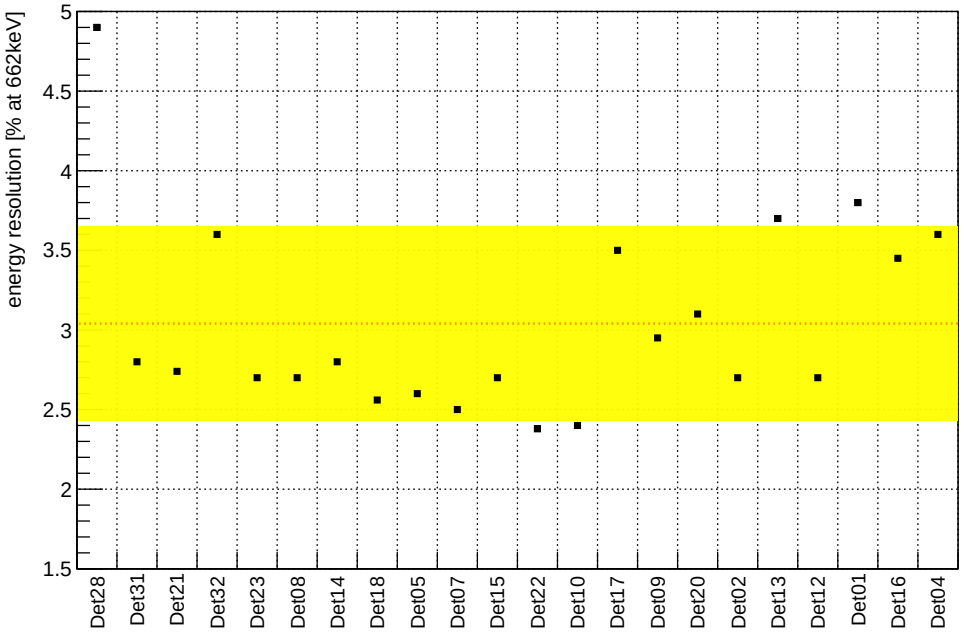

Figure 3.10: Energy resolution of the above displayed detectors in same order. No clear correlation is derivable. The mean energy resolution is $E_{res} = (3.04 \pm 0.61)\%$ at 662 keV.

3.3 Temperature Scaling Experiments

3.3.1 Experimental setup

Gentle cooling reduces surface- and bulk-leakage currents and can potentially enhance the observed energy resolution of CZT detectors [ALL06]. In 2009 Dawson et al performed investigations on the effect of moderate cooling on COBRA CZT detectors [DMR+09]. Improvements in energy resolution and low energy threshold were observed. To test the influence of cooling of the detectors used for COBRA Demonstrator setup in combination with cooling of the preamplifiers, a special test setup is developed. To allow EMI shielding of the detector during temperature scaling experiments, a miniaturized EMI box for the detector mounting is manufactured. It features a shielded high voltage, grid bias and collecting anode feedthrough (figure 3.11). To perform

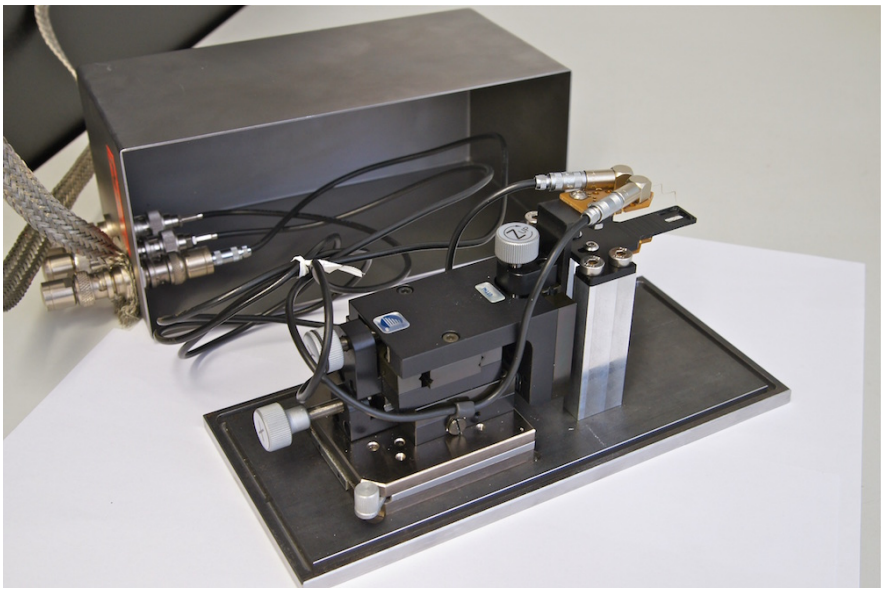

Figure 3.11: The micro-manipulator installed in the EMI shielding box for temperature scaling and laboratory experiments. The detector is placed on the black plastic support on the right hand side. The cathode connection is performed with the cathode probe card (bottom side) through the hole in the support structure. The thick mesh band connected to the feed trough is for grounding of the box.

the temperature scaling experiments, a thermal isolated cooling box is prepared. The cooling box houses the cooling device, the preamplifier box, the CZT detector in the EMI shielding box and the radioactive source (figure 3.12 and 3.13). Cooling is possible in the range of $T_{det} = (-5 \cdots + 25)°\mathrm{C}$. For all measurements pulser signals are injected directly into the input of the preamplifier to monitor the impact of cooling to the width of the pulser peak in the spectrum and allow to analyze the performance gain due to reduction of electronic noise. For this purpose a *Berkeley Nucleonics PB4* pulser is set to inject rectangular 20 µs long pulses with an amplitude of $U = 100\,\mathrm{mV}$ at the shortest

Figure 3.12: The thermal isolated cooling box on the table, chiller device below the table, electronics rack with power supply, pulser, FADCs, computer on right hand side.

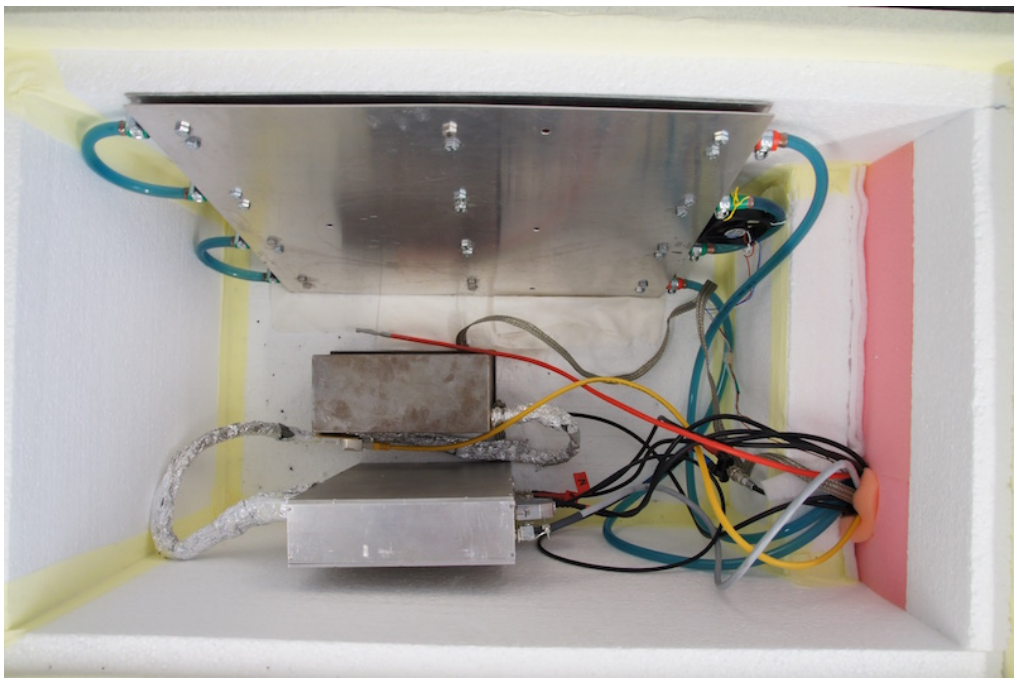

Figure 3.13: View into the cooling box. Back: cooling device, middle: EMI shielding box with detector mounting, front: preamplifier box. Red cable: temperature sensing device.

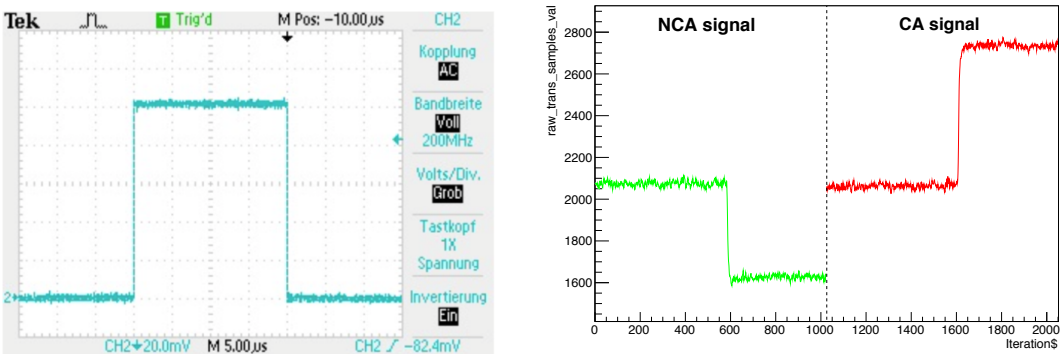

Figure 3.14: Left: injected pulser signal with a duration of $t = 20\,\mu s$, screen-shot from oscilloscope, right: sampled pulse shape of pulser signal with 10 µs sample length

possible rise-time of $t_{rise} = 16\,ns$. The typical rise-time of the CZT signals is in the range of 1 µs, depending on the depth of interaction in the crystal and the deposited energy, and is much slower than the rise-time of the pulser signal. The length of a recorded event is 10.24 µs and only half as long as the injected pulse itself. With these parameters the record of the injected pulse results in a steep, approximately two samples long rising edge and a flat top (NCA channel is inverted, figure 3.14). The noise of the baseline is a result of the overall noise in the system, including the detector noise. Deviations in the amplitude of the injected pulses are directly correlated to the noise of the readout chain and are independent of the detector noise. For testing purposes and to exclude possible instabilities of the pulser input, the signal is directly connected to the FADC input and compared to the same signal injected into the full DAQ chain. The analysis reveals, that the DAQ chain smears out the injected signal significantly. The directly injected pulser signal shows a standard deviation of $\sigma_{direct} = 0.8$, whereas the standard deviation of the same signal fed through the full DAQ chain shows a width of $\sigma_{DAQ} = 6.0$ (figure 3.15). No relative values are given, as the standard deviation for the injected pulses is nearly independent on the position of the mean value in the

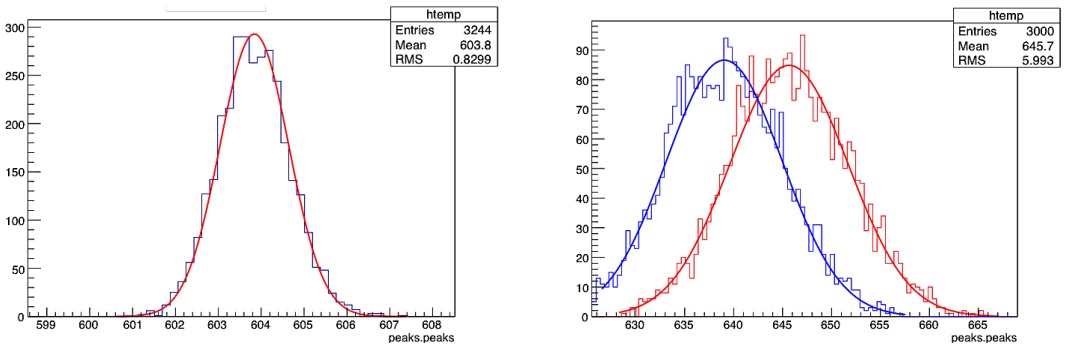

Figure 3.15: Left: Pulse directly injected into the FADC, $\sigma_{direct} = 0.8$; Right: pulse injected through the full DAQ chain, $\sigma_{DAQ} = 6.0$, tested on two different FADC channels

spectrum. The temperature dependency of the σ of the pulser peak is shown in figure 3.16. A reduction of the σ of the pulser peak of circa 10% is observed for a reduction of the ambient temperature from 15.6°C to -1.7°C. For these measurements the pulser is set to a repetition rate of $f = 30\,\mathrm{Hz}$ to be almost on a par with the full energy deposition rate of the ^{137}Cs source in the investigated detector (figure 3.17).
To test for shifts of the working point of the detector, a programmable power supply for high voltage and grid bias is used. As a wide range of working points at different temperatures has to be scanned, an automated measurement routine is programmed for unattended operation. The high voltage is varied from $U_{HV} = (800 \ldots 1500)\,\mathrm{V}$ in 100 V steps, the grid bias is varied from $U_{GB} = (30 \ldots 110)\,\mathrm{V}$ in 10 V steps. For each combination a spectrum is taken for 10 min. For the analysis of temperature driven performance alterations, a gaussian fitting algorithm is applied to the full energy peak of ^{137}Cs for each spectrum, accordingly. The measured peak width of the FEP is given in standard deviations in figure 3.18 for the different combinations of HV and GB as well as for different temperatures.
Especially for the lower temperatures a clear shift of the working point to higher grid bias voltages is visible. At room temperature the working point of this detector is determined to be $U_{HV} = 1500\,\mathrm{V}$ and $U_{GB} = 30\,\mathrm{V}$. For the lowest temperature the best energy resolution is clearly shifted and can be found at $U_{GB} = 90\,\mathrm{V}$. The energy resolution of the detector is also high voltage dependent and should be set to highest possible voltages. For operation at lower temperatures and elevated grid bias voltages the high voltage can be lowered slightly with no performance degradation. At the lowest temperature the working point of this detector is shifted to $U_{HV} = 1400\,\mathrm{V}$ and $U_{GB} = 90\,\mathrm{V}$. The energy resolution is reduced from 13.6 to 12.4 which equals roughly 9% relative improvement. The improvement can mainly be attributed to reduced surface and bulk leakage currents. The increased drift performance of the electrons due to reduced lattice vibrations and thereby caused reduced recombination contributed further to the performance gain. The observed effect is very detector specific and must not be over-simplified. To test for the reproducibility of the observed shift of the working point, another two detectors (Det15, Det16) are tested with the same HV/GB-scanning at 0 °C (figure 3.19).
It is visible, that the optimal performance of the individual detectors varies with the HV/GB settings and temperature. For the analyzed detectors with decreasing temperature a tendency can be found, that points to higher HV and higher GB whereas not always the highest possible voltage combination result in best performance. Therefore, a careful individual performance screening for each detector is necessary. In this work the performance improvements are analyzed only for the full energy peak of ^{137}Cs. It turned out, that energy resolution improvements in the 10% range can be observed by lowering the temperature from 22.7 °C to about 0 °C.

3.3.2 Temperature Dependency of the Mobility-Lifetime-Product

To analyze the temperature dependency of the mobility lifetime product, the measurements of the previous section and the reevaluated data from Kresse [Kre17] are used.

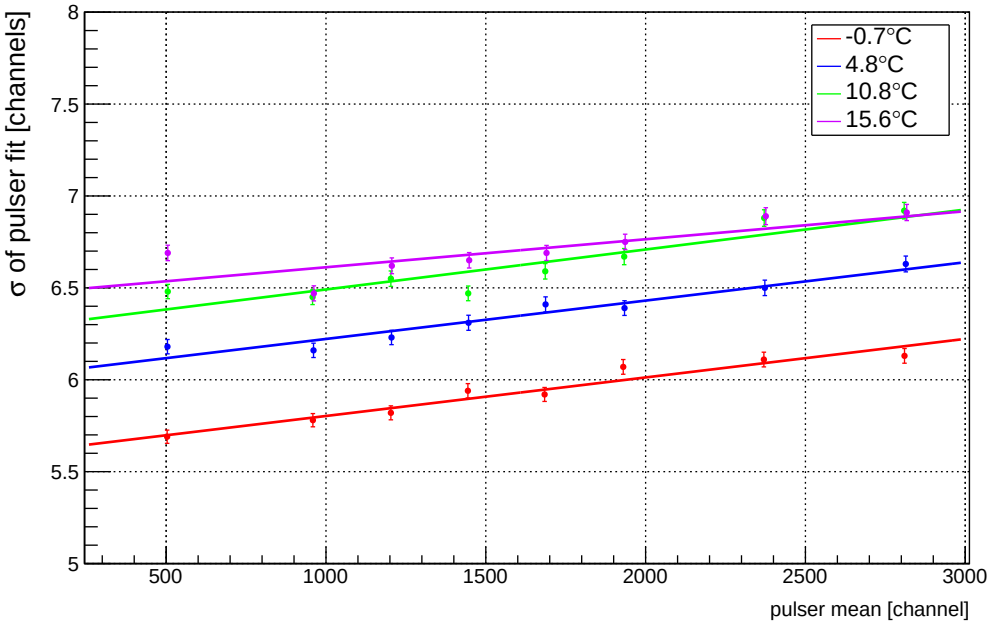

Figure 3.16: The standard deviation of the injected pulser signal is analyzed at different positions of the mean (proportional to energy) and at four temperatures. With decreasing energy a steady reduction of the peak width (σ) was observed. A linear approximation is superimposed. The observed reduction is in the same order as the performance gain for the CZT detector ($\sim 12\%$ at channel 1000).

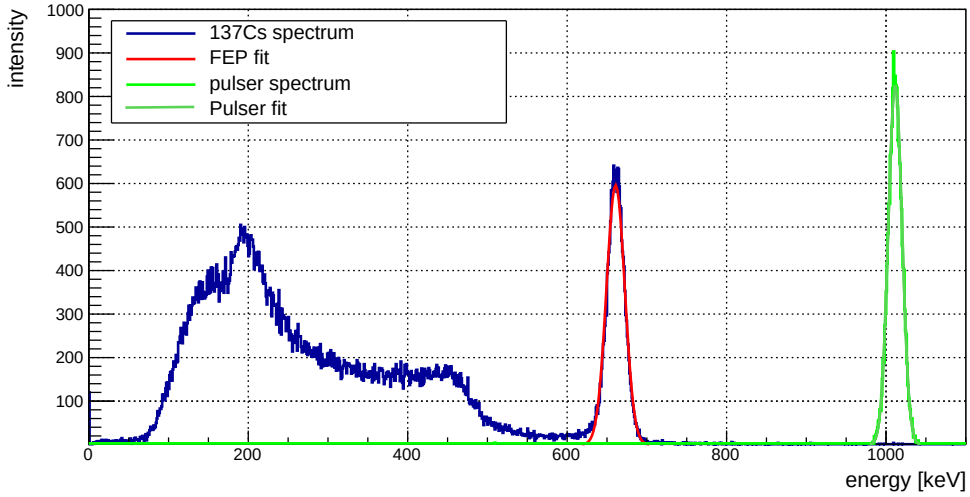

Figure 3.17: ^{137}Cs spectrum of temperature scaling experiment with injected pulser at 1 MeV (Det21 at $U_{HV} = 1500\,\mathrm{V}$ and $U_{GB} = 30\,\mathrm{V}$ at 10.7°C) Superimposed are the fits for the full-energy peak and the injected pulser peak.

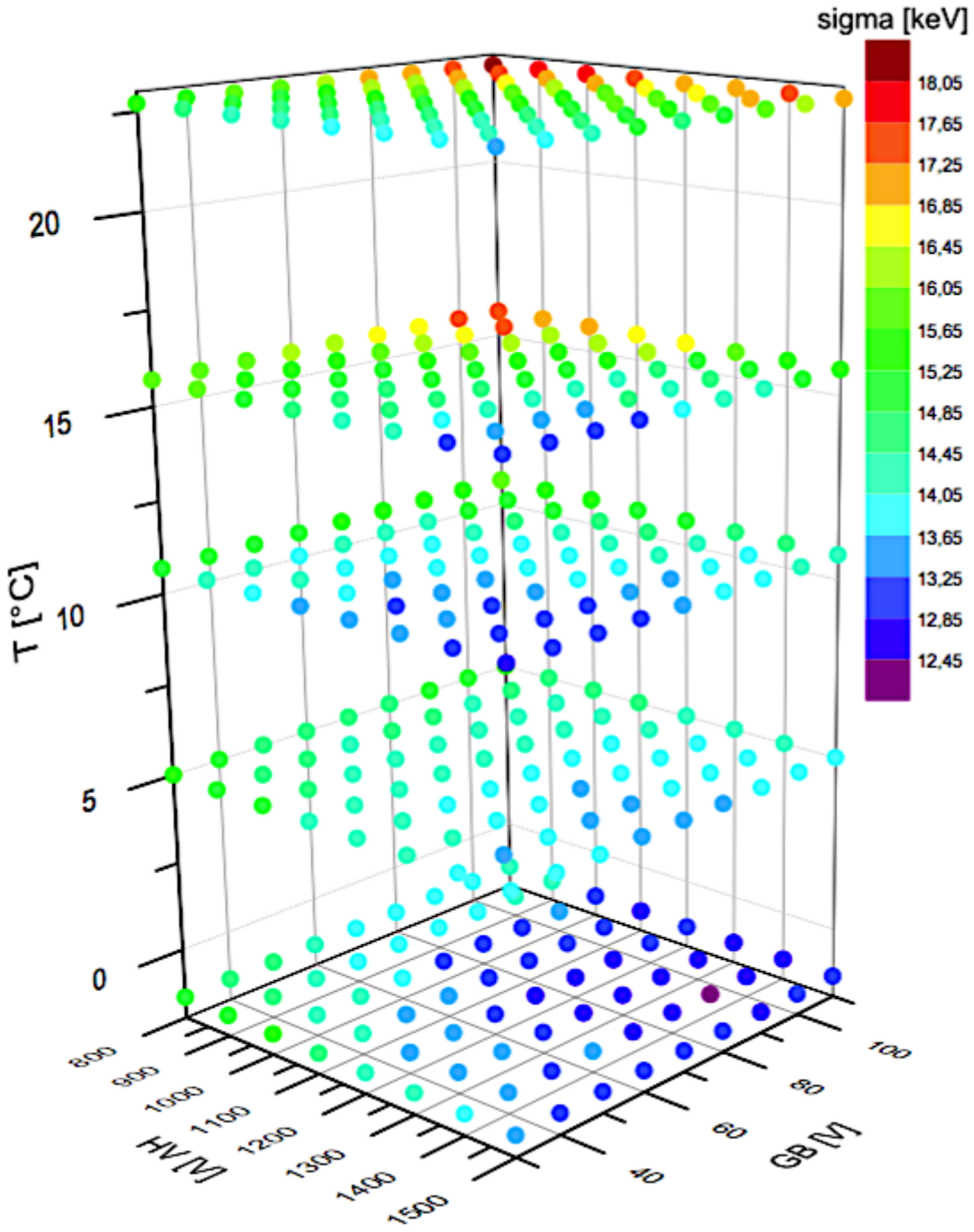

Figure 3.18: Temperature dependency of the energy resolution of the detector. The standard deviation of the full energy peak is color-coded. The detector performance is tested over a wide range of HV/GB combinations at five different temperatures. A clear shift of the working point of the detector to higher grid bias values for decreasing temperature is visible.

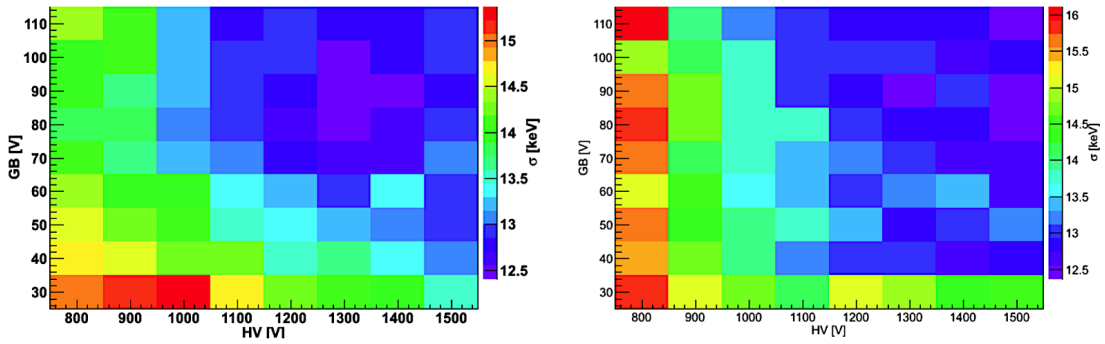

Figure 3.19: Determination of the working point of two detectors (Det15, Det16) at 0 °C. Left: Working point set to $U_{HV} = 1300\,\mathrm{V}$ and $U_{GB} = 90\,\mathrm{V}$, Right: Working point set to $U_{HV} = 1500\,\mathrm{V}$ and $U_{GB} = 90\,\mathrm{V}$

The shift of the working point indicates that the electric properties of the detectors change in dependency of a changing ambient temperature.
To analyze interactions of the same energy and of the same point of interaction in terms of depth between the anodes and the cathode, the improved depth reconstruction of Fritts et al is used [Fea13]. The depth of interaction can be calculated by analyzing the height of CA and NCA signal and w as weighting factor:

$$z = \left(\frac{1+w}{1-w}\right) \cdot \ln\left(\frac{1-w}{1+w} \cdot \frac{CA+NCA}{CA-NCA}\right) \tag{3.2}$$

The heat-plot in figure 3.20 displays the z *over* E distribution of a ^{137}Cs irradiation of a COBRA Demonstrator detector. In this type of plot the anodes are at $z = 0$ and the cathode is at $z = 1$. The vertical band at $E = 662\,\mathrm{keV}$ indicates the full energy depositions. The anode near distortions are described in section 2.2.3.
To analyze the impact of the temperature to the drift velocity of the charge cloud, the drift time of the charge carriers are probed using the NCA signal. The NCA signal is chosen as it rises continuously with the drift of the charge cloud throughout the detector and drops fast if it reaches the scope of the weighting field. The longest drift times are expected for interactions next to the cathode, therefore a combined energy-/depth-cut is applied (`cal_ipos_ztc>0.9 && cal_ipos_ztc<1.0 && cal_edep>600 && cal_edep<700`). The mobility of the charge carriers in dependency of the measured drift time ($\mu(\tau_{max})$) is extracted from the measured drift velocity and can be expressed by following equations (only electrons are regarded):

$$v_{drift} = \mu \cdot E = \mu \cdot \frac{HV - \frac{1}{2}GB}{L} = \frac{L}{\tau_{max(T)}} \tag{3.3}$$

$$\Longrightarrow \mu(\tau_{max(T)}) = \frac{L^2}{\tau_{max(T)} \cdot (HV - \frac{1}{2}GB)} \tag{3.4}$$

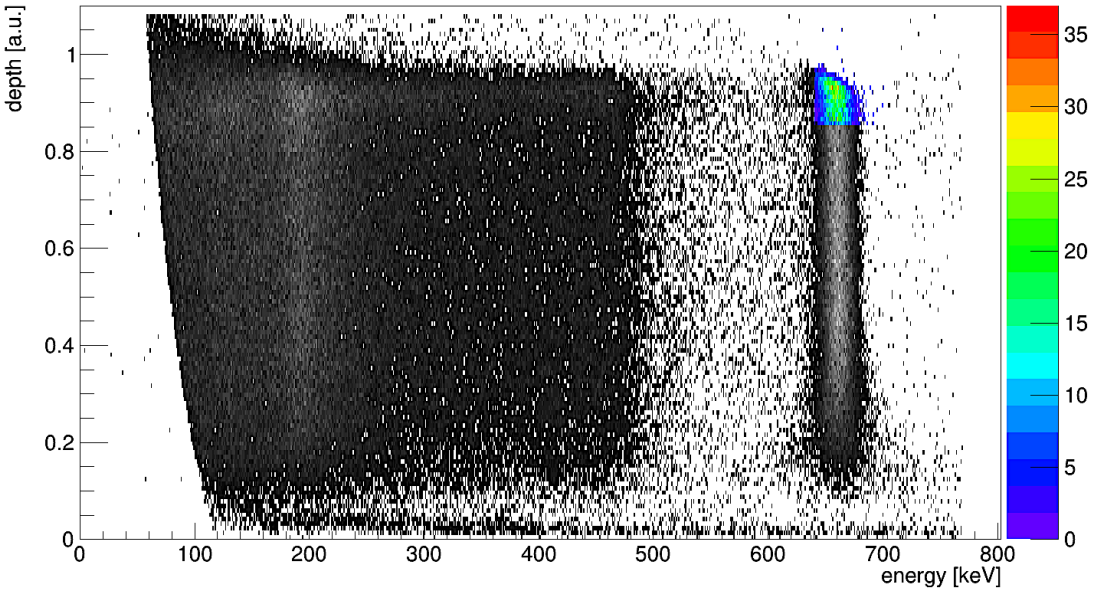

Figure 3.20: Heat-Plot of a homogeneous ^{137}Cs irradiation of a COBRA Demonstrator detector (Det21) at its working point ($U_{HV} = 1300\,\mathrm{V}$ and $U_{GB} = 30\,\mathrm{V}$). The colored events are used for up-slope analysis.

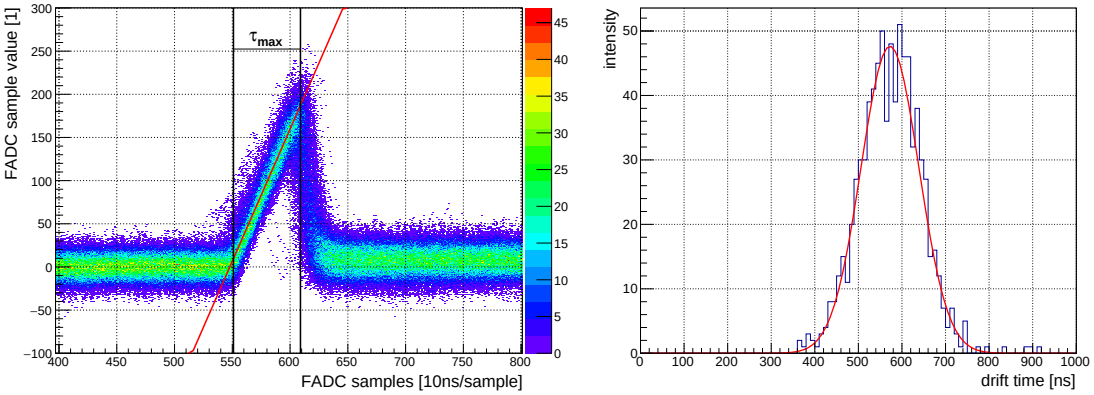

Figure 3.21: Left: overlay of selected NCA signals from figure 3.20 with linear regression of the signal slope (red) for the 20% to 80% signal range superimposed. The mean of the drift time (τ_{max}) is marked too. Right: histogram of the determined drift times for $U_{HV} = 1300\,\mathrm{V}/U_{GB} = 30\,\mathrm{V}$ at 22°C and combined $E-$ and $z-$cut with superimposed gaussian fit.

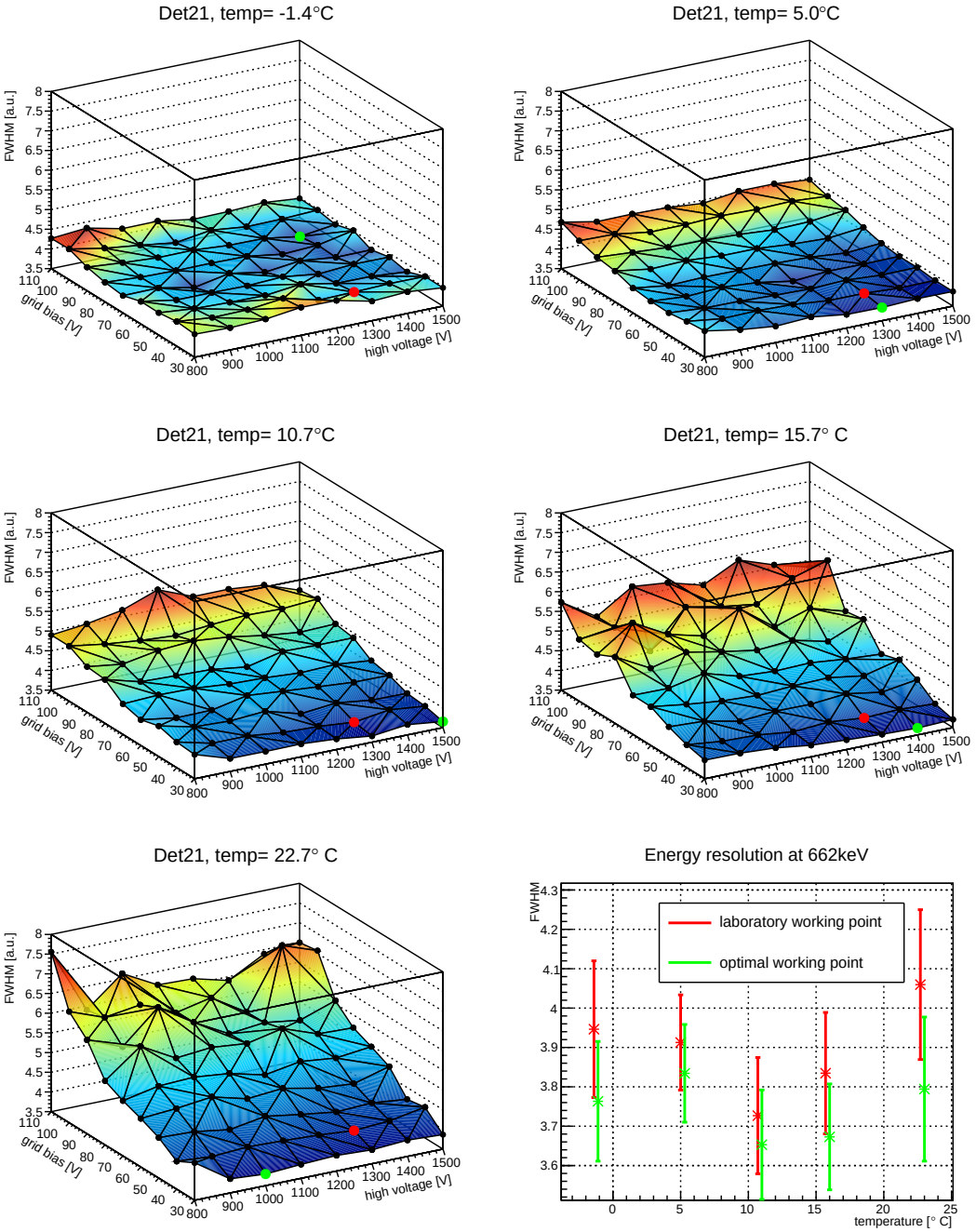

Figure 3.22: Shift of working point of Det21 with changing temperature. Red dot: working point determined at room temperature to be $U_{HV} = 1300\,\mathrm{V}$, $U_{GB} = 30\,\mathrm{V}$ with original evaluation software, green dot: working point determined after reevaluation of data set with improved evaluation software. Data of the plot is based on the reevaluated data from Kresse [Kre17]

with μ as the electron mobility in $cm^2/(V{\cdot}sec)$, L is the drift length (here L =1 cm), HV is high voltage and GB is grid bias, both in Volt. An overlay of all sampled events from the combined energy-/depth-cut is displayed in figure (figure 3.21). Based on the τ_{max} values the mobility of the charge carriers can be calculated. The definition of the mobility-lifetime product is as follows [STY+01]:

$$\mu\tau = \frac{\lambda \cdot L^2}{\mathrm{HV} - \frac{1}{2}\mathrm{GB}} \quad \text{with} \quad \lambda = \frac{1+w}{1-w} \tag{3.5}$$

whereas τ is the lifetime of the electrons in sec and w is the dimensionless weighting factor. The parameter μ is changing according to temperature, τ and λ do as well. In the reevaluated data the w is optimized for each specific working point at each temperature. With the given values for μ and w and the equations 3.4 and 3.5 the temperature dependent charge carrier lifetime for the given setup can be expressed as:

$$\tau(T) = \frac{\lambda(T) \cdot L^2}{HV - \frac{1}{2}\mathrm{GB}} \cdot \frac{1}{\mu(\tau_{max(T)})} = \lambda(T) \cdot \tau_{max(T)}. \tag{3.6}$$

The combination of the measurement of the drift time and the equation 3.6 allows to calculate the temperature dependent mobility-lifetime product for each point in the HV/GB/temperature parameter space (figure 3.23). The analysis reveals a clear depen-

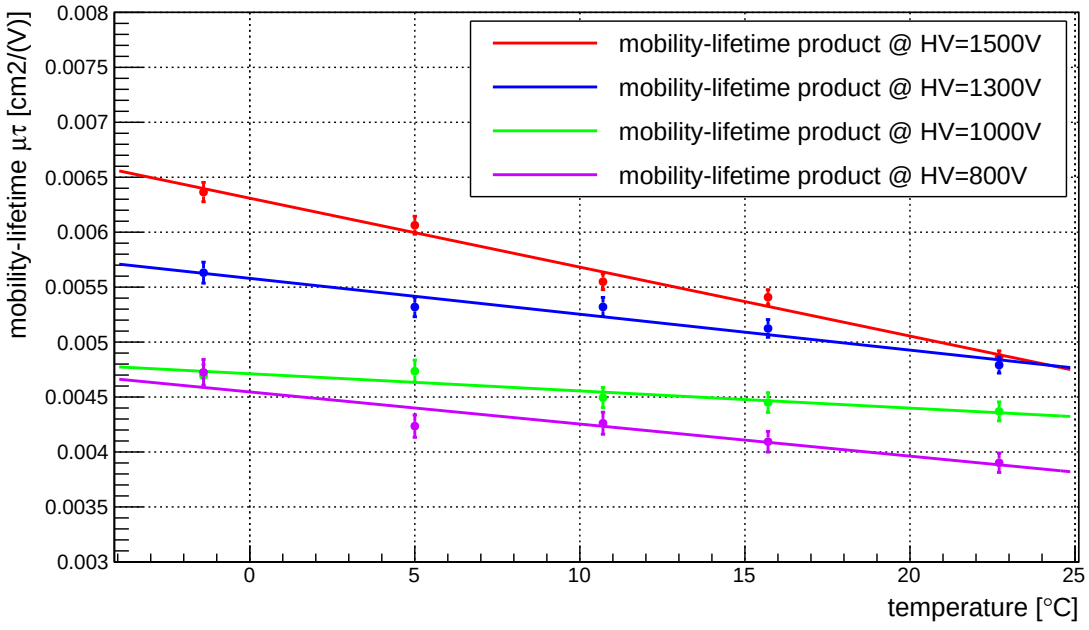

Figure 3.23: Temperature dependency of mobility-lifetime product of Det21 displayed for four different high voltages. Errors are caused by variations of the observed drift time.

dency of the mobility-lifetime product from temperature. For all analyzed high voltages the mobility-lifetime product increases with decreasing temperature. The errors are

caused by the variations of the measured maximum drift times τ_{max}. In comparison to the installed COBRA Demonstrator detectors, Det21 performs at the lower end of the observed mobility-lifetime range of $\mu\tau = (1.13 \pm 0.55) \cdot 10^{-2}$ cm^2/V, [Zat14]. The influence of a reduced temperature to the threshold of the systems is not investigated as the setup differs significantly from the COBRA Demonstrator setup at the LNGS. The reevaluation of the data with the improved software and the automated analysis of the optimal weighting factor for the operated HV/GB combination shows the great potential of the offline pulse shape analysis (figure 3.22). It must be noted, that only one detector (Det21) is analyzed for the full parameter space. Even if the results match the expectations, the results may vary for different detectors as the working points and the performance differ at room temperature, too.

3.4 Spatial resolved Analysis of Charge Transport Properties in CZT

This chapter describes the development and operation of a setup for a spatial resolved mapping of the charge collection efficiency (CCE) for the COBRA Demonstrator detectors and the measurement of the local detector response by use of highly collimated γ-ray radiation. Measurements of Amman and Kargar have shown, that the CCE in CZT varies locally due to inhomogeneities of the bulk material and enhanced trapping at defects in the crystal [ALL02] [KHBM10]. Both have used α-radiation to illuminate the cathode side of the detector, only. As the α-particles are stopped immediately in matter, for this investigation highly collimated γ-radiation is used.
Beside the energy resolution, the charge collection efficiency ϵ is the second major contributor in terms of detector performance. The CCE is a value that describes the loss of the induced charge Q_0 in the detector during its transfer from the point of origin x_0 to the electrodes of the detector, given in length L. The charge loss results in a reduced number of charge carriers detected and causes a shift of the reconstructed energy of the event towards lower energies. Therefore, detectors with large, inhomogeneous zones show deteriorated energy resolution. The CCE is defined as follows:

$$\epsilon = \frac{Q_{det}}{Q_0} = \frac{\sum_{i=x_0}^{L} \Delta Q_i \Big|_e + \sum_{j=x_0}^{L} \Delta Q_j \Big|_h}{Q_0} \quad \text{with} \tag{3.7}$$

$$\Delta Q_{i,j} = Q_0 \cdot \varphi(x_{i,j}) \cdot e^{\left(\frac{-\Delta x_{i,j}}{\mu_{e/h}\tau_{e/h}E(x_{i,j})}\right)}. \tag{3.8}$$

In equation 3.8 the $\Delta Q_{i,j}$ is the exponential decline of the charge cloud during the transfer. As the shape of the weighting potential $\varphi(x_{i,j})$ is the same for all COBRA Demonstrator detectors, this decrease depends on the point of interaction of the particle in the detector and the mobility lifetime product $\mu\tau_{(e/h)}$ of the specific detector along the path of charge transport. Minor variations due to different working points of the

detectors are neglected. The carrier mobility $\mu_{e/h}$ is basically a material property that in CZT can only be adjusted by changing the zinc concentration, whereas the carrier lifetime $\tau_{e/h}$ is mainly dependent on the charge trap density of the material (section 2.2.2). Effectively, the weighting factor w accounts for the integral CCE properties of the detector (equation 2.17).
As the supplied detectors for the COBRA Demonstrator setup are from different batches and of different quality grades, ranging from detector- to spectrometer-grade material with energy resolution varying between 2%...5% at 662 keV, the performance of each detector has to be examined before the installation. One part of this examination is the determination of the working point and the weighting factor as described in section 3.2. The second part is the mapping of the CCE from at least two sides. The mapping of the localized CCE allows to select detectors with respect to their specific properties. The advantage of the selective mapping over the integral total efficiency measurement is, that the mapping reveals strongly affected areas in the detector, that are not visible with flush measurements. A detector with a homogeneous CCE map must be preferred to a detector with the same total efficiency but inhomogeneous CCE map, as interactions in the distorted regions are affected by worse energy resolution and a shifted energy calibration. If an interaction happens in such areas, the integral determined weighting factor w is too high and the reconstructed energy is too low. The result is a shift of the event out of the acceptance window for $0\nu\beta\beta$-search. Therefore, the detectors with the best performance in terms of energy resolution and a homogeneous spatial CCE are selected and are placed at the inner eight positions of the 64 detector array. Since all detectors are of the same geometry and grid layout, the performance is strictly related to the quality of the material.

3.4.1 Experimental Setup for Localized Irradiation

To gain information about the spatial distribution of the CCE a scanning device and a highly collimated γ-ray source for localized irradiation of the detectors is needed. For this purpose a dedicated collimator device is developed. The main requirements are a resulting spot size of the γ-beam at the detector of less than 1 mm diameter and an attenuation factor offside of the channel of more than 100 for the use of a ^{137}Cs source (figure 3.24). To reduce the data taking time at the detector, a highly radioactive source must be used. Additionally, the radioactive source can be exchanged optionally and the radiation protection of the operator must be guaranteed. Consequently, the collimator is made from lead and consists of two parts that are bolted together. The design allows to use industrial LLA-type sources, that are available in different activities and with different nuclides. The channel of the lead collimator has a length of 6 cm and a diameter of 0.5 mm. For the following described experiments a 100 MBq ^{137}Cs is used. The activity is a trade-off between needed measuring time and count rate at the detector that the DAQ system can handle.
The test rig itself is designed to allow for an irradiation of the detector from all three directions in a well controlled way (figure 3.25). By turning the detector mount $\pm 90°$ and by moving the x-y-stage from vertical to horizontal, in total four sides of the

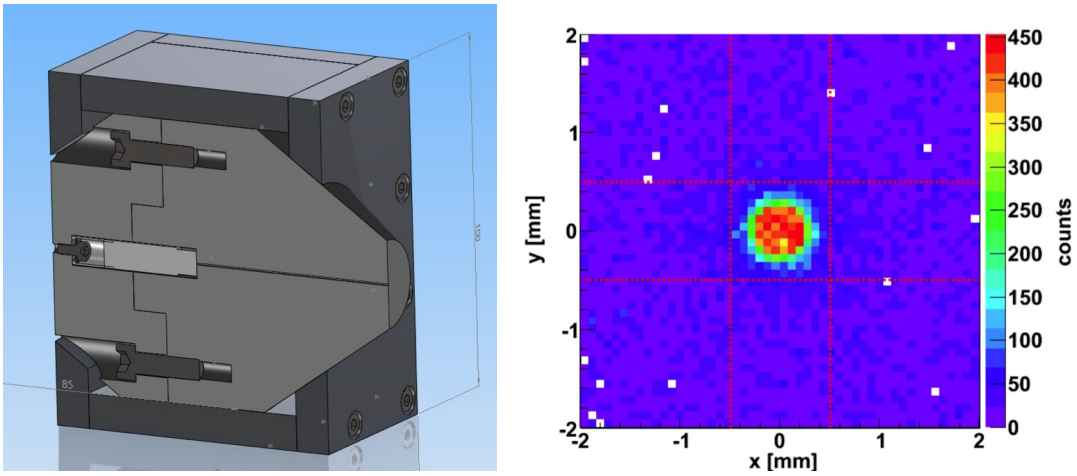

Figure 3.24: Left: Schematic drawing of the collimator device. The channel of the collimator has a length of 6 cm and a width of 0.5 mm. Right: Beam intensity profile of ^{137}Cs source at 3 mm distance from the detector surface. Only photons with energies in the energy range of the 662 keV FEP are regarded [Wes12].

detector are directly accessible without changing the detector connections (figure 3.26). To access the last sidewall of the detector, it must be tilted on the detector mount. Only the cathode side is not accessible, but the irradiation through the anodes in combination with the reconstruction of the depth of interaction provides the same information.

In the test rig the collimator device is mounted on two linear drives that are computer controlled. The x-y-movement of the collimator is performed by stepper motors with µm precision. By combined use of localized irradiation through the anodes and pulse shape analysis for depth reconstruction it is possible to reconstruct the CCE of the detectors in small volume elements. The main drawback of the sidewall irradiation (x-z-plane) is, that a possible inhomogeneous CCE distribution in the x-y-plane can not be resolved, since it is not possible to locate the point of interaction in the x-y-plane of a CPG detector. For the 2d mappings of the nominal $(10\times10)\,\mathrm{mm}^2$ sidewalls of the detectors a 12×12 raster of reading points with 1 mm steps and 600 sec acquisition time is chosen. The larger raster is necessary as some detectors are slightly larger than the nominal value. In this configuration a total mapping time of $t \sim 24\,\mathrm{h}$ per side is needed, allowing to run daily scans. For this investigation the detectors are operated at their prior determined, specific working point. All detectors, currently installed at LNGS in the COBRA Demonstrator setup, are scanned from two sides - through the anodes and from one sidewall. This allows for a three-dimensional back-projection of the CCE-distribution. This is sufficient, as already the scan through the anodes in combination with depth sensing reveals the most important information of relative CCE distribution. Nevertheless, the ability to access four sides of the detectors is used for intense analysis.

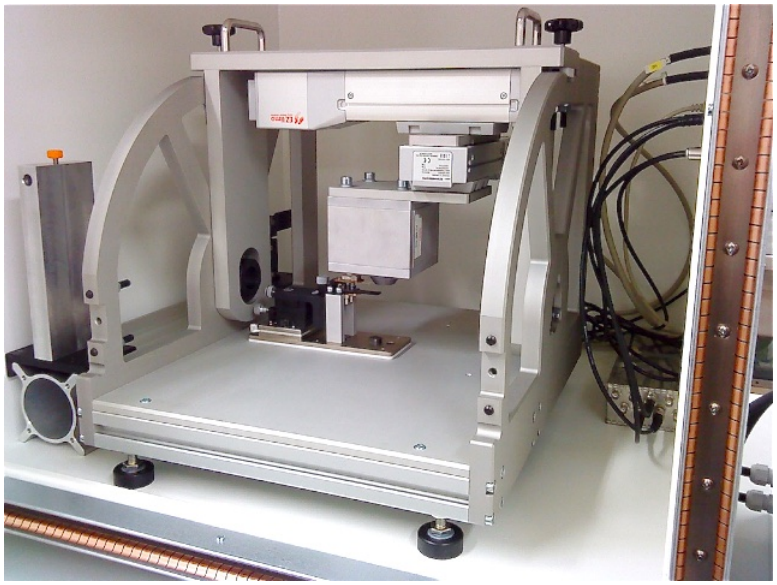

Figure 3.25: Testrig for two dimensional spatial resolved measurement of the CCE of the COBRA Demonstrator detectors. The collimator is moved with µm precision by stepper motors. In this position the detector is irradiated from the anode side. The axes are computer controlled and can be scripted for unattended operation. The test rig is installed and operated in a electromagnetic shielded box.

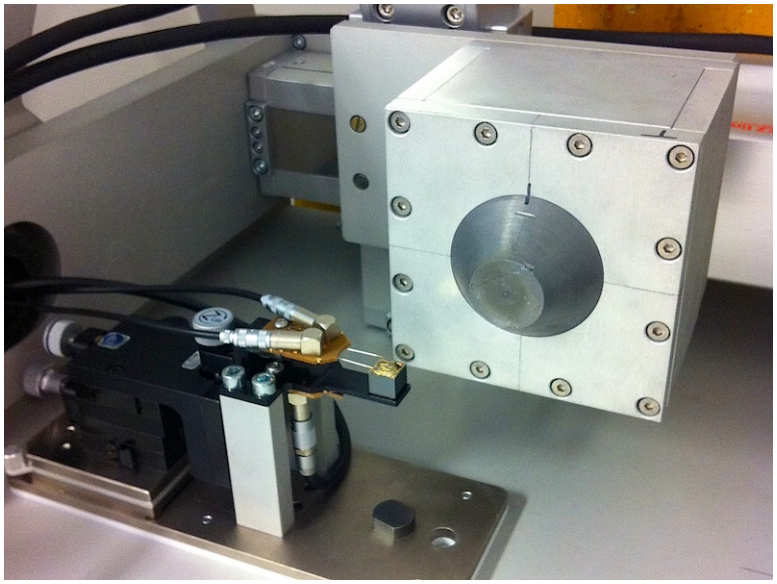

Figure 3.26: The whole collimator assembly can be moved downwards to irradiate the detector from the sidewall. The detector mounting can be rotated, such, that three of the sidewalls can be irradiated with no additional manipulation needed. Here, the detector is installed and connected.

3.4.2 2D-Mapping of the Charge Collection Efficiency

For the evaluation of the acquired spectra and the graphical representation of the CCE only the full energy peak entries of the ^{137}Cs are regarded. Due to the high activity of the ^{137}Cs source a large number of forward scattered photons lower than $E = 662\,\mathrm{keV}$ are found in the Compton valley between the full energy peak and the Compton edge at $E = 478\,\mathrm{keV}$ if compared to measurements for working point determination. To account for this enhanced background in the Compton valley the fit function for the FEP consist of a linear combination of a conventional Gauss-function and a Fermi-function:

$$F(x) = \frac{A}{\sigma_g\sqrt{2\pi}} \exp\left(-\frac{(x-\mu_g)^2}{2\sigma_g^2}\right) + \frac{B}{\exp\left(\frac{x-\mu_f}{S}\right)+1} \quad . \tag{3.9}$$

The variables are:

- A – area below Gauss function
- σ_g – standard deviation of Gauss function
- μ_g – centroid of Gauss function
- B – amplitude of of Fermi function
- μ_f – centroid of Fermi function
- S – decline of Fermi function

Based on this combined fit, the peak position and the peak area of the full energy peak (FEP) can be evaluated and is used for the following analysis (figure 3.27).

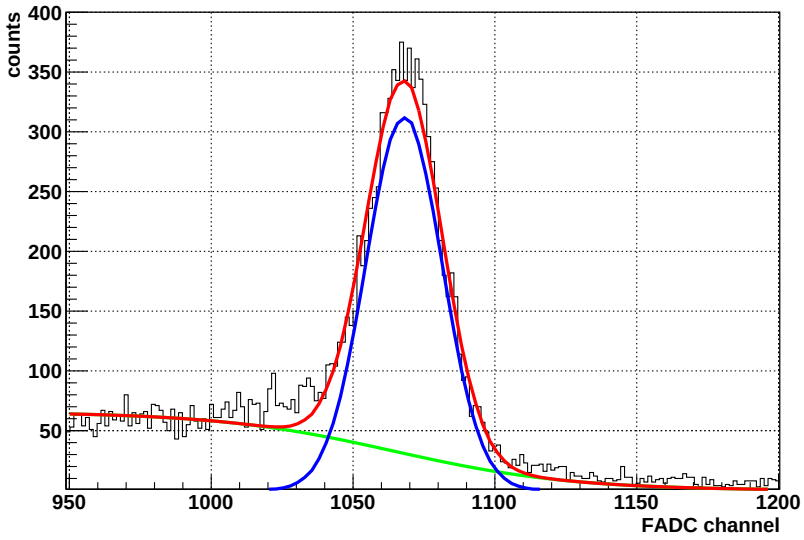

Figure 3.27: Overlay of the two parts of the full energy fit function used for efficiency analysis. Black: histogram of measured events, green: Fermi–function, blue: Gauss–function, red: combined fit–function to be used for analysis.

In the first analysis, the two dimensional localized detection efficiency for the ^{137}Cs full energy peak is evaluated. As the CPG principle does not allow to resolve the point of interaction in the x-y-plane, a two dimensional mapping from a detector side results in a two dimensional projection of a three dimensional distribution of the CCE properties in this horizontal oriented volume element in the detector. To analyze the projected CCE the total acquired spectra is normalized to 'one' and the entries in the full-energy-peak are evaluated. The heat map of the normalized FEP shows the expected intensity distribution with an almost flat center that slowly decreases towards the edges of the detector (figure 3.28).

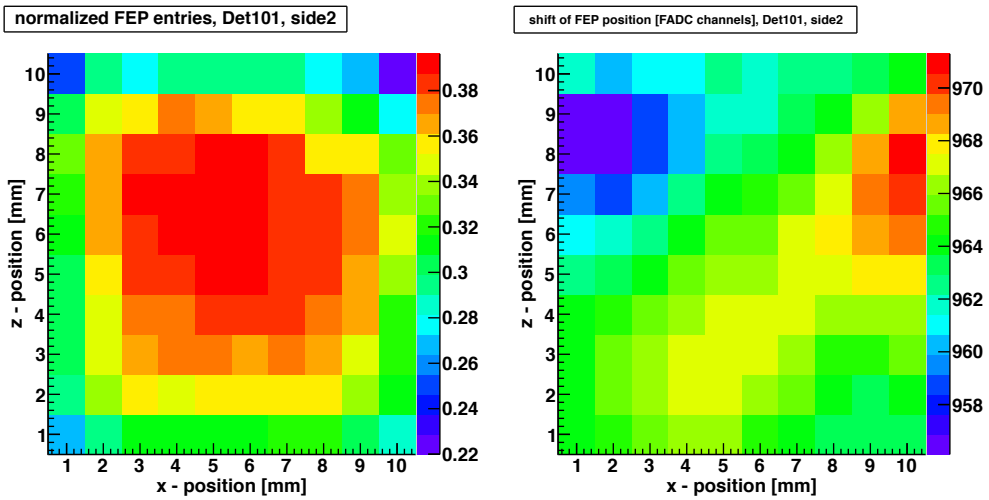

Figure 3.28: Left: full-energy heat-map of side2 from detector Det101. The intensity of the full-energy peak is normalized to the full spectrum. Right: heat-map of full-energy peak centroid shift of the same measurement. Green: mean centroid of the full detector, cooler colors indicate charge loss, hotter colors indicate better CCE than average.

In this type of illustration the anodes are always on top, the cathode is at bottom. On righthand side of figure 3.28 the shift of the centroid of the full-energy peak from the mean of the peak position is displayed. The decay of the intensity of the normalized full-energy entries to the edges of the detector is caused by Compton scattering of photons out of the detector. Those events do not contribute to the full-energy peak and result in total efficiency loss. The very symmetrical appearance indicates a well aligned setup. An average radius of approximately 2 mm for Compton scattered photons to interact a second time and to finally deposit their rest energy can be deduced from the short range of the decay. Areas with better CCE are qualified by less charge loss, hence, the centroid values of the full-energy peak is shifted to higher values relative to the mean centroid value of the detector, the opposite is true for affected areas.
In figure 3.29 the full-energy peak position of scan-position (x=2, z=9), (x=10, z=8) and the full-energy peak position of the detector-mean of figure 3.28 (right side) are compared. The peak positions of the violet histogram are shifted to lower energies

compared to detector mean (green histogram) whereas the red is shifted to higher energies. All detectors mounted in COBRA Demonstrator at LNGS are scanned at

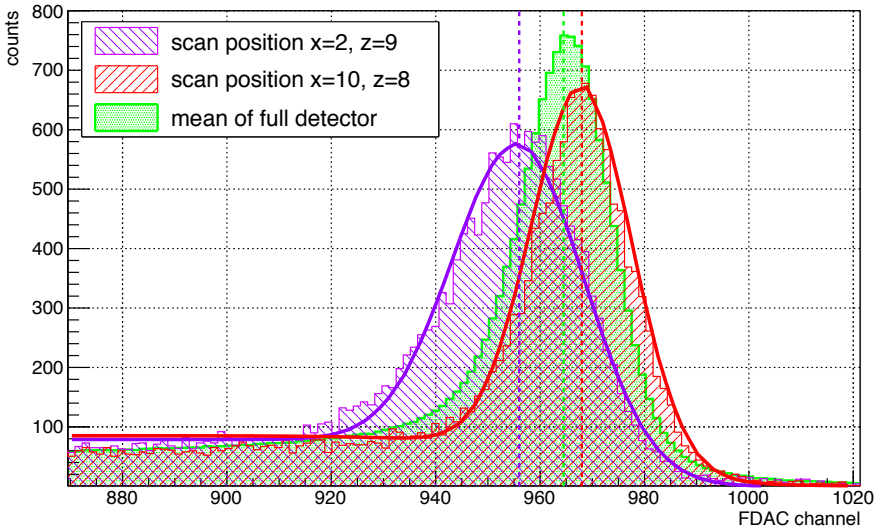

Figure 3.29: Analysis of the full-energy peak shift of the point of lowest CCE (x=2, z=9, violet histogram and fit) and highest CCE (x=10, z=8, red histogram and fit) of the CCE mapping in figure 3.28 right hand side. The detector mean is plotted in green.

least from two sides: through the anodes and through side1 (figure 3.30). The mapping of four sides of the detector and the projection to a cube frame allow to receive an impression of the three dimensional distribution of the zones with different CCE in the detector (figure 3.31 and figure 3.32). The evaluation of the scans through the anodes in combination with the z-information of the interactions reveals the three dimensional distribution of possibly affected areas in the detectors.

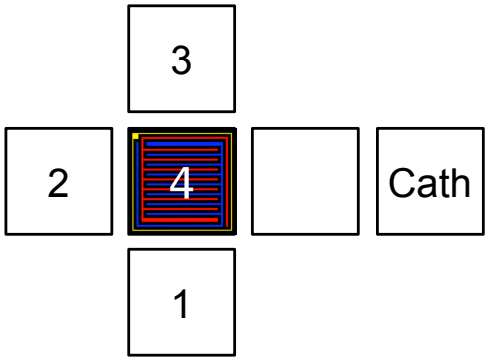

Figure 3.30: Declaration of detector sides with respect to guard ring contact pad - the yellow box upper side left at side four. The four numbered sides are directly accessible with the 2D scan test rig. The unlabeled side is accessible by turning the detector at the support frame. It is not possible to directly irradiate the cathode.

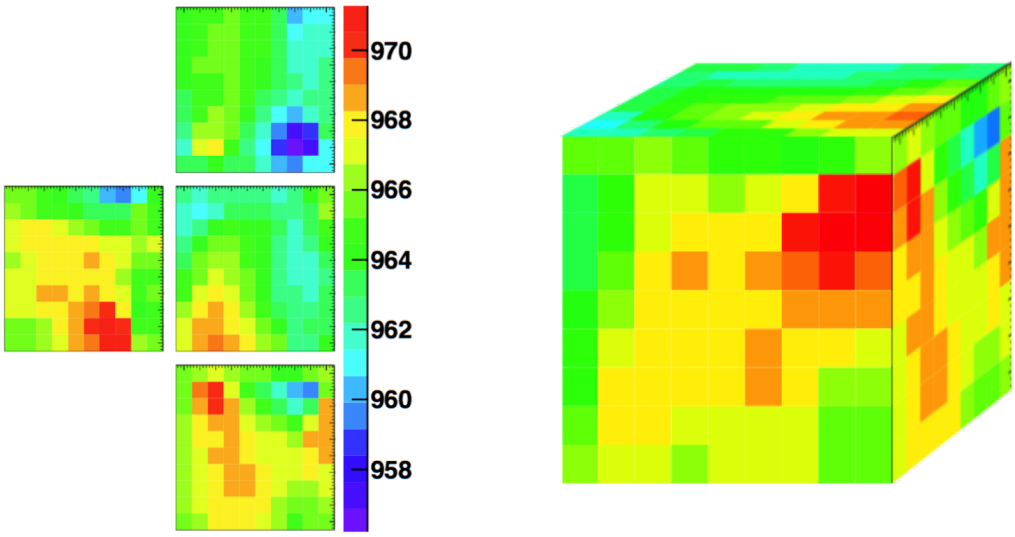

Figure 3.31: Projection of the CCE mappings of the four measurable sides of the detector (here Det09) to a detector cube (center is anode side). The areas with better than average CCE form a continuous volume element if viewed from three sides. Even the worse performing area on the hidden side of the cube is visible from the right side. Color coded values are FADC channels and indicate the shift of the full energy centroid.

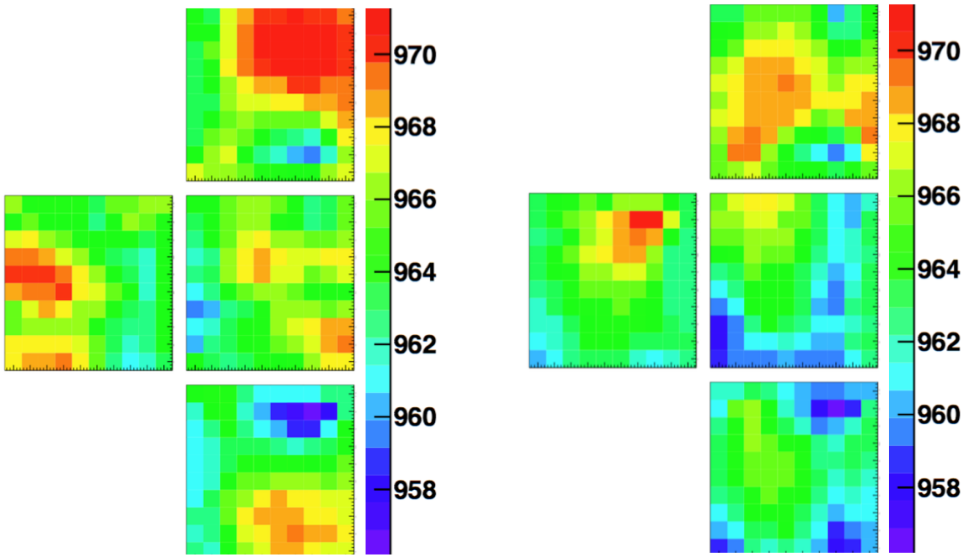

Figure 3.32: CCE mappings of detector Det11 (left) and Det15 (right), centered square is the view to the anode. Color coded values are FADC channels and indicate the shift of the full energy centroid.

3.5 Compton Coincidence Experiment

The chance for a full energy deposition of high energetic photons with $E_\gamma > 1.1\,\text{MeV}$ in a $1\,\text{cm}^3$ detector is relatively small, more often Compton scattering or pair production with secondary interactions of annihilation photons will happen. As the COBRA experiment moves towards bigger detectors for the large scale setup, the chance for a second interaction of the scattered photon in the same detector increases. The second interaction in the detector will appear as MSE, whereas the searched $\beta\beta$-decay is primary SSE. Hence, an effective differentiation of SSE versus MSE is needed.

3.5.1 Theory and Experimental Setup

To generate a library of defined and verified single site events in different depth of a CZT detector, a test setup is built (schematic figure 3.33). In the experimental setup, a turnable mounted, collimated γ-source, that can be equipped with either ^{137}Cs- or ^{60}Co-sources, is installed and points at a CZT scatter detector in the pivot of the setup. A HPGe detector is used to detect the scattered photons (figure 3.34).

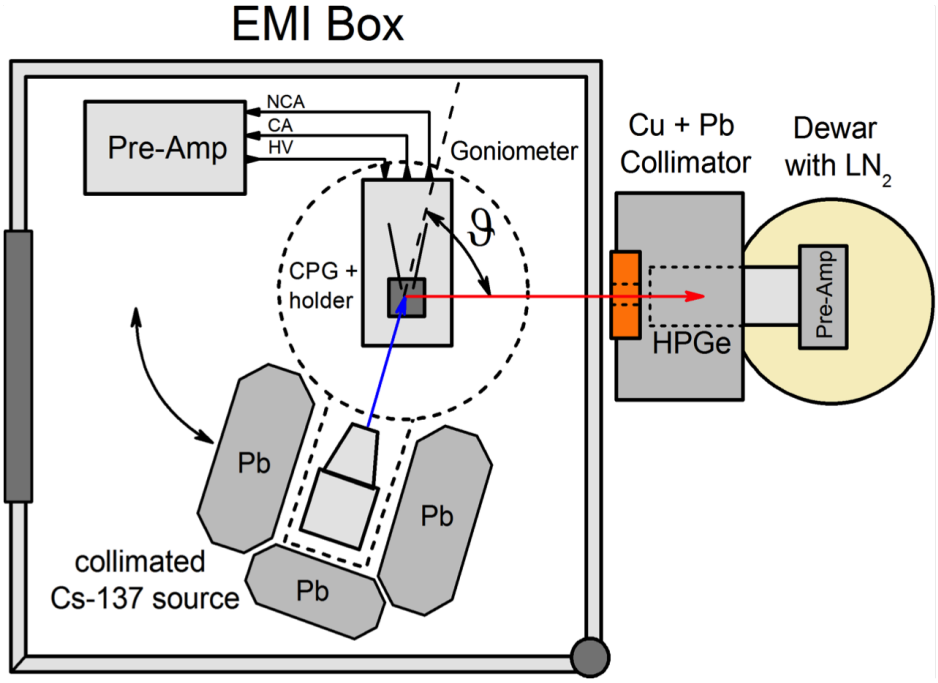

Figure 3.33: Schematics of the Compton Coincidence experimental setup (top view). The pre-collimated γ-source is mounted on a move- and rotatable goniometer device, the CZT-scatter-detector is located at the pivot of the setup. The HPGe detector to measure the scattered photon is placed outside of the EMI-box in a lead castle [Zat14].

It is installed outside of the electromagnetic interference shielding box (EMI-box) in a lead castle, at a fixed position. The lead castle is needed to shield the HPGe detector

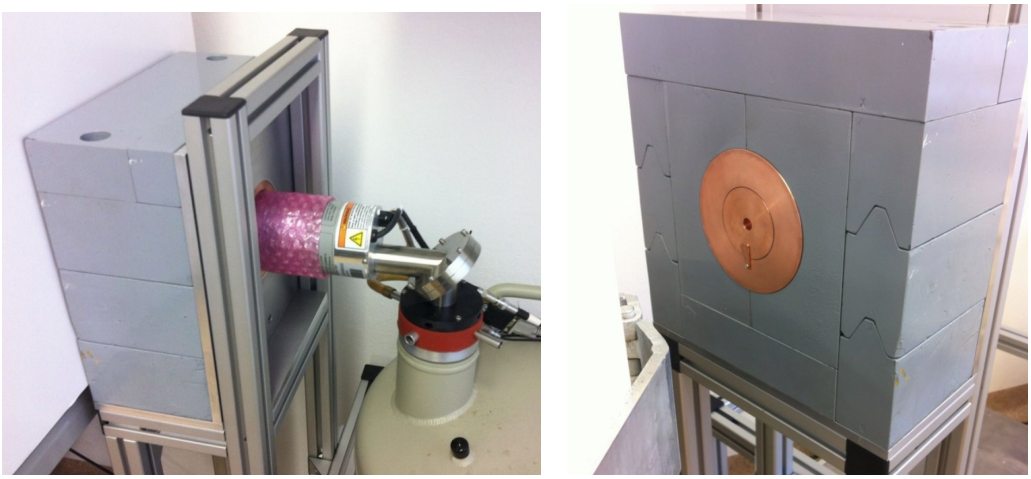

Figure 3.34: Lead collimator setup for HPGe detector of Compton scatter experiments. Beside the 5 cm lead shielding, the detector is screened by a 1 cm thick copper shroud. The frontside of the shroud can be narrowed by 2 cm thick copper plugs. Here, the copper plug with the 1 cm drill hole is installed.

from unwanted direct radiation from the pre-collimated γ-source (figure 3.34). The geometrical acceptance angle for the scattered photons can artificially be narrowed by 2 cm thick copper plugs with different drill hole diameters installed in front of the HPGe detector. This is necessary as the diameter of the HPGe is about 5 cm, which widens the acceptance angle too much and smears out the accepted energy window. The lead castle of the HPGe-detector also shields the background contribution of the laboratory environment. A total reduction factor of about 5 over the full energy range is reported (figure 3.35).
To select a specific energy of the scattered photon the scattering angle ϑ between the CZT- and the HPGe-detector can be adjusted. The energy of the scattered photon is calculated by the Klein-Nishina-Formula:

$$E'_\nu(\vartheta) = \frac{E_\nu}{1 + \frac{E_\nu}{m_e}(1 - \cos\vartheta)} \tag{3.10}$$

A Compton scattered photon is by definition a single site event. If the scattered photon is detected in the HPGe detector and the following two main requirements are fulfilled, the chance that the first interaction is SSE is very high. The first requirement is, that both detectors are triggering basically at the same time and the sum energy of both detectors is identical with the primary energy of the emitted photon. Secondly, the scatter-angle dependent energy deposition in the CZT and in the HPGe have to be correct. If both requirements are fulfilled, the detected photon can be tagged as a singly Compton scattered photon in the CZT-detector that finally undergoes a full energy deposition in the HPGe-detector. With the adjustable scattering angle of the setup, the energy dependent characteristics of SSEs in the CZT detector can be probed.

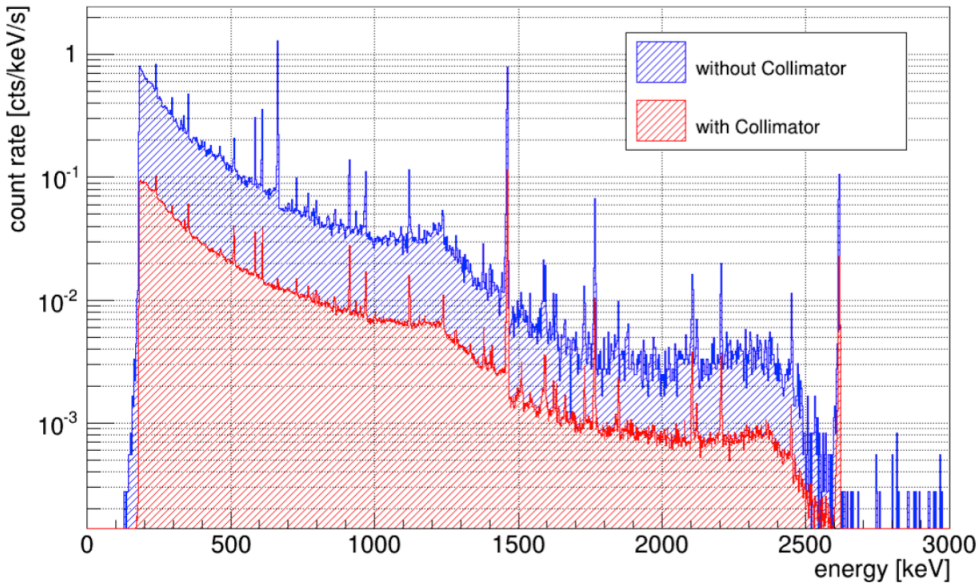

Figure 3.35: Reduction of the background due to installation of the lead castle. The difference of the intensity at the 662 keV line is due to the presence of a ^{137}Cs source in a second setup during background measurement [Zat14].

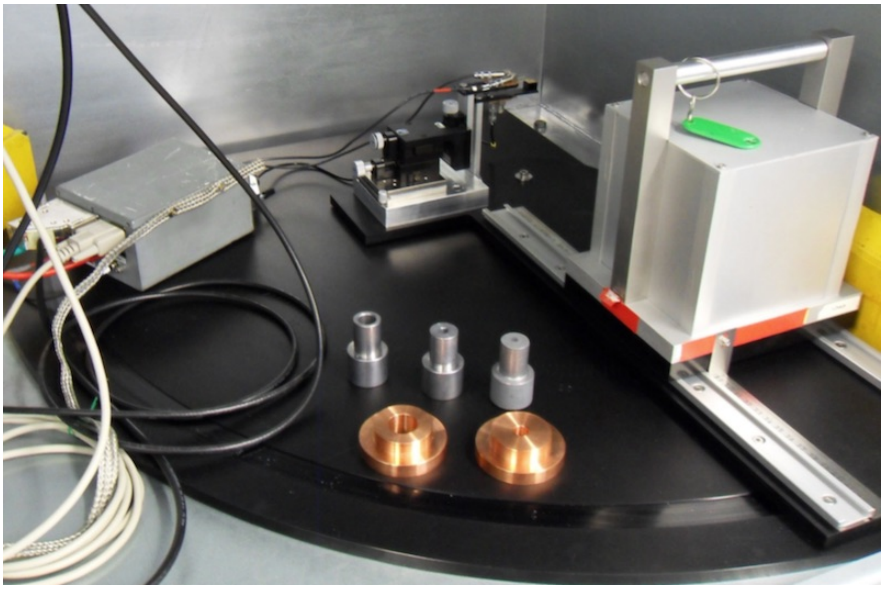

Figure 3.36: Goniometer setup of Compton Scatter setup inside the EMI box. The CZT-detector is mounted in the pivot of the setup. The γ-source is placed in the grey box on the right side. The distance between the γ-source and the CZT scatter detector can be adjusted to compensate for different source intensities. The lead plugs are used to limit the emission angle of the γ-source, the copper plugs are used to limit the acceptance angle of the HPGe detector.

3.5.2 180° Back-Scattering of ^{60}Co photons

The initial experiment is performed with a ^{60}Co-source placed right between CZT- and HPGe-detector. In such a configuration the 180° back-scattered photon from the CZT is detected in the HPGe and generates a well-defined SSE at a specific energy in the CZT. As this process also happens the other way around - the Compton back-scattering in the HPGe and detection of scattered photon in the CPG - such setup can be used for the same analysis of the HPGe detector. A modified setup is developed at TU Dresden to scan HPGe detectors for depth dependent variations of pulse shapes in HPGe detectors.
^{60}Co emits two high energetic photons with nearly the same relative emission intensities. The energy of the 180° back-scattered photon from the CZT is calculated by formula 3.10. The resulting energies can be found in table 3.6. As two high energetic photons are emitted at energies of $E_{\nu 1}$=1173 keV and $E_{\nu 2}$=1332 keV, both interactions can be used for SSE analysis. In figure 3.37 the CZT events in the $E'_{\nu 1/2} \pm 20$ keV range are plotted in solid green for $E'_{\nu 1}$ and solid blue for$E'_{\nu 2}$. The corresponding 180°-

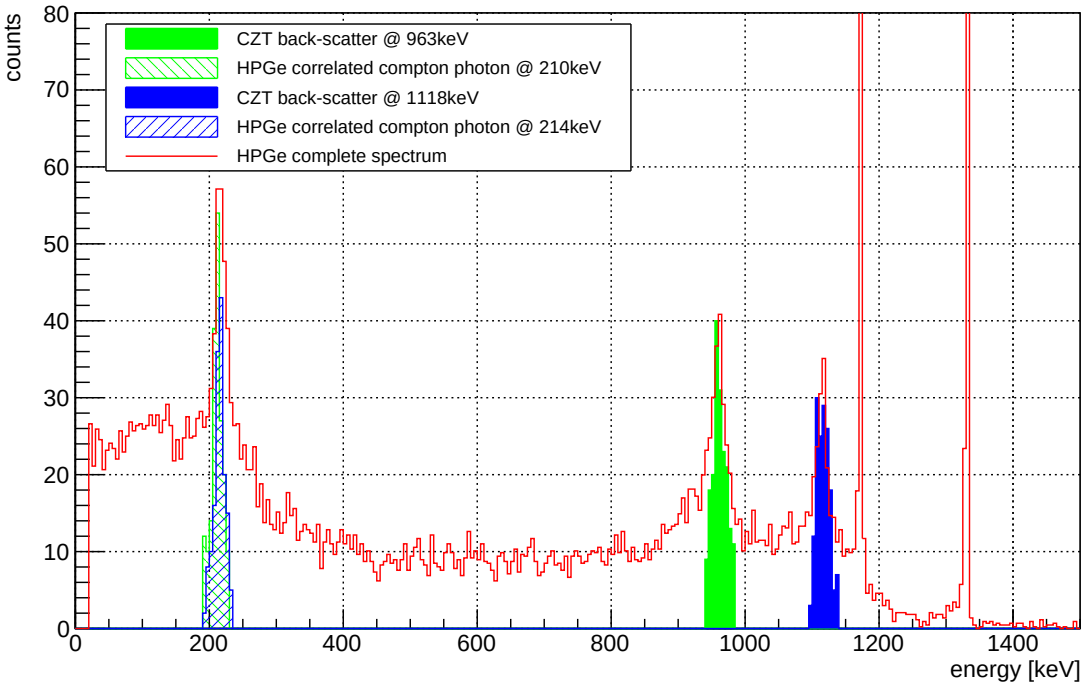

Figure 3.37: Compton scatter setup with a move- and rotatable, pre-collimated γ-source, CZT-scatter-detector and shielded HPGe detector to measure the scattered photon.

back-scattered photons, detected in the HPGe, are plotted at 210±20 keV in dashed green and 214±20 keV in blue. Additionally, in red the complete, down-scaled HPGe-spectrum is superimposed. The intense peaks at $E_{\nu 1}$ and $E_{\nu 2}$ of the ^{60}Co full energy

deposition in the HPGe are off scale. The above described back-scatter-process of the primary photons in the HPGe is visible at $E'_{\nu 1}$ and $E'_{\nu 2}$, too. This effect can only happen in a configuration, where the ^{60}Co-source is placed in-between the two detectors. With this data set a first investigation for the efficiency of the MSE cut is performed. The result shows, that about 3% of the supposed single site events still are MSE like. Independently from the cut strength used, this number is almost stable. This gives strong indication, that these events have to be attributed to random coincidences. To reduce the impact of random coincidences in the later, angular scatter experiment, a special lead castle for the HPGe detector is built (section 3.5.1).

Table 3.6: Resulting energies for 180° back-scattered photons from ^{60}Co

	E / (keV)	E'_ν / (keV)	E''_ν / (keV)
$E_{\nu 1}(4^+ \rightarrow 2^+)$	1173.24	963.43	209.81
$E_{\nu 2}(2^+ \rightarrow 0)$	1332.50	1118.11	214.39

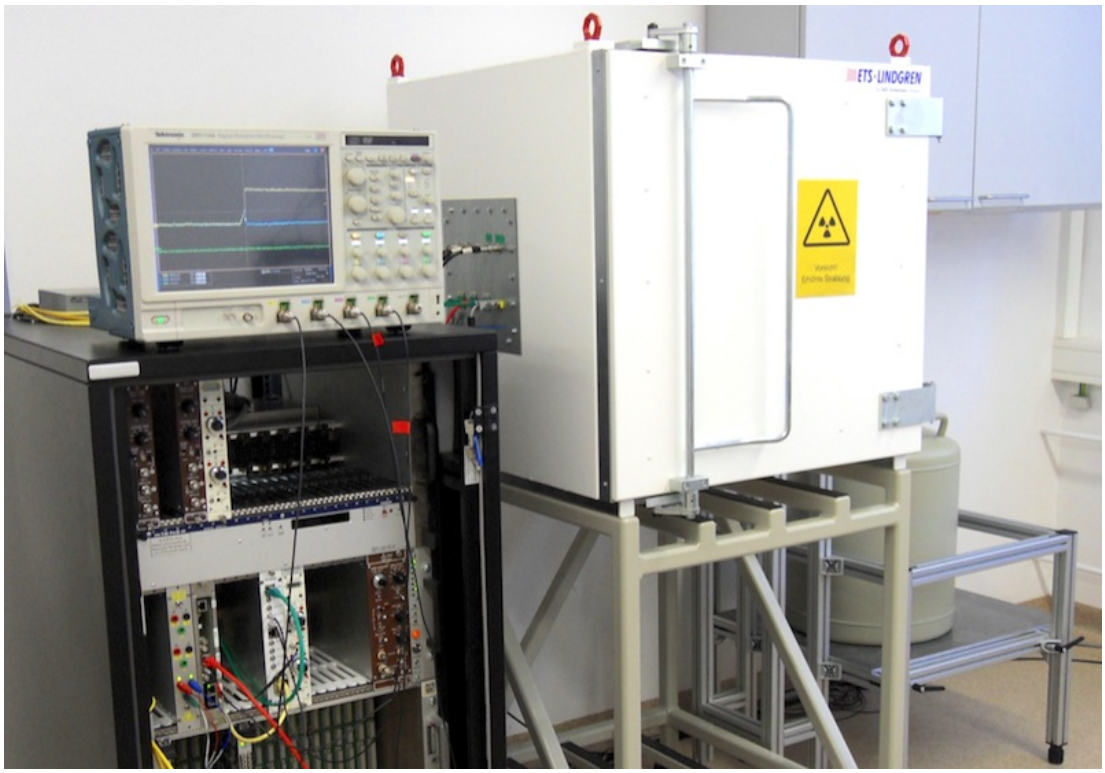

Figure 3.38: Electronics, electromagnetic shielding box and dewar of HPGe detector (partially covered by EMI box) of Compton Scatter test setup.

3.5.3 Angular Compton Scatter Experiments

In the continuation of the experiment, different scattering angles are used to deposit different energies in the detectors. Following, the resulting spectra are analyzed for the generation of single site events in the CZT detector. Figure 3.39 displays the resulting CZT and HPGe coincidence spectra for six different scattering angles. According to Klein-Nishina, the measured intensity at the CZT detector is decreasing for higher energies.

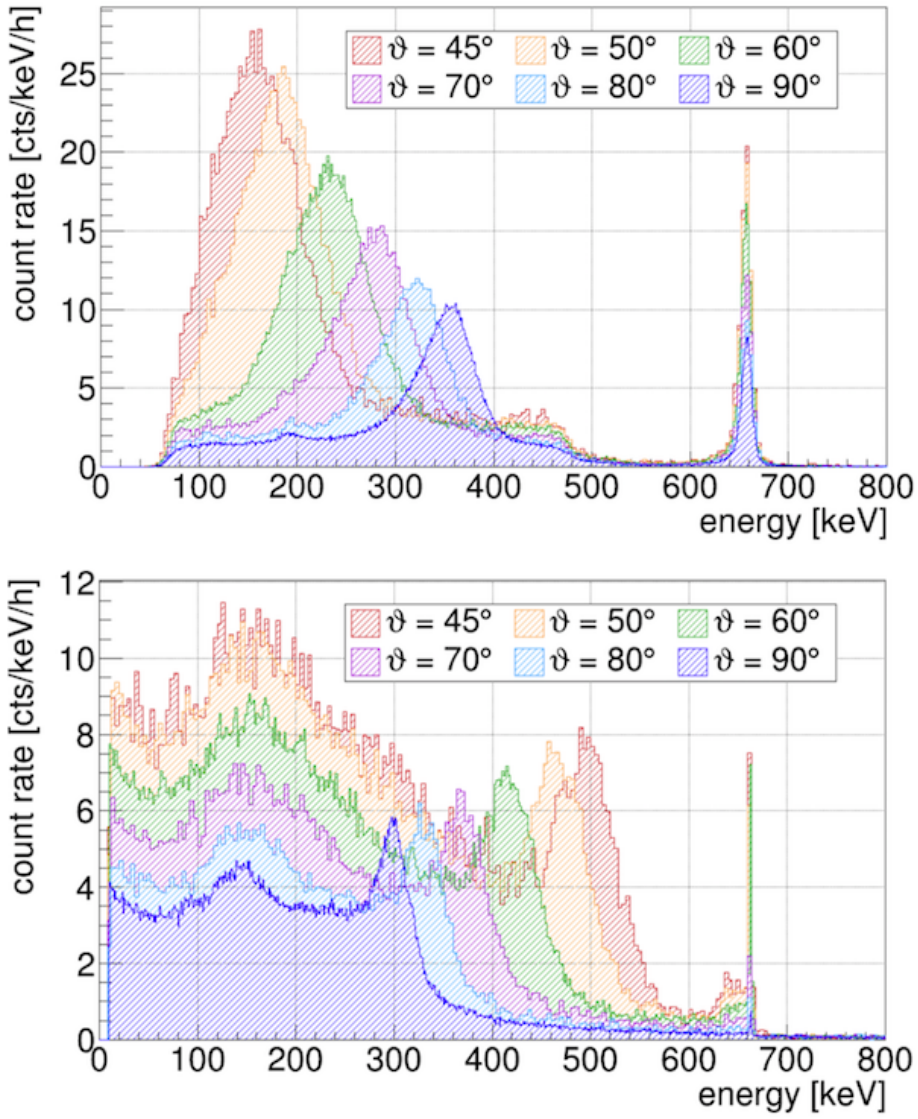

Figure 3.39: Above: Coincidence spectra of the CZT detector for six different scatter angles of ^{137}Cs. Width of the scatter peak is a function of acceptance angle at the HPGe detector. Measurements are performed without limiting collimator plug. Below: Corresponding HPGe spectra for the six different scatter angles. [Zat14]

The combination of the SSE event selection with the depth selection cut and the coincident energy measurement at the HPGe-detector allows to build up a a single site interaction library for different depth of interactions and different energies in the detector. All events in such a selection are defined single site interactions that originate from the same depth plane. Hence, the overlay of the raw samples of this specific selection should result in a narrow band of uniform pulses. As expected, there are no significant deviations from the average pulse shape visible (figure 3.40). With this analysis the proof of concept of this approach is shown. Based on this method a library of SSE pulse shapes for specific depths and energies is created by Zatschler.

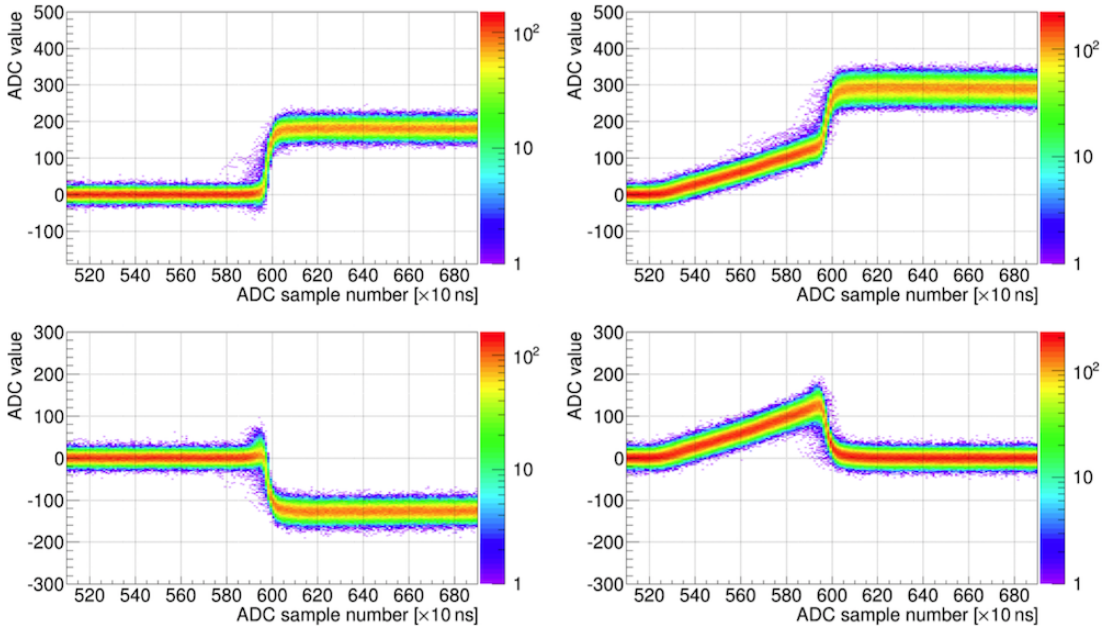

Figure 3.40: Overlay of raw signals from two different depth regions, left: anode near region, right: cathode near region, above: CA signal, below: NCA signal. The pulses representing the SSEs in the CZT selected by coincidence analysis with the HPGe detector.

3.6 Investigations on a possible α/β-Discrimination at the Cathode

A reliable α-particle induced event identification is crucial to reduce this background contribution in the COBRA-Experiment. Currently, the main background contribution originates from α-active contaminations at the detector surface. This implies all sides of the detector: the anode side, the cathode side and the lateral side walls, too. From now on the side walls are also referred to as lateral surfaces. Even though the lateral surfaces are completely covered with a protective lacquer and the anodes are partially covered, there is still a background contribution from these sides of the detector. The organic encapsulation seals the susceptible surface of the detector from humidity, mechanical strain and - as a side effect - acts as a stopping layer for α-particles from the surface of the detector. Hence, the plain cathode is the only remaining part of the detector which is unprotected and completely exposed to the lab environment. In this section the identification of α-induced events on the cathode and its possible discrimination from β-induced events is discussed. The effects at the anode side are described in chapter 2.2.3.

3.6.1 The Origin of ^{190}Pt and ^{210}Po at the Cathode

The analysis of the LNGS background spectra reveals two significant α-contributions from the cathode side of the detector. The root causes are identified to be ^{190}Pt ($Q_{^{190}\mathrm{Pt}}$=3.249 MeV) and ^{210}Po ($Q_{^{210}\mathrm{Po}}$=3.792 MeV, [FBC96]). In principle, the α-decays from those isotopes can energetically mimic $\beta\beta$-events as the detected energy strongly depends on the emission angle towards the detector and the self absorption in the cathode. Furthermore, such an α-event is always a Single-Site-Event and, hence, not distinguishable from $\beta(\beta)$-decay. Therefore it is advised to probe for a possibility to differentiate α- and β-decays that occur in the vicinity or at the surface of the cathode. The cathode of the detector covers the whole bottom of the crystal (figure 3.1). It is made of two components: platinum and gold. The materials are layered in two thin films with the platinum in direct contact to the CZT. The total thickness of the cathode is 80...100 nm as per supplier information. However, XRD measurements show, that the cathode of the analyzed detector is only about half of the nominal thickness (section 3.1), but it is known, that the thickness of the electro-chemical plated layer is batch dependent. For the following experiment thickness variations in the 10 nm range are negligible as the range of α-particles in the MeV-range is limited to a few µm in CZT while those of β-particles of the same energy can reach up to several hundred µm. Due to the strong interaction of the heavy, charged α-particle with the detector and the high stopping power of CZT, the α-particle loses its energy on a comparable short track. A perpendicular started α-particle with the full energy of the ^{190}Pt-decay has a maximum range of roughly 1.2 µm in CZT and, hence, deposits its energy in the ultimate vicinity of the cathode (figure 3.41).
Natural abundant platinum contains traces of the premordial isotope ^{190}Pt. Its abundance is given with 0.01%, the half-life is $T_{1/2} = (4.97 \pm 0.16) \times 10^{11}$ yr and the Q-value

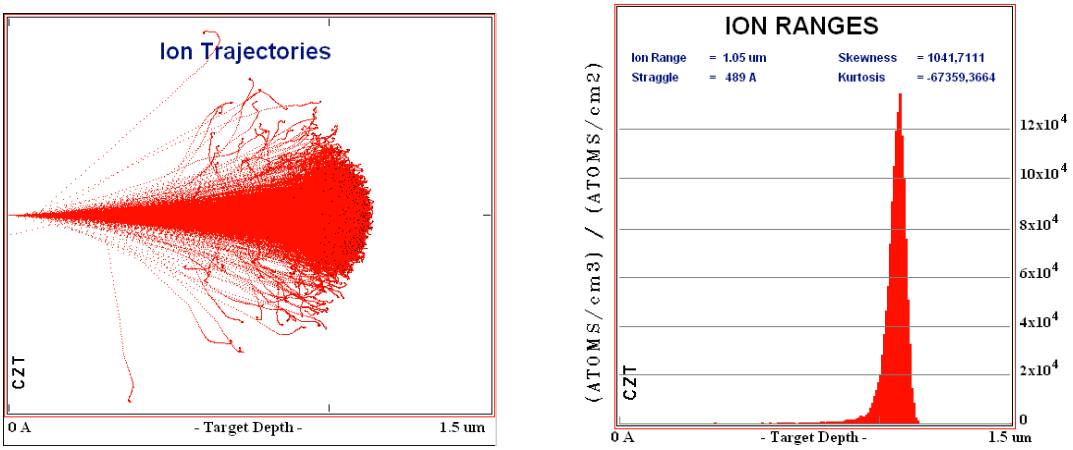

Figure 3.41: Ion Trajectories and Ion Ranges of perpendicular started 3.2 MeV alphas into CZT; Simulation based on SRIM

of the α-decay is $Q_\alpha = (3.252 \pm 0.006)$ MeV [BGS+17]. Even with its long half-life and the low total number of ^{190}Pt atoms at the cathode ($N \simeq 6.6 \times 10^{13}$ atoms assuming 1 cm^2 and 100 nm thickness) it is still possible to detect the alphas from the ^{190}Pt-decay at both electrodes of the detector, at the anodes and the cathode. Based on the given values for layer thickness, density and half-life, a ^{190}Pt-decay rate of about 100 events per year and detector can be deduced. The detected rate is scaling linear with the real thickness of the platinum-layer. Due to the randomly oriented emission of the alphas, only about half of the events are detected, as the other half is emitted outside of the cathode/anodes and the detector. If the alphas are emitted towards the detector, the detection efficiency is basically 100%, as α-particles are dense ionizing particles. Taking into account the short range, the almost full energy deposition of α-particles starting at the cathode, the emission towards the crystal and the expected number of decays per detector and year, a expected number of ^{190}Pt-events can be calculated for a given exposure. In the case of the 82.35 kgd data-set of the L1- and L2-data $N_{exp} = 1880$ events are expected. A total number of $N_{det} = 1930$ events are found, applying a z-cut from $0.95 < z < 1.1$ and an energy window from $E = (2900 \ldots 3300)$ keV (figure 3.42), which is in very good agreement with the expectation. The validity of this assumption is supported by the *z(E)*-plot. It is obvious, that the ^{190}Pt contribution is limited to the cathode and anode region, only. The energy entries in the anode region at z=0 are shifted due to the double-energy-effect (figure 3.43). The contribution of ^{210}Po at the cathode originates from an accumulation of radioactive daughters of the ^{222}Rn decay during the operation of the detectors in normal laboratory air environment. The ^{222}Rn is formed in the ^{238}U decay chain and piles up to an activity in the range of $A \sim 100$ Bq/m^3 air, depending on the material used for the construction of the building and geological formations the building is founded on. ^{222}Rn has a half-life of $T_{1/2} = 3.8$ days and decays via α-emission with Q_α=5590.3 keV. As it is an inert, noble gas and it is very volatile ^{222}Rn can reach the experimental setup by simple diffusion. The ^{222}Rn-atom decay forms a charged secondary ion ^{218}Po$^+$ which gets attracted from

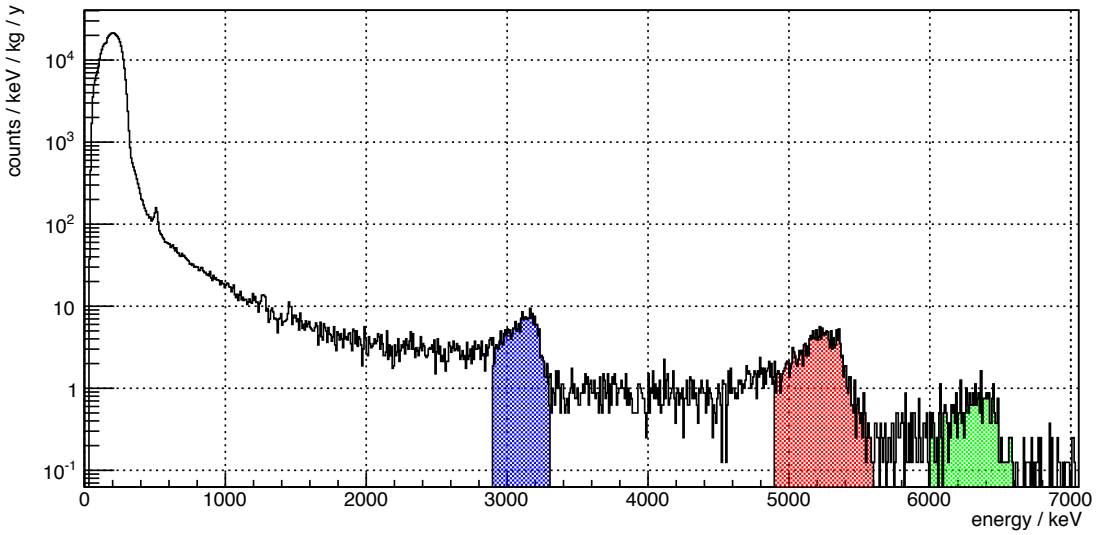

Figure 3.42: The contribution of the clearly identifyable ^{190}Pt and ^{210}Po to the background of the 82.3 kgd exposure of the L1 and L2 data from the LNGS. Blue: ^{190}Pt-decays at the cathode (1932); red: ^{210}Po at the cathode (1673); green: energy doubled ^{190}Pt-decays at the anode (296). Due to the lower coverage at the anode, the number of ^{190}Pt events is reduced here.

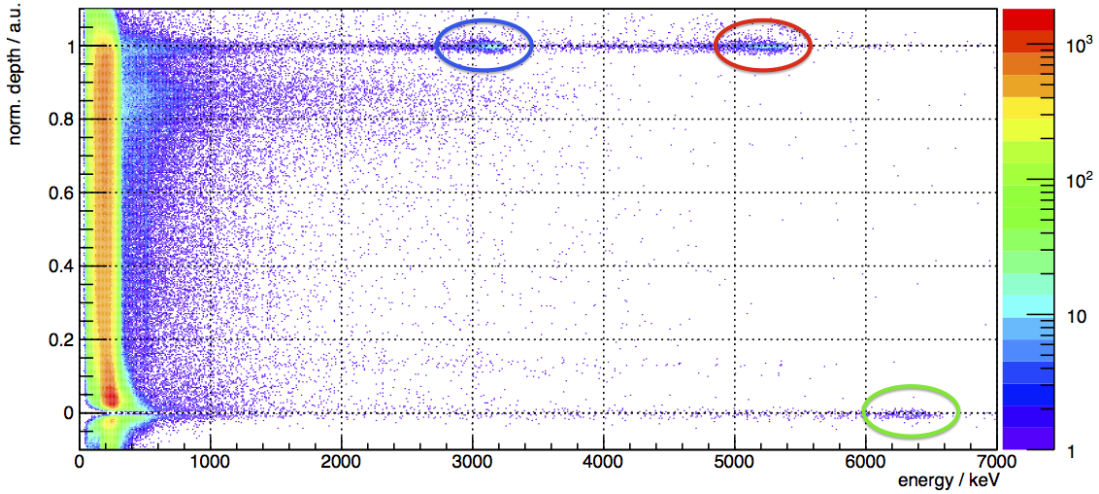

Figure 3.43: $z(E)$-Plot of the 82.3 kgd exposure of the L1 and L2 data from the LNGS. The population at the cathode at z=1 is mainly caused by alphas from ^{190}Pt (blue marker) and ^{210}Po (red marker). At the anode side the number of ^{190}Pt events is reduced due to the lower coverage of the metallization (green marker). ^{210}Po events are not detectable at the anode as they are energetically doubled and reach the point of saturation at ca. 9 MeV.

the negatively biased cathode. In the subsequent decays the following short lived isotopes are formed: ^{218}Po ($T_{1/2}$ =3 min); ^{214}Pb ($T_{1/2}$ =27 min); ^{214}Bi ($T_{1/2}$ = 20 min) and ^{214}Po with an half-life of just $T_{1/2}$ = 164 µs (figure 3.44). ^{214}Po decays to the relatively stable ^{210}Pb ($T_{1/2}$ =22 yr) that contaminates the detectors surface, especially the cathode. In two subsequent β-decays ^{210}Bi and the α-decaying ^{210}Po are formed. The decay of the ^{210}Po can be observed during the lifetime of the experiment (figure 3.43). The problem with ^{210}Po over the ^{190}Pt is, that the position of the platinum is well known, as it is deposited at the anode and the cathode, only, whereas the lead isotope can theoretically be spread over the whole detector surface. In this case the z-cut can not remove the ^{210}Pb events that originate from the sidewalls of the detector. Additionally, these sidewall-alphas are partly blocked by the encapsulation and are shifted towards lower energies due to the energy loss in the lacquer. This is problematic as the Q-value of the ^{210}Po-decay is 5.407 MeV. If α-particles from this decay lose energy before they are detected, they can generate entries in the ROI of the searched $\beta\beta$-decay.

Figure 3.44: Lower part of the ^{238}U decay chain starting at ^{222}Rn and processing down to ^{206}Pb to illustrate the accumulation of ^{210}Po at the cathode [Cen18]

3.6.2 Analysis of the Pulse Shapes of α- and β-Events

To analyze for a possible way to discriminate α- and β-events an idealized lab-experiment is performed. In this experiment the cathode of a 1 cm^3 CZT detector is irradiated with α- and β-particles. To assure a perpendicular impact of the ionizing particles and to limit the irradiated area to a narrow window in the center of the cathode two collimators are used. For the collimation of the α-particles the window at the backside of the plastic detector mount is sufficient, for the β-particles a 5 mm thick steel disk with a 3 mm drill-hole is used. As radiation sources a combined ^{239}Pu/^{241}Am/^{244}Cm α-source with an activity of A = 3 kBq and a ^{90}Sr/^{90}Y β-source with an activity of A = 72 kBq are used. The α-source is installed at two different distances, with d_1 = 1 cm and d_2 = 4 cm, to simulate different alpha energies over a wide energy range. The highest available β-energy is the combined spectrum of the ^{90}Sr/^{90}Y decay with Q-values of $Q_{^{90}\mathrm{Sr}}$=0.546 MeV and $Q_{^{90}\mathrm{Y}}$=2.282 MeV, respectively. Due to the construction of the source and the distance between the detector and the source the full Q-value of the decay can not be observed (figure 3.45).

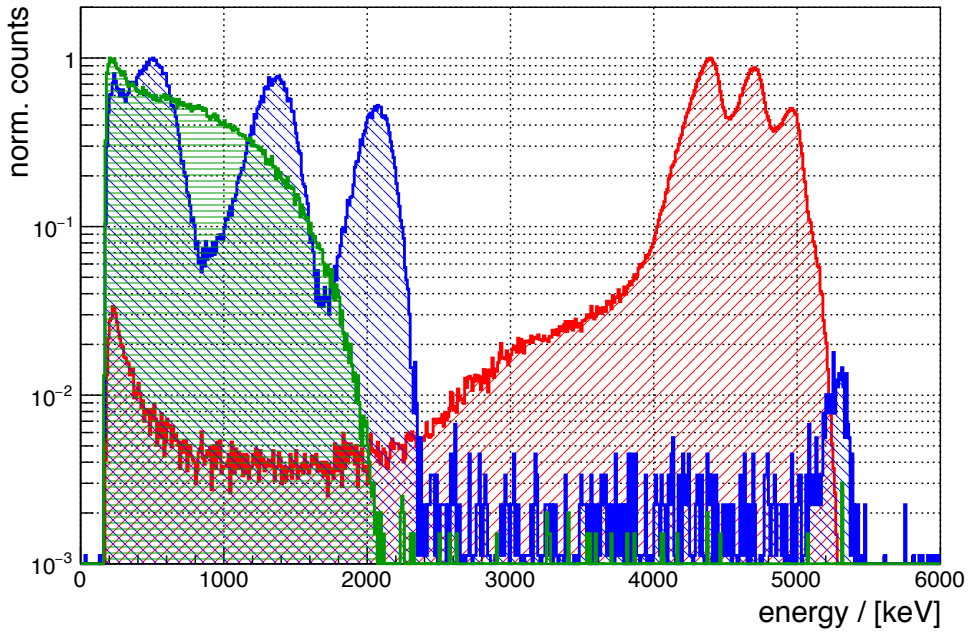

Figure 3.45: Overlay of the normalized pulse height spectra of the combined ^{239}Pu/^{241}Am/^{244}Cm α-source at 1 cm distance to cathode (red) and 4 cm (blue) and the ^{90}Sr/^{90}Y β-source at 6 cm (green).

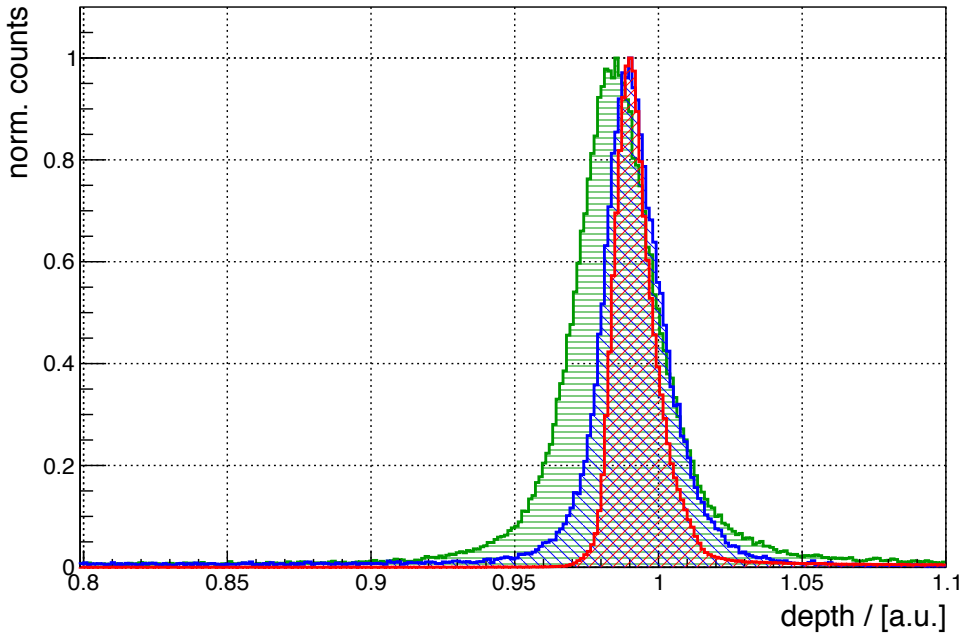

Figure 3.46: Comparison of the reconstructed depth of 1 cm (red) and 4 cm (blue) α-events and β-events (green).

The energy calibration is performed with an ^{137}Cs and an ^{60}Co source in advance. The difference in the interaction of α- and β-particles with matter could result in differences in the pulse shape of the event. As the α- and β-irradiations are performed independently the single events can be attributed clearly to the specific type of interaction. In a first step the depth distribution of the events is analyzed. From the physics of interaction it is expected, that the β-events show a broader distribution compared to the short ranging α-particles, which is observed (figure 3.46).
The α-events (red and blue histograms) are clearly clustering around $z = 0.99$ with a sharper distribution compared to the β-events (green). For the α-particles the reconstruction should result in a sharp peak at '1' as the range of α-particles in CZT is only a few µm. This demonstrates the general limitation in the precision of the depth reconstruction algorithm. Even though the irradiation is applied only at the cathode, the reconstruction yields ranges of up to several 100 µm for the α-particles, which is way too large. Nevertheless, it can be shown, that the z-cut, ranging from $0.97 \leq z \leq 1.05$, covers the majority of the α-particles impinging from the cathode side $\epsilon = 0.992$ for the 1 cm distance irradiation (red histogram). In the case of the 4 cm distance (blue histogram) the efficiency of the cut is reduced to $\epsilon = 0.85$ due to the broader distribution of the depth reconstruction for the lower energy alphas. The mean peak position of the reconstructed events is in both α-cases at 0.99 and so very close to the cathode. The mean distribution of the reconstructed depth for different energy bins are shown for the α-events in figure 3.47 and the β-events in figure 3.48. The plots are displaying

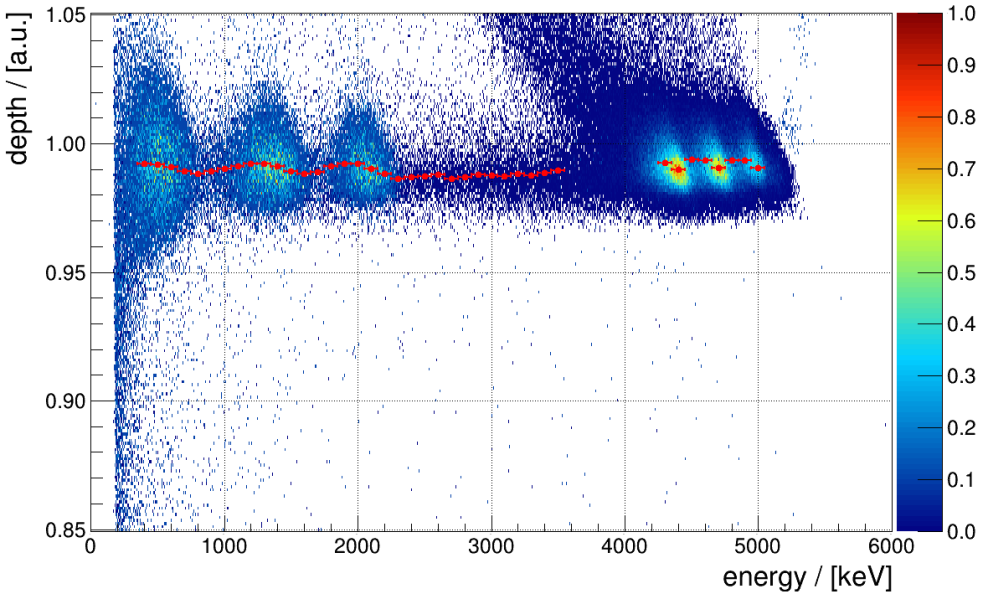

Figure 3.47: Heat-Plots of the $z(E)$-distribution of the α-irradiations. Superimposed is the mean-value of the reconstructed depth for the respective energy bin (red). ^{239}Pu/^{241}Am/^{244}Cm α-source at 1 cm and 4 cm distance.

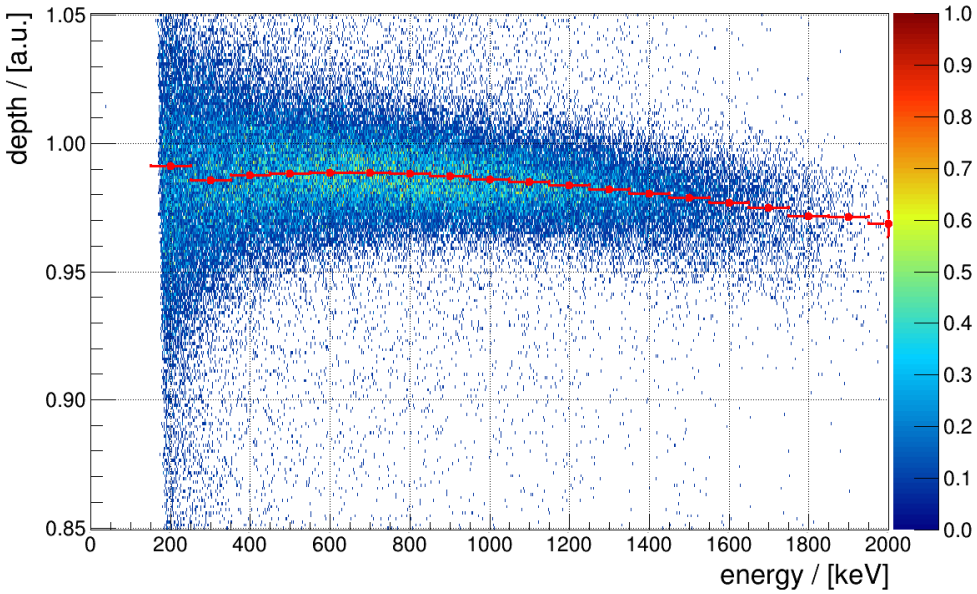

Figure 3.48: Heat-Plots of the $z(E)$-distribution of the ^{90}Sr/^{90}Y-irradiation. Superimposed is the mean-value of the reconstructed depth for the respective energy bin (red).

the heat-maps of the z-over-E distributions of the α-events and β-events. Superimposed is the mean of the reconstructed depth distribution for the respective energy bin. The errors of the mean are too small to be displayed. For the α-events the reconstructed depth is almost constant at $z_\alpha = (0.99 \pm 0.005)$ for the full energy range. Caused by the longer random walk of high energetic electrons in matter, a clear tendency for a deeper penetration with increasing energy is visible for the β-events. A selection of pulse shapes from the α- and β-events is displayed in figure 3.49. On the left side the NCA pulses of the energy window $E = 1800..1900\,\text{keV}$ are shown, the corresponding CA signals are displayed on the right side. The β-events are shifted by 100 ADC-units for better comparison.
Qualitatively no differences between the α- and β-events are evident. Interestingly, the drift of the charge cloud throughout the detector is not linear for this specific detector. A clear reduction in the rise of the charge signal is visible in the second part of the drift path which is expressed in a slightly downwards bended pulse shape starting at about 40% of the drift path. This behavior is observed for the CA and NCA signals as well and, hence, can be attributed to the detector itself. For the detectors at the LNGS such a behavior is not observed.
To test for possible differences of α- and β-induced events of the same energy, the rising slope of the NCA pulse shape signal is analyzed. Due to the different ranges of the ionization process of α- and β-events differences in the size of the generated charge cloud are expected. Therefore, the analysis is performed at the 20..80% step height of the NCA signal. This is possible as the drift of the charge cloud through the detector induces the same signal at the CA and NCA until the charge cloud reaches the scope

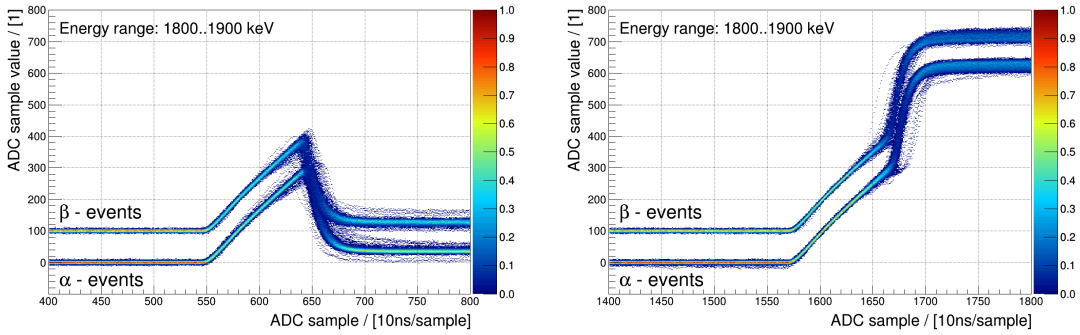

Figure 3.49: Overlay of the α- and β-event pulse shapes for two different energy ranges. Left: NCA pulse shapes, right: corresponding CA pulse shape. The β-events are shifted by 100 ADC-units for better comparison.

of the grid bias field of the NCA (section 2.2.3). In figure 3.50 the overlay of the the 1800..1900 keV α-events are plotted exemplarily. For each event the slope of the sample between 20% and 80% of the maximum pulse height is analyzed.

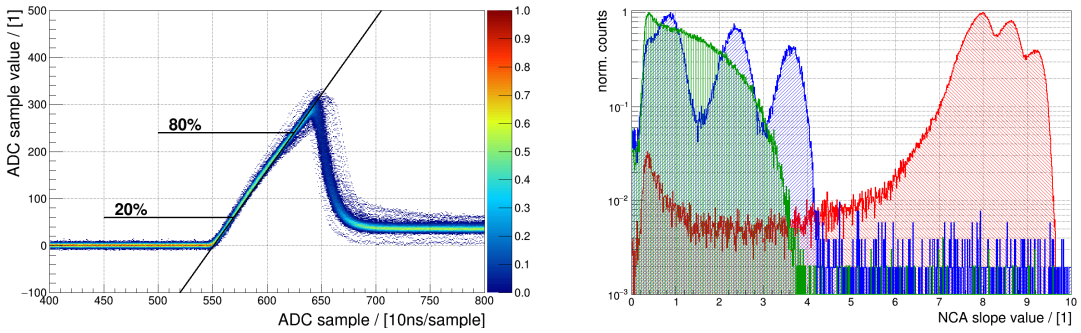

Figure 3.50: Left: Overlay of the NCA pulses of the $E = 1800..1900\,\mathrm{keV}$ α-events. The 20% and 80% levels are tagged. The slope between this two points is analyzed. Right: Reproduction of the energy spectra based on the NCA slope distribution.

This value can be used to reconstruct the total energy deposition, too. Due to noise induced limitations of the single events the determination of the maximum peak height is affected and distorts the precise determination of this point. Nevertheless, in the given case the distribution of the NCA slope values greatly reproduces the energy spectra of the irradiation. The NCA slope based measured energy resolution is 10% for the ^{239}Pu α-peak at $E = 4.4\,\mathrm{MeV}$, whereas it is 6% based on the pulse height based evaluation. I The linearity of the energy versus NCA slope is tested for both types of events. For this analysis the energy versus the determined NCA slope value is plotted for each event. A linear correlation between energy and NCA slope is assumed and superimposed in red. As displayed in figure 3.51 no difference in the general correlation between

the energy and the NCA slope is found. The slight deviation of the approximation and the data for the $d = 1\,\text{cm}$ distance α-experiment (upper left in figure 3.51) is caused by the strong difference in the population of events over the wide energy range.

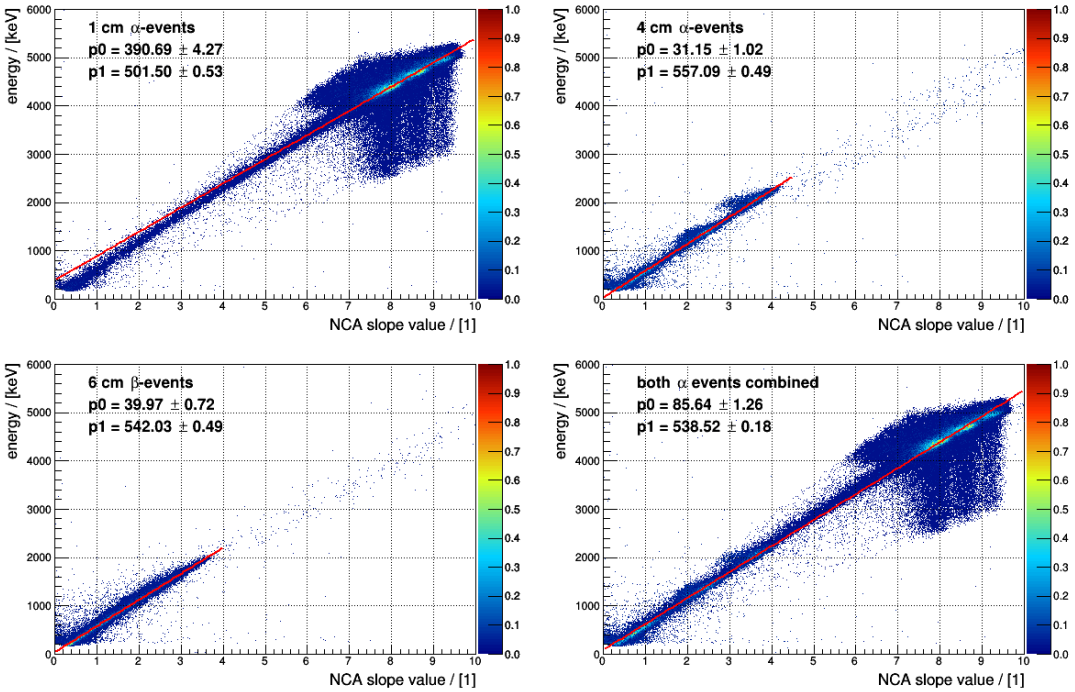

Figure 3.51: Comparison of the correlation between energy and NCA slope for the different experimental conditions. A linear approximation is superimposed. The p0 and p1 values for the linear function are given.

Table 3.7: Evaluated parameters of the linear approximation

particle	distance	p0-value	p1-value
α	1 cm	390.69±4.27	501.50±0.53
α	4 cm	31.15±4.27	557.09±0.49
α	combined	85.64±1.26	538.52±0.18
β	6 cm	39.97±0.72	542.03±0.49

If the $d = 1\,\text{cm}$ and $d = 4\,\text{cm}$ α-measurements are combined, the fit reproduces the data much better. In fact, the linear approximation yields almost the same p0 and p1 values for α- and β-events if the β-values and the values deduced from the combined α-measurements are compared (Table 3.7). From that evaluation it must be concluded, that the energy versus NCA slope analysis does not yield a suitable measure to differentiate between α- and β-events.
To test for possible drift time variations of α- and β-events the time between the 20%- and 80%-level of the NCA peak signal is analyzed. At the left hand side of figure

3.52 the pulse shapes of α- and β-events of the 1800..1900 keV energy bin are plotted. For each event the drift time is measured in the indicated region. The distribution of the drift times for the same energy bin is shown at the right hand side of figure 3.52. A gaussian distribution is superimposed. This energy bin is the one with the largest discrepancy in the measured drift times of α- and β-events.

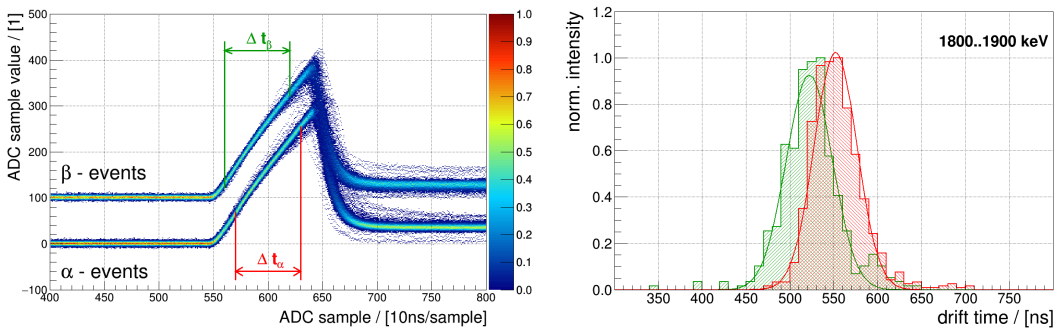

Figure 3.52: Left: Overlay of the NCA pulses of the $E = 1800..1900$ keV α- and β-events. The drift time is measured between the 20% and 80% levels of the NCA signal for each event. Right: The normalized distribution of the measured drift times of α- and β-events.

The combined data of the lab-experiment is plotted in figure 3.53. The mean value (marker) and the sigma of the fit to the drift time variations (error bars) for the respective energy bin are shown for both particles. Even if there is a slight separation between α- and β-drift times observable, starting at about $E = 1000$ keV, the distributions still overlaps significantly, such that a clear differentiation between events caused by the two particle types is currently not possible. In a follow-up experiment a β-source with a higher Q-value could be used to test if the observed separation continues for higher energies and if a suitable indicator to distinguish α- and β-events can be deduced from this indication.
To probe for differences of the sampled pulse shapes and derivatives of the pulse shapes, the data is binned 100 keV-wise for analysis. For each bin the averaged pulses and derivatives from the averaged pulses are calculated to allow for a direct comparison between α- and β-events. In figure 3.54 the pulses of collecting anode (CA), non-collecting anode (NCA), difference pulse (DIFF), reconstructed cathode pulse (CATH) and the first derivatives of each pulse are plotted for the $E = 1300..1400$ keV energy bin.
At first glance, no major difference between the two types of interaction are obvious. The little variations are caused by the different reconstructed depths for α- and β-particles of the same energy bin. Again, the strange drifting behavior of the charge transport during the drift in the linear weighting field for this detector gets visible. The signal should not be accelerated or decelerated during the move between the HV-biased cathode and the influence of the grid bias from the NCA but should move constantly between sample 550 and sample 630. In contrast to the expectation a deceleration is observed - most obviously at the reconstructed cathode signal, as this is a linear combination of the CA and NCA.

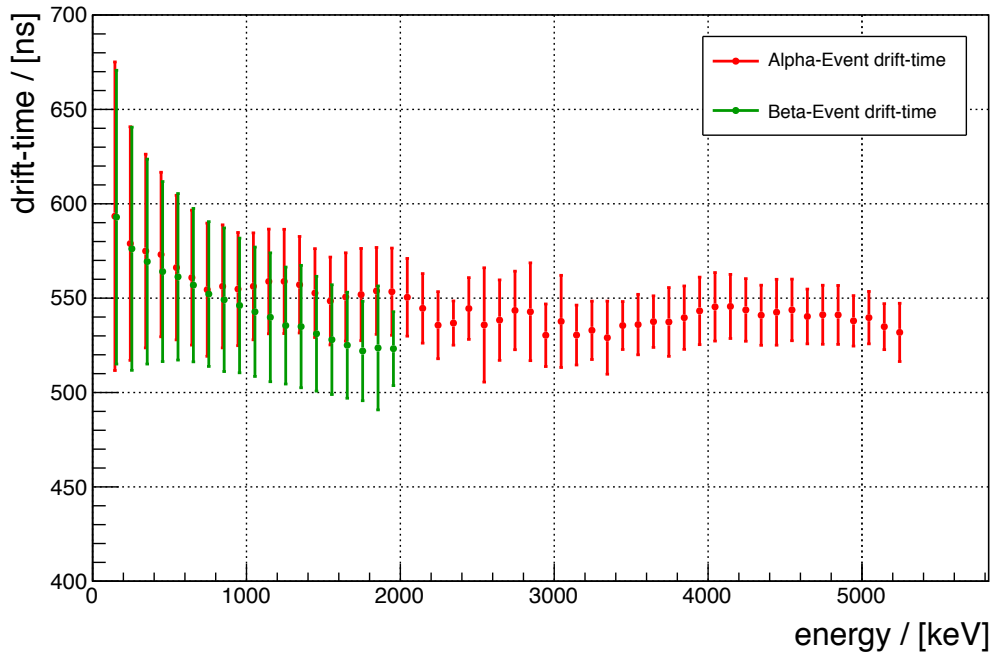

Figure 3.53: Comparison of the drift time between the 20% and 80% NCA signal level for cathode induced α- and β-events.

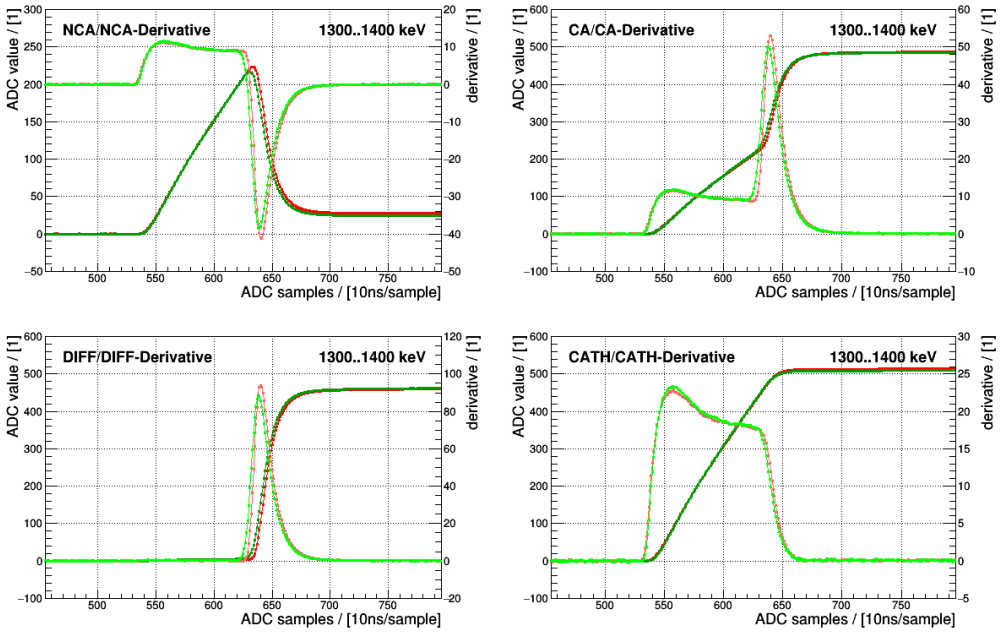

Figure 3.54: Overlay of the averaged NCA, CA, DIFF and CATH pulses with its respective first derivatives of the $E = 1300..1400\,\text{keV}$ energy bin. The darker colors represent the sampled/reconstructed values (red: α-events, green: β-events), the lighter colors represent the respective derivatives.

The close-up inspection of the averaged difference pulse reveals little but steady differences between the α- and β-events for all energy bins at the point the grid bias starts to affect the charge carrier movement. As shown in figure 3.55 the reconstructed DIFF-pulse of the α-event (dark red marker) shows a clear kink right before the charge cloud starts to move towards the collecting anode at about sample 630. The plot depicts the

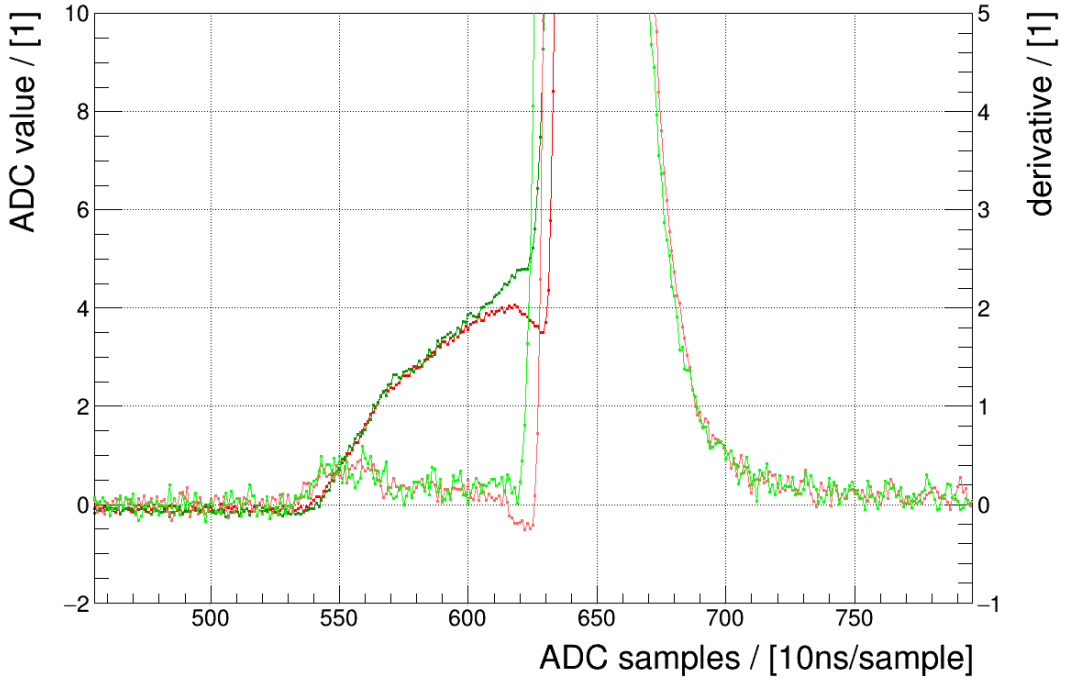

Figure 3.55: Close-up of DIFF pulses and DIFF-DERIVATIVE of the 1300..1400 keV energy bin. The darker colors represent the reconstructed DIFF-values (red: α-events, green: β-events), the lighter colors indicating the DIFF-DERIVATIVE.

averaged samples of the $E = 1300..1400\,\text{keV}$ energy bin of both particle interactions. The kink of the α-events is more prominent in the DIFF pulse itself than in the DIFF-DERIVATIVE. The observed feature can be found mainly for the strongly α-populated parts in the spectrum (compare figure 3.56) whereas in the less frequented energy regions the feature is not that clearly developed. It must be noted, that the difference between the strong and weak populated area in the α-spectrum spreads over one order of magnitude in counts (figure 3.45). So, this effect is only visible, if a mean pulse is calculated from a large number of samples with float precision for the ADC values, whereas single events are sampled as integer values. In general, it is possible to develop an automated routine to detect such kinks - especially since there is no kink observed for the β-events in the DIFF pulse. The main problem is, that the effect is very small. Even for the strongest affected signal in the energy range of $E = 1800..1900\,\text{keV}$ the difference between peek and bottom of the kink is only about 1 ADC value. In contrast to this difference the absolute value of the DIFF-signal is more than 500 ADC values.

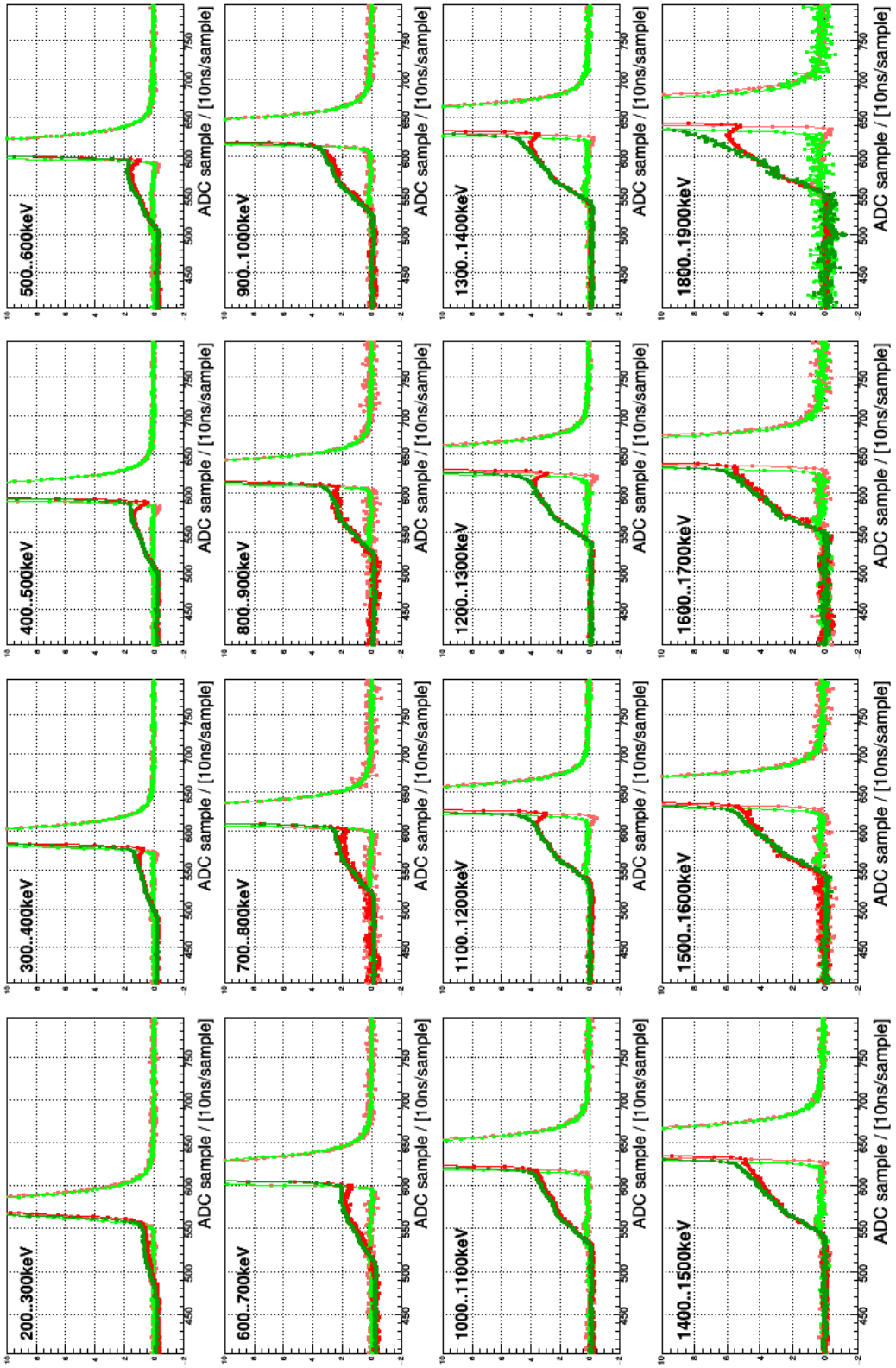

Figure 3.56: Overlay of the mean DIFF and mean DIFF-DERIVATIVE pulses of α- and β-events for a choice of energy bins.

Even more problematic is, that the single pulses are affected by electromagnetic interferences which mask the kink-signal searched for.
Taking all this into account, it must be concluded, that the observed difference lies below the resolution of the used ADCs and is overlaid by electromagnetic interferences of the real pulses. Hence, a sure differentiation of α- or β-induced events based on the pulse shape analysis, only, is not possible.

3.7 Investigations on the Long-term Stability of Underground Operated CZT Detectors

3.7.1 Measurement Strategy

Since the detectors are made from natural cadmium containing 12.2% ^{113}Cd and as they are operated in an ultra low-background environment, the intrinsic, fourfold forbidden non-unique single beta-decay of $^{113}\mathrm{Cd}^{\left(\frac{1}{2}+\right)} \rightarrow {}^{113}\mathrm{In}^{\left(\frac{9}{2}+\right)}$ is by far the most intense signal. The decay of ^{113}Cd is a direct beta-decay into the ground state of ^{113}In. Hence, the spectrum is continuously spread over the allowed energy range from zero to the Q-value of the decay, $Q = (322.2 \pm 1.2)\,\mathrm{keV}$ [DRW$^+$09]. It can be used to monitor the stability of the detectors by analyzing the decay rate of this isotope. The theoretically expected rate of ^{113}Cd decays is about 400 per day and detector, assuming 5.9 g detector mass, 5.0 at% zinc concentration and 100% detection efficiency for this low energetic β-decay. Currently, the shape of the ^{113}Cd spectrum in the range below 100 keV is not well known and experimental data is strongly requested [Bea07, Mea07, Mea06]. The long half-life of ^{113}Cd of $T_{1/2} = (8.00 \pm 0.35) \times 10^{15}\,\mathrm{yr}$ [DRW$^+$09] and its homogeneous distribution inside the CZT detector should result in a constant decay rate over the time of operation. Changes in the measured decay rate can indicate an alteration of the detector properties which could have a negative effect on the overall performance of the experiment.

3.7.2 Selection Criteria and Measurements

Due to the uncertainty in the shape of the ^{113}Cd spectrum, the stability analysis is limited to runs with the lowest common energy threshold for each detector. The energy threshold defines the amplitude of the pulse shape that must be exceeded to trigger the data acquisition system for recording and storing events. The thresholds for the detectors are adjusted on a run-by-run basis with the aim to reach the lowest possible energy threshold. In figure 3.57 the time dependent threshold of a selection of detectors is displayed exemplarily. The full set of data for the other detectors can be found in figure 3.65 at the end of this chapter. It can be seen, that with the installation of additional detector layers the thresholds had to be raised. This is caused by additional electromagnetic noise that is introduced into the setup by the multiplied number of cables and the additional preamplifier boxes necessary for the operation. In September 2014 a program for an optimization of the thresholds was started, which allows to

lower the thresholds for a number of detectors. However, it is possible to reach the low thresholds again that L1 was operated at briefly before L2 installation. Several measures are necessary to enable the setup to run at ultra-low thresholds again, which would imply additional cooling to lowest possible temperature, separate operation of L1 and L4 and independent supply of the preamp boxes.

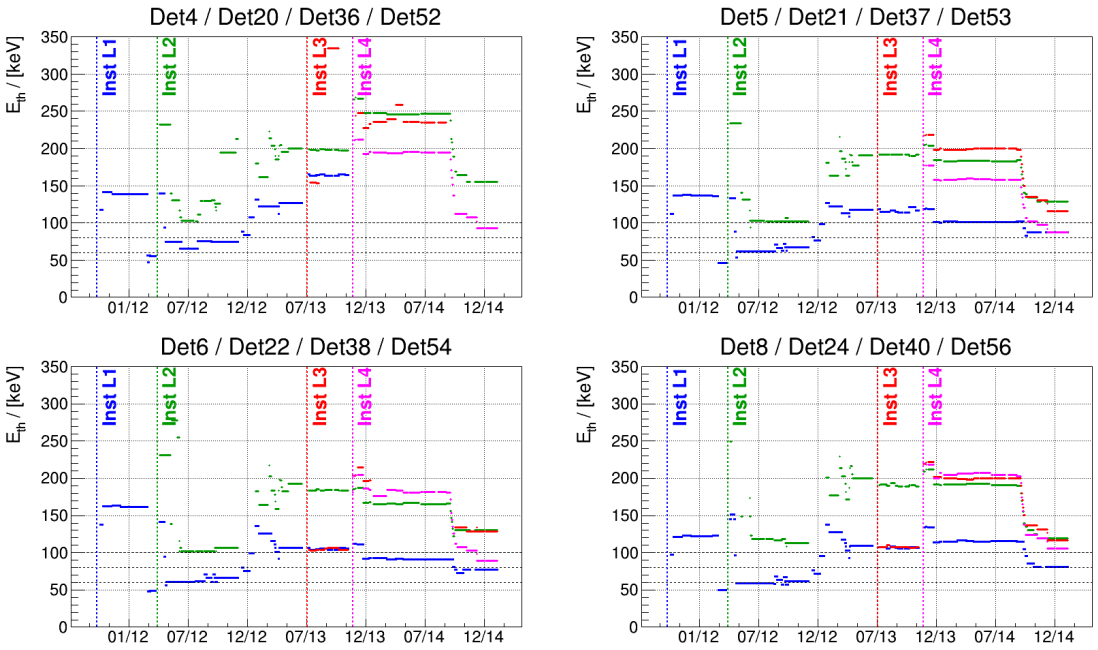

Figure 3.57: The time dependent threshold settings for a selection of detectors is plotted here. The installation of Layer L1, L2, L3 and L4 is indicated.

Due to this time dependent threshold, the available lifetime per energy bin depends on the observed energy interval for each detector. Runs with thresholds of $E_{th} > 250\,\mathrm{keV}$ are discarded for the stability analysis to avoid too large statistical uncertainties of the detected count rate. An optimization procedure is applied to identify the optimal threshold E_{opt}, to maximize the count rate and to minimize the statistical uncertainties. In this approach, the total number of counts are maximized for each detector as a function of the available lifetime per energy bin (figure 3.58). It is to be seen, that for Det6 the configuration with $E_{th} = 160\,\mathrm{keV}$ yields the largest total lifetime but due to the spectral shape of the ^{113}Cd spectrum (figure 3.59) it does not result the best statistical data. In this case the E_{opt} can be found at $E = 115\,\mathrm{keV}$ as it covers a larger part of the spectrum even at lower total exposure.
In figure 3.59, the total spectrum of one detector is shown in blue. The available, threshold-dependent detector lifetime in days is plotted in red. Data taken below the optimal threshold are not used for the stability analysis. The lifetime distribution shows that for lower energies the available lifetime of the detector drops fast and for energies below $E_{th} = 60\,\mathrm{keV}$ it is less than 20 days. For the stability analysis, an additional

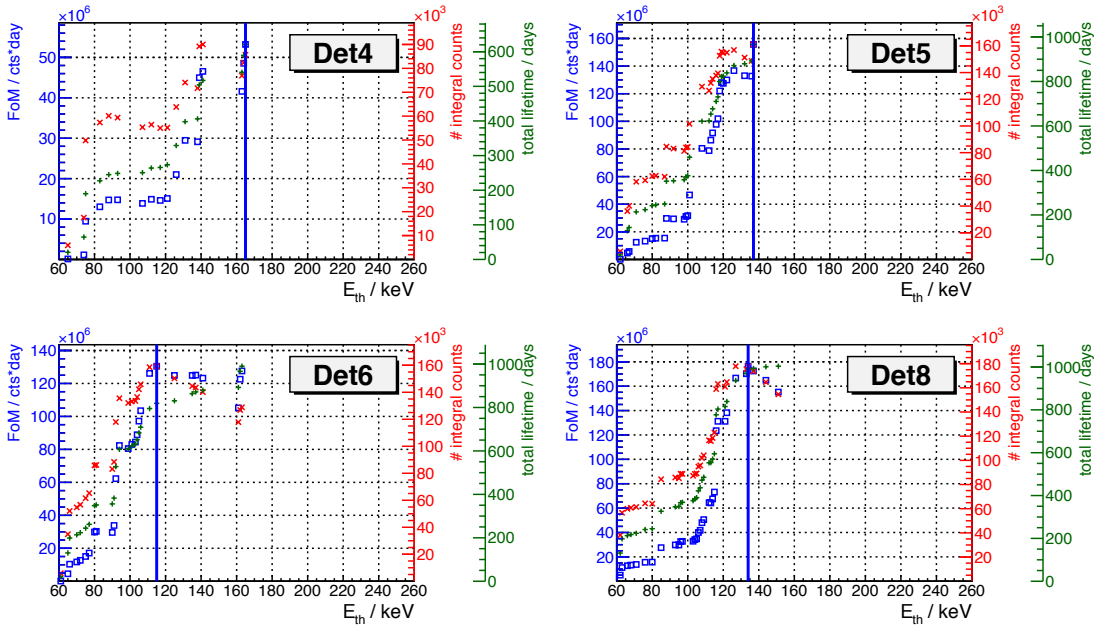

Figure 3.58: In blue the "Figure of Merit" in counts×day is plotted. The red marker indicate the total counts in the respective energy bin, in green the respective lifetime of this energy bin is given. Due to the spectral shape of the ^{113}Cd spectrum and the limited available lifetime per energy bin the FoM gives the optimal threshold energy for the stability analysis.

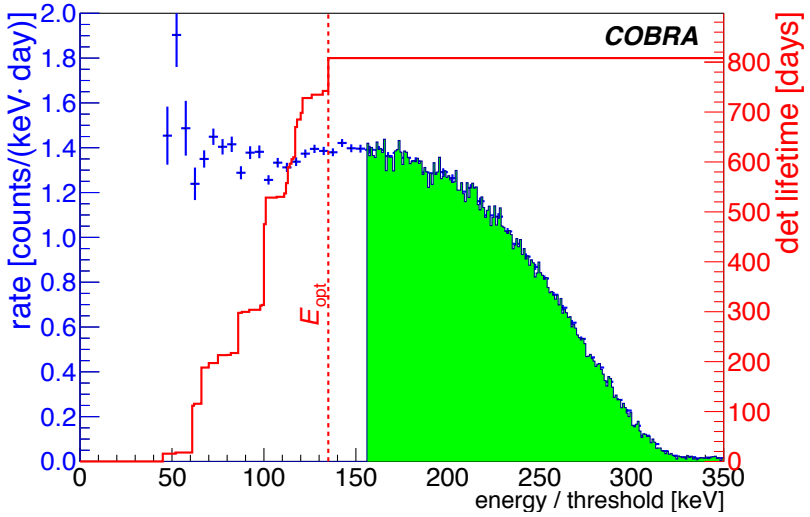

Figure 3.59: Exemplarily, in blue the total ^{113}Cd spectrum of one detector is plotted. The green part of the spectrum is used for the stability analysis. The threshold dependent lifetime of the detector is shown in red. The different lifetimes per energy bins are caused by the operation of the detector at adjusted thresholds in the subsequent runs.

+20 keV offset is applied to E_{opt}. This accounts for the limited energy resolution in that energy range. The remaining part of the spectrum, shown as green histogram, is used for the stability analysis. Runs with an energy thresholds higher than E_{opt} are discarded.
A further limitation is caused by the working principle of the coplanar grid. The pulse-shape analysis used in the COBRA Demonstrator allows for the reconstruction of the depth of interaction (DOI) and to judge if the interaction happened at the lateral surfaces of the detector [Fea13, Fea14]. It is known that in the vicinity of the anodes the presence of the grid bias field distorts the movement of the charge carriers. This distortion alters the energy- and depth-reconstruction for energy deposits close to the anodes. For this reason, a second, static depth-cut is used to limit the fiducial volume to the section where the energy and depth are reconstructed correctly. The static depth-cut selects the region $\geq$0.2 and $\leq$0.97 of normalized depth and, hence, excludes the effect of the hole shift [Fea13] in the vicinity of the anodes.

3.7.3 Observed ^{113}Cd Decay Rate Variations

The operation under ultra low-background conditions and the analysis of the high-energy part of the spectrum allows to neglect further contributions from other background sources in the analyzed energy range from $E = (100 \ldots 350)$ keV for the stability analysis. It is therefore assumed, that the ^{113}Cd signal region is not contaminated by background. To analyze for the stability of the detected ^{113}Cd decay rate, the data is partitioned into ten-days real-time intervals. For the respective interval the lifetime has to be at least five days to be considered. The optimal threshold-cut and the static depth-cut are applied for each detector, respectively. The remaining ^{113}Cd counts are summed up and normalized to the lifetime in the respective time period. Due to the different optimal thresholds of each detector, the observed absolute decay-rate deviates from one device to another. The measured ^{113}Cd decay rates of detectors Det4, Det5, Det6 and Det8 of L1 are shown in figure 3.60 with red markers. The detectors were operated at all times. Missing data points indicate an operation above the optimal energy threshold in the specific time period which led to a removal of the run. A robust, linear approximation is superimposed. The grey boxes indicate excluded time periods (Jul'13 - Nov'13 and Jul'14 - Sep'14), which were affected by electromagnetic interferences that caused an increased baseline noise. This noise led to a higher rejection rate of triggered events and, thus, accidentally removed low-energetic physics events. The ^{113}Cd rate is especially affected since the deposited energy is always below $E = 322$ keV. Hence, it was decided to exclude the data from these time periods for the evaluation.
Det4 shows the strongest decrease of the ^{113}Cd count rate in L1 with $\Delta_{Det4} = -5.2\%$ per year, whereas Det6 is the only detector that shows a slight increase of the detected count rate with $\Delta_{Det6} = +1.4\%$ per year. All other detectors are in between those values for the observed rate variations. For Det8, the measured decay rate of the ^{113}Cd is basically constant over the full time period, excluding the electronically disturbed runs. This detector yields one of the largest data sets with more than 810 days accepted lifetime. As the detectors are produced using material from different batches, the single

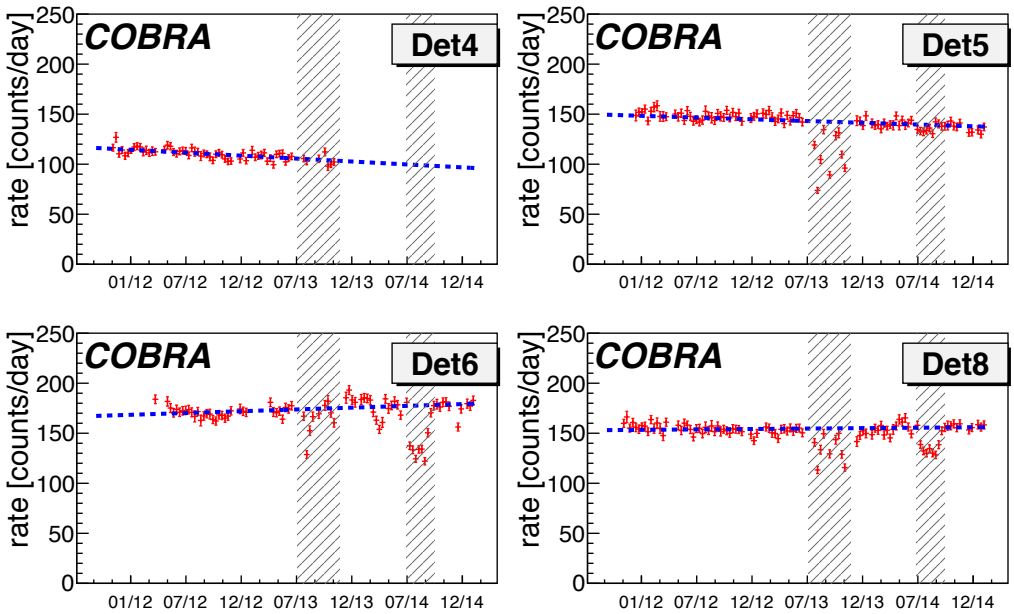

Figure 3.60: The threshold dependent ^{113}Cd decay rate of Det4, Det5, Det6 and Det8 of L1. The data is partitioned into ten day intervals, whereas the rate is calculated in counts/day in the analyzed part of the spectrum and varies due to the different optimal thresholds. The uncertainties on the rate are purely statistical in nature. A linear approximation is superimposed in blue. The grey boxes indicate excluded time periods.

layers have to be considered independently. The layers were installed subsequently with several months (L1 and L2) or more than one year delay (L3 and L4). Furthermore, L3 is still not performing as well as the other detector layers and is excluded from the following considerations. This layer is generally more affected by electronic noise and the overall detector performance lags behind those of the other detectors in terms of energy resolution. Additionally, the considered exposure of L3 and L4 is only about one third of those of L1 and L2, which results in fewer time periods and larger uncertainties for the linear approximation. For L1, the average accepted lifetime of the detectors is roughly 700 days whereas it is for L2 630 days, for L3 300 days and for L4 it is only 270 days. Nevertheless, the detected count rate variations are relatively low. Beside the excluded time periods no significant outliers are found that would indicate a drastic change of the detector properties or of the data acquisition chain. This can be seen in table 3.8. The relative change in count rate per year and detector is plotted in figure 3.61. The error bars indicate the uncertainty of the linear approximation on the data which is basically related to statistical uncertainties. 45 out of 48 detectors from L1, L2 and L4 show a change in the decay rate well below ±6% per year. The shorter overall lifetime and the higher optimal thresholds of the detectors of L4 affects the accuracy of the approximation as only a smaller part of the spectrum is analyzed and fewer accepted run periods are available. Nevertheless, a weighted mean of the slope of $\bar{p}_1 = (0.995 \pm 0.004)$ can be reported, which indicates an almost perfect stable

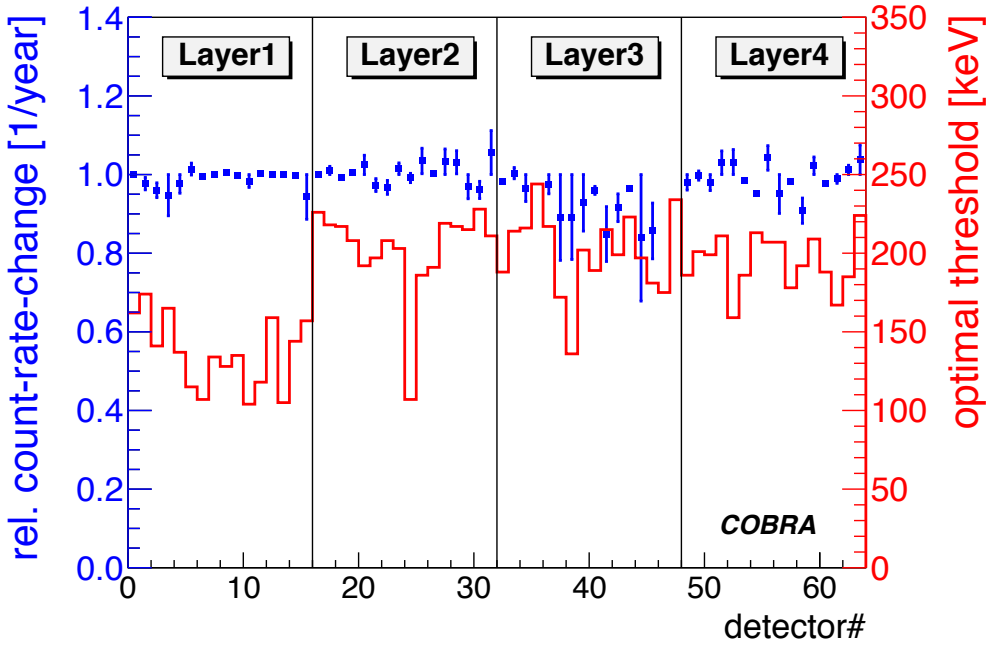

Figure 3.61: The relative ^{113}Cd count rate change on a per year basis is plotted in blue. In red the respective optimal threshold per detector is shown.

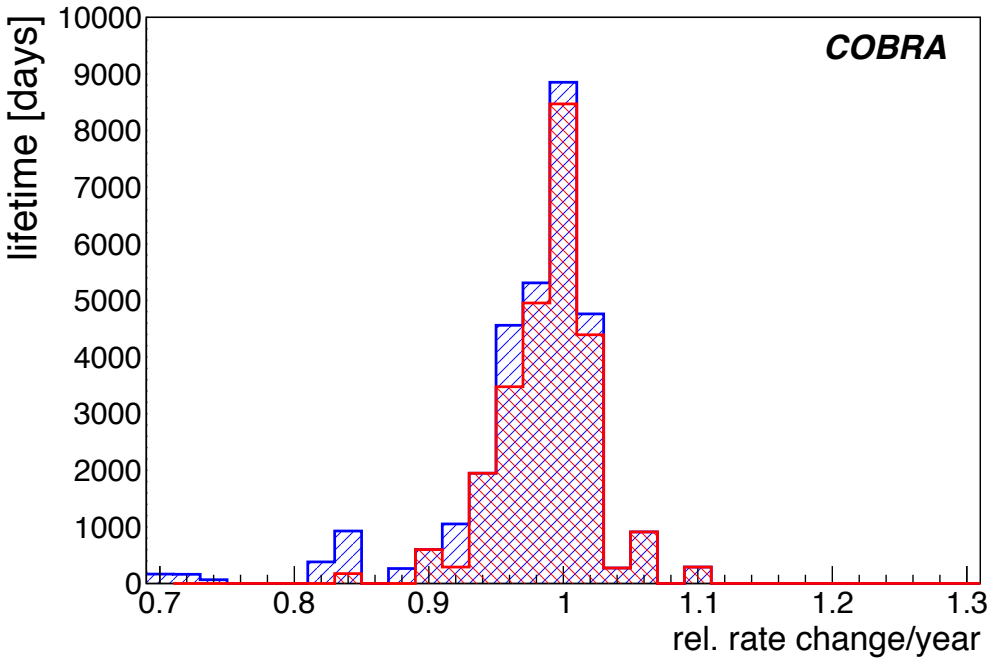

Figure 3.62: The lifetime-weighted distribution of the relative rate change of all Layers (blue) and Layer1, Layer2 and Layer4 in red.

Table 3.8: Relative ^{113}Cd decay rate variations per year for each detector. L1, L2 and L4 are considered for the stability analysis. L3 is excluded due to general performance problems in the low-energy range.

Layer 1	relative rate change / yr	Layer 2	relative rate change / yr
Det1	1.000±0.004	Det17	1.001±0.001
Det2	0.977±0.016	Det18	1.010±0.010
Det3	0.960±0.019	Det19	0.993±0.001
Det4	0.948±0.052	Det20	1.006±0.006
Det5	0.976±0.024	Det21	1.025±0.025
Det6	1.014±0.015	Det22	0.973±0.016
Det7	0.996±0.004	Det23	0.967±0.018
Det8	1.000±0.002	Det24	1.015±0.015
Det9	1.005±0.005	Det25	0.991±0.012
Det10	0.998±0.005	Det26	1.035±0.032
Det11	0.984±0.016	Det27	1.003±0.007
Det12	1.004±0.004	Det28	1.033±0.033
Det13	0.999±0.001	Det29	1.031±0.029
Det14	1.001±0.003	Det30	0.969±0.031
Det15	0.998±0.002	Det31	0.961±0.022
Det16	0.943±0.057	Det32	1.056±0.056
Layer 3	relative rate change / yr	Layer 4	relative rate change / yr
Det33	0.982±0.001	Det49	0.980±0.020
Det34	1.004±0.014	Det50	0.997±0.012
Det35	0.966±0.034	Det51	0.980±0.020
Det36	0.695±0.305	Det52	1.030±0.030
Det37	0.976±0.024	Det53	1.032±0.032
Det38	0.891±0.109	Det54	0.985±0.006
Det39	0.892±0.108	Det55	0.951±0.006
Det40	0.928±0.072	Det56	1.042±0.031
Det41	0.960±0.010	Det57	0.951±0.049
Det42	0.849±0.070	Det58	0.983±0.002
Det43	0.916±0.035	Det59	0.908±0.032
Det44	0.964±0.004	Det60	1.022±0.022
Det45	0.839±0.161	Det61	0.978±0.002
Det46	0.857±0.071	Det62	0.989±0.011
Det47	0.705±0.295	Det63	1.012±0.012
Det48	0.733±0.267	Det64	1.038±0.038

operation of the detectors. Figure 3.62 displays the lifetime-weighted relative change rate distribution for all layers (blue) and for L1, L2 and L4 in red. The distribution is clustered around one with a slight shift towards values less than one. To analyze for the cause of the observed changes, the spectral shape and the depth distribution of different time periods of the experiment are compared. To accomplish this, the number of available intervals is sectioned into three parts: the start, middle and end of the lifetime.

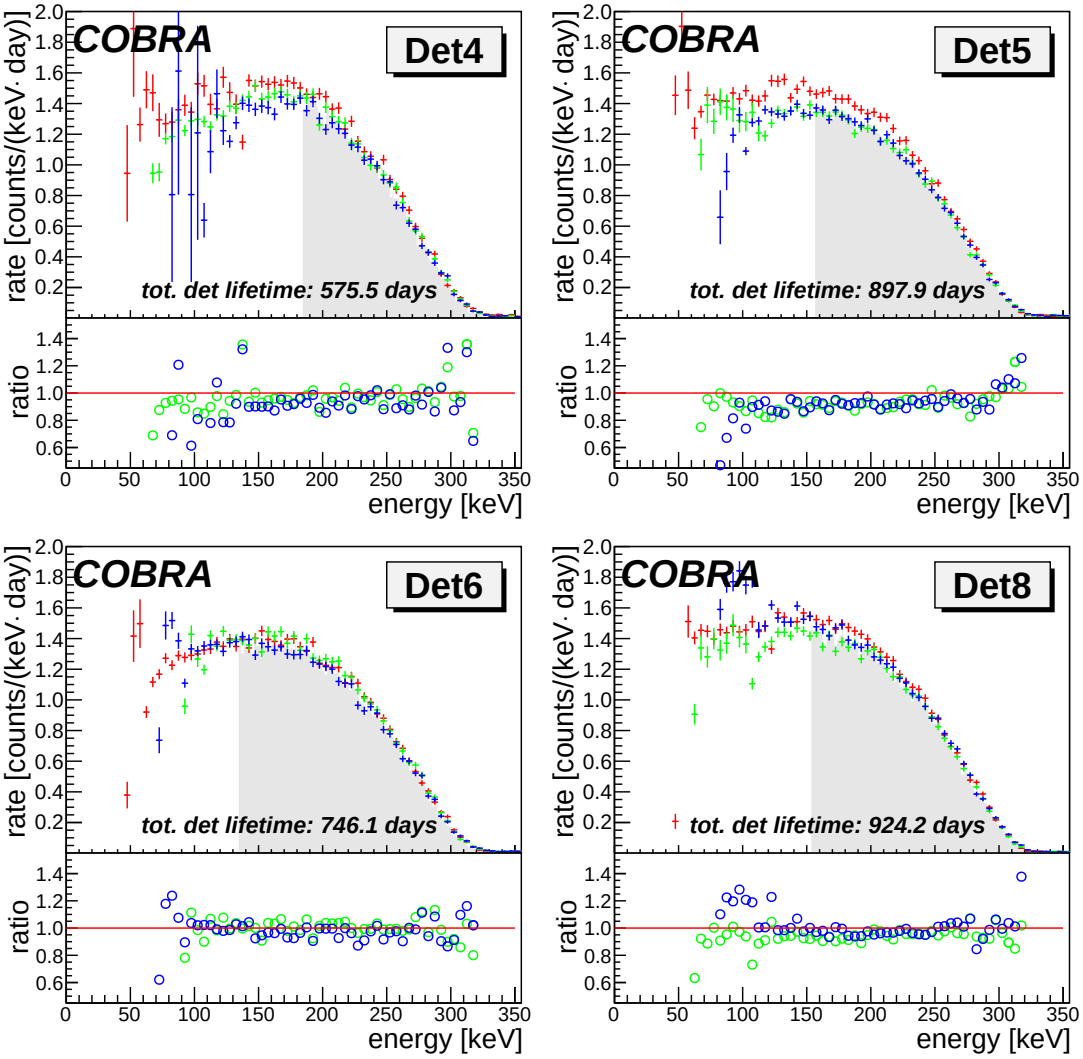

Figure 3.63: Comparison of the spectral shapes of the ^{113}Cd decay for different time sections. The data is partitioned into three time periods: first third (red), second third (green) and last third (blue). The grey part of the spectrum has been used for the stability analysis. The lower inset shows the relative deviation of the middle (green) and the end period (blue) with respect to the start period (red).

For the three time periods, the counts per keV are summed up bin-wise and normalized to the respective lifetime per bin for each detector. In figure 3.63, the three spectra of the detectors are plotted for the first third of the data taking period in red, the second third in green and the last third in blue. In grey, the part of the spectrum that lies above the $(E_{\mathrm{opt}}+20)$ keV is marked. Only this part is used for the stability analysis. In the presented cases the first third of the data taking period lies slightly above the green and blue ones - but no clear tendency is observable if the other detectors are respected.

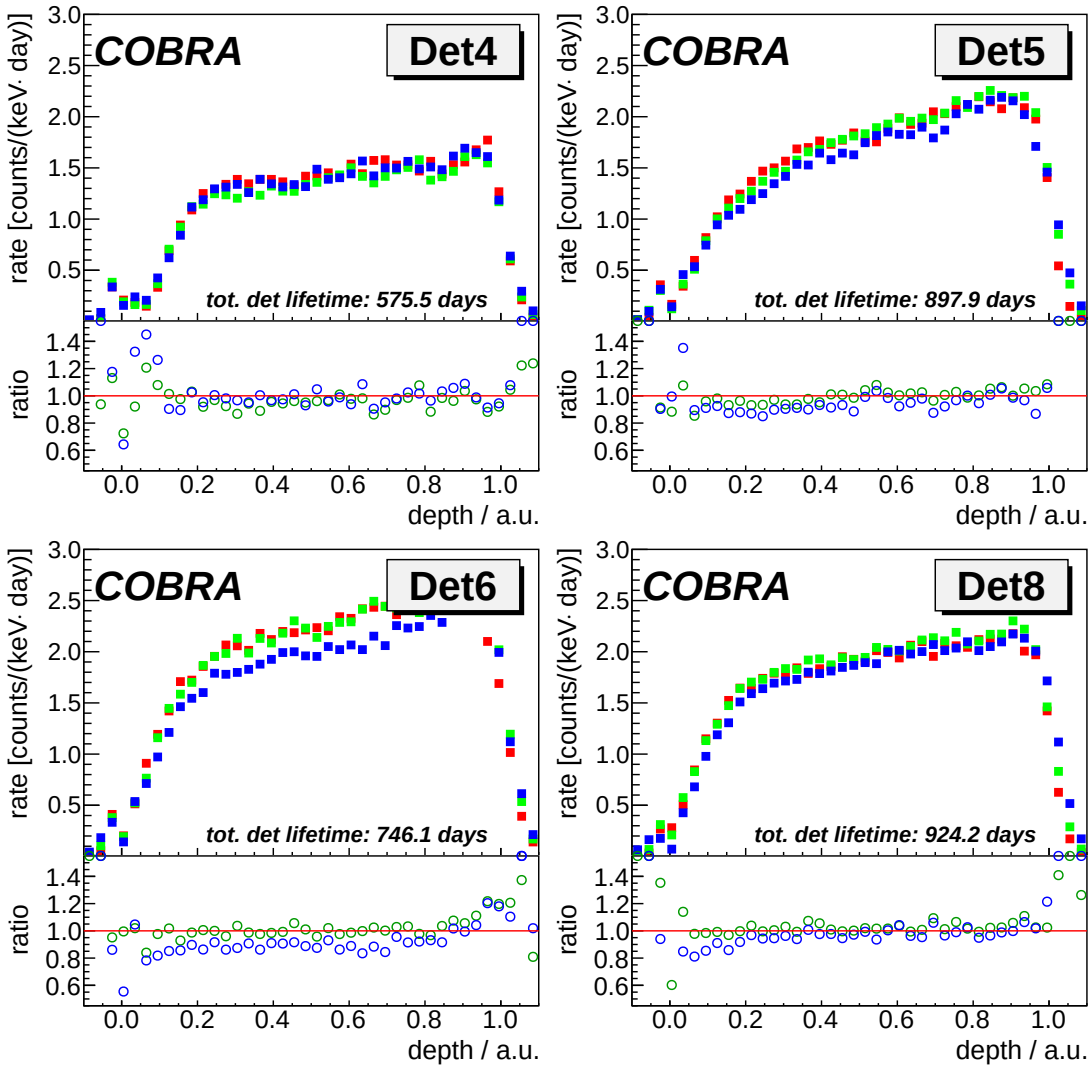

Figure 3.64: Comparison of the depth distribution of the ^{113}Cd decay for different time sections (anodes at '0', cathode at '1'). For the stability analysis the static depth cut is applied.

In general, no shift or deformation of the spectral shape is found comparing the different time periods. For the stability analysis of the reconstructed depth distribution, the same time sectioning and least common energy threshold-cuts are applied. In contrast to the decay-rate based stability analysis that implies the static depth-cut, no depth dependent cuts are applied here. This allows for an analysis of the full depth distribution of the recorded interactions. No time-correlated impact on the reconstructed depth is visible as can be seen in figure 3.64. The fact that the shape of the depth distribution looks different for the single detectors is caused by their different thresholds. The lower the threshold, the higher the total count rate. The asymmetry of the reconstructed depth, which shows a shift of the reconstructed events towards the cathode, is caused by imprecisions of the reconstruction algorithm for lower energies.

3.7.4 Results of the Stability Analysis

The presented stability analysis is based on the intrinsic, fourfold forbidden non-unique single beta-decay of ^{113}Cd with a Q-value of Q=(322.2 ± 1.2) keV. The stability results obtained are limited to the energy range from approximately $E = (100 \ldots 350)$ keV. The analyzed dataset represents a lifetime of roughly $t = 3.5$ yr with a total acquired exposure of $m \cdot t = 218$ kg·days, which is the longest measurement ever taken with CZT detectors under these conditions.
Based on this dataset, count rate variations in the lower percent-per-year range of $\Delta_{mean} = (-0.5 \pm 0.4)$ % per year and are found for 45 out of 48 detectors. The majority of the detectors are working without any glitches or sudden performance changes. The reproduction of the spectral information as well as the depth reconstruction of the detectors is not affected and is stable over the analyzed time period. The 16 detectors of layer L3 are excluded due to known performance issues. Disregarding L3, the overall performance and stability of the setup is excellent. The root cause for the observed minor alterations of the count rate is currently not clear. The stability tracking for the higher energies was not in the scope of this work. To analyze for efficiency alterations in higher energy ranges, a continuous monitoring of the detectors based on precisely positioned calibration sources is required. Nevertheless, under the precondition of ultra low-background operation, the analysis of the intrinsic ^{113}Cd decay offers a unique way to monitor the detector performance during the runtime of the experiment.
Finally, it is concluded that CZT detectors can be operated stably under ultra low-background conditions over time scales of at least several years. This result shows that it is possible to move towards a large-scale experiment as proposed by the COBRA collaboration. The work and the data of this chapter is published in [EGG+16b].

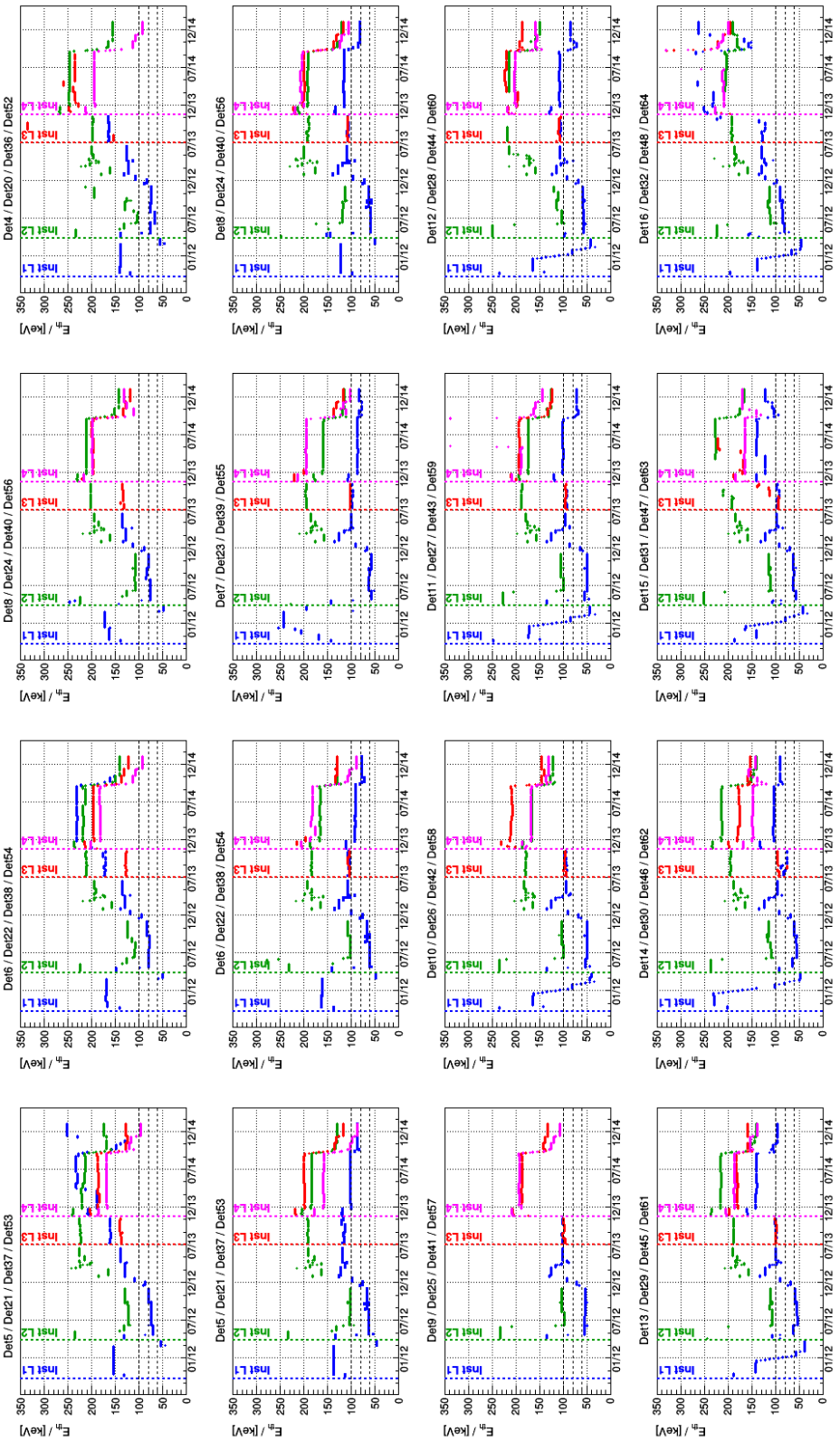

Figure 3.65: The time dependent threshold settings for all detectors. The plot is arranged in the 4x4 array with color coding for the different layers. The installation of Layer L1, L2, L3 and L4 is indicated.

4

Discussion

Within the scope of this work a fully equipped detector characterization laboratory has been established at the TU Dresden and three different test setups were developed. The use of these setups is universally possible and not limited to a specific detector type. The test setups allowed to thoroughly analyze the different specifics of the semiconducting radiation detectors and to perform comprehensive studies of it. The main focus of this work was on the characterization of the CZT detectors used in the COBRA Demonstrator at the LNGS and even if there are just 64 detectors installed, finally more than 100 detectors have been analyzed. In order to enable such extensive measuring campaigns, a suitable infrastructure had to be installed and automatic measuring and evaluation routines had to be developed, accordingly. Furthermore, electronic components had to be used, which are also in use at the LNGS, in order to keep the results transferable.

The first test setup was built to determine the working points, the energy resolution and the detection efficiency of the detectors. In section 3.2 the test setup and the results of this investigation is presented. This approach worked fine for the determination of the working points of the COBRA Demonstrator detectors but it does not scale for a large scale experiment as proposed by the COBRA collaboration as on the one hand the measurements ran automatically but on the other hand the detectors had to be exchanged manually. Therefore, other ways to find the optimal combination of GB and HV per detector are required. One possibility is to perform this analysis at the readily installed detector layers at LNGS. The introduction of a suitable calibration source and the automatic scanning of the GB/HV parameter space combined with an automatic acquisition of the spectrum for the corresponding GB/HV combinations, would allow to perform the above described determination of the working point of the detectors at their final point of deployment. The automatic evaluation procedures to find the working points of the detectors are developed and can be implemented for such an approach, easily. This approach would also allow to overcome the problem, that some of the installed detectors at the LNGS could not be operated at their specific working point as determined at the detector laboratory.

The proposed in-place determination of the working point could easily be combined

with the temperature scaling measurements. As described in section 3.3, the detector performance is temperature dependent. Improvements of the detector performance have been found and it is shown, that the mobility-lifetime product improved with decreasing temperatures. In this work only a single detector was analyzed in the pull parameter space for its spectral response to mild cooling. This is due to the fact, that only one detector at a time can be installed in the cooling box and that the scan of all operational parameters at different temperatures is time-consuming.
The general setup of the COBRA Demonstrator allows to rerun both experiments at once: the working point determination with all 64 detectors installed in place and the analysis of the temperature dependence of the detector performance under real experimental conditions. The basic requirements – a programmable GB/HV power supply, a cooling device to adjust the temperature over a wide range and the possibility to insert a calibration source – are fulfilled, such, that a repetition of the experiment is possible and could be performed from remote. It is suggested, to repeat the experiment with a ^{152}Eu source to allow for an analysis of the temperature driven impact over a wide energy range, as the ^{152}Eu decay offers many suited γ-lines over the full energy spectrum. The analysis of the temperature driven impact on the energy threshold of the different detectors could be performed in parallel, too.
Another challenge was the development of the completely novel test rig to monitor the two dimensional distribution of the charge collection efficiency (CCE) in the COBRA Demonstrator detectors (section 3.4). Initial investigations have been performed at other institutions with α-irradiation of the cathode, only. This already revealed some impressions of local variations of the CCE but with this approach it was not possible to map spatial distributions. The developed 2D scanning test rig allows to map cubic detectors from five sides by means of highly collimated γ-rays. As shown in figures 3.31 and 3.32 the mapping from four sides allows for a back-projection of the local variations of the CCE in the detectors and to gain an impression of the spatial distributions of affected areas. All detectors currently installed at COBRA Demonstrator setup have been scanned at least from two sides. For the overview of the quality of the detector it is sufficient, as the improved method for the reconstruction of the depth of interaction also contributes to the general information. Another major advantage of the 2D scanning test rig is that this device can be used universally and is not limited to CZT analysis. The large scanning range of the linear motors and the micrometer precision make it a great tool for a variety of tasks. Such, it has been used for the development of the evaluation methods for the new 6 cm^3 Quad-Grid detectors that will be used in the COBRA-XDEM setup. The possibility to irradiate very localized and with high accuracy allowed to investigate interactions very close to the inter-grid borders of this new type of detectors. Details of this investigations can be found in appendix B.
The third test setup developed in the course of this work is the compton coincidence experiment (section 3.5). With the help of this device it is possible to select defined single site interaction pulses of specific energy from defined depth of interactions in the detector. The possibility to distinguish single- from multi-site interactions is a must-have for an effective background suppression for $0\nu\beta\beta$-search. The $\beta\beta$-decay is

by origin a single site interaction and, hence, events with the searched energy deposition but multiple points of interaction in the same detector have to be discarded. Such events can be caused by high energetic photons that undergo multiple compton scatter processes in the same detector. The best way to generate a defined library of single site events is to make use of the compton scatter process itself as a singly scattered photon is by definition a single site event and the scattered photon carries a defined energy at a defined scatter angle. The detection of this photon allows to tag the primary interaction as a single site event and the reconstruction algorithm allows to identify the plane of the depth of interaction in the detector. Therefore, the test setup was designed with a COBRA Demonstrator detector as the scattering detector and the HPGe detector as the second detector. Again, the setup was designed to be used with different radioactive sources, such, that the searched events can be generated over a wide range of energy. The moveable primary collimator for the radioactive source allowed to adjust the irradiation intensity according to the maximal event rate the data acquisition system can handle. The goniometer was designed with the CZT detector in the pivot of the setup, the moveable source at the rotatable arm and the HPGe detector at an adjustable scatter angle (figure 3.36). To suppress the normal laboratory background and to enhance the detection of the scattered photons, accordingly, a special lead shielding for the HPGe detector was developed that improved the background rate by nearly an order of magnitude over the full energy range. The result of this measurements is a library of defined single site interactions of different energies at different depth of interactions. Furthermore, the experiments performed at this setup allowed to improve the identification algorithm for multiple interactions in the detectors significantly and, hence, improved the background suppression power for the $0\nu\beta\beta$-search.
Beside high energetic photons, α-particles from natural radioactive decay also generate background in the current COBRA Demonstrator. This rose questions if a separation of α-particles from β-particles based on pulse shape analysis is possible. To analyze this question, dedicated experiments were performed (section 3.6). Experimental conditions were chosen such, that the difference of the α- and β-interactions would be the largest possible. That was achieved by an irradiation of the cathode side of the detector with the respective sources. The use of a combined α-source at different distances allowed to analyze the impact of different energies up to 5 MeV. In the absence of a source with a natural β-decay energy higher than 2 MeV this experiment was capped for the β-irradiation at this energy. The analysis for a possible differentiation of the α- and β-events was performed at different parameters of the pulse. Therefore, the pulse up-slope and the drift time of the events was analyzed for a variety of signals. The differences found for both interactions are only visible in the DIFF and DIFF-DERIVATIVE signal close to the splitting point of the CA and NCA signal. Unfortunately, the observed differences are too small to be used as a differentiating feature to decide this interaction was an α- or a β-interaction. The differences became visible only in the accumulated spectra with large numbers of events and the observed deviations were below the nominal resolution of the FADCs for a single event. Hence, the approach to distinguish α- from β-events based on pulse shape analysis, only, is not applicable. Investigations

performed by multi-variant analysis have shown to be more promising, but also here the differentiation of α- and β-interactions is not as strong as needed [Reb15].
A large scale a $0\nu\beta\beta$-experiment has to be operated for several years. Therefore, the long term stability of the used detectors must be assured and a measure to keep track of it must be found. To probe, if the COBRA Demonstrator detectors fulfill the required long-term stability, the largest data-set ever acquired with CZT detectors at this time was analyzed (section 3.7). The analysis was performed with data of the fully equipped COBRA Demonstrator in its final shape. Due to the stepwise upgrade of the experiment, different total life-times of the four layers are analyzed, ranging from roughly 3.5 years for Layer1 to about 1 year for Layer4. The analysis was performed based on the fourfold forbidden, non-unique single β-decay of ^{113}Cd with a half-life of $T_{1/2} = 8 \cdot 10^{15}$ yr. Even though this isotope has such a long half-life it was the only suited signal for the stability analysis as it is an intrinsic component of the CZT detectors and it is evenly distributed in the source material. Therefore, no external stimulation was needed and the analysis can be performed on the normal data taking runs. ^{113}Cd generates about 150 decays per day in a detector over the full energy spectrum with about 1.4 counts per keV and day in the most intense part of the β-spectrum. The low count rate and the steadily changing energy thresholds required to develop a figure of merit that was used to select runs for the analysis that yielded best statistical data. It was found, that the count rate change of 45 out of 48 detectors was in the lower percent-per-year range and the majority of the detectors worked without any glitches or sudden performance changes. The spectral shape reproduction was stable and there were no changes in the reconstructed depth of interaction observable. These results are a great success for the COBRA collaboration as it shows that long term operation of CZT detectors with no performance degradation is generally possible.

Public presentations in the course of this work

- D. Gehre on behalf of the COBRA collaboration
  On the Use of CPG-CZT Detectors in the COBRA Experiment
  IEEE, 2010 Nuclear Science Symposium and Medical Imaging Conference

- D. Gehre on behalf of the COBRA collaboration
  Spatial resolved determination of the weighting factor on CZT-CPG detectors
  IEEE, 2011 Nuclear Science Symposium and Medical Imaging Conference

- D. Gehre on behalf of the COBRA collaboration
  Long Term Stability and Depth of Interaction Studies on Underground Operated CZT-CPG Detectors
  IEEE, 2012 Nuclear Science Symposium and Medical Imaging Conference

- D. Gehre on behalf K. Zuber
  On the Search for the Neutrinoless Double Beta Decay with the COBRA-Experiment
  Scientific Committee Meeting at LNGS, 2013

- D. Gehre on behalf of the COBRA collaboration
  Investigations on the Long-Term Stability of Underground Operated CZT-Detectors Based on the ^{113}Cd-Decay Analysis
  IEEE, 2014 Nuclear Science Symposium and Medical Imaging Conference

- D. Gehre on behalf of the COBRA collaboration
  A Compton Scatter Experiment for the Discrimination of Single-Site and Multi-Site Events in CZT-CPG-Detectors
  IEEE, 2014 Nuclear Science Symposium and Medical Imaging Conference

- D. Gehre and M.-L. Menzel
  Analyse der charakteristischen Eigenschaften des CZT-CPG-Detektors unter Gamma- und Neutronen-Strahlung
  DPG-Frühjahrstagung 2010, Physik der Hadronen und Kerne

- D. Gehre und A. Sörensen
  Ortsaufgelöste Bestimmung der Detektor-Effizienz an COBRA-CZT-CPG Detektoren
  DPG-Frühjahrstagung 2011, Physik der Hadronen und Kerne

- D. Gehre on behalf of the COBRA collaboration
  Status des Doppel-Beta-Experiments C0BRA - Gruppenbericht
  DPG-Frühjahrstagung 2012, Physik der Hadronen und Kerne

- D. Gehre und M. Fritts
  Long Term Stability Study on Underground Operated CZT-CPG Detectors
  DPG-Frühjahrstagung 2013, Physik der Hadronen und Kerne

Publications in the course of this work

- J. Ebert, ..., D. Gehre, et. al
  Results of a search for neutrinoless $\beta\beta$-decay using the COBRA Demonstrator,
  Physical Review C 94 (2016) no.2, 024603

- J. Ebert, ..., D. Gehre, et. al
  Long-term stability of underground operated CZT detectors based on the analysis of intrinsic ^{113}Cd β-decay,
  Nuclear Instruments and Methods in Physics Research Section A: Accelerators, Spectrometers, Detectors and Associated Equipment, A821 (2016) 109-115

- J. Ebert, ..., D. Gehre, et. al
  The COBRA Demonstrator at the LNGS underground laboratory,
  Nuclear Instruments and Methods in Physics Research Section A: Accelerators, Spectrometers, Detectors and Associated Equipment, A807 (2016) 114-120

- J. Ebert, ..., D. Gehre, et. al
  Characterization of a large CdZnTe coplanar quad-grid semiconductor detector,
  Nuclear Instruments and Methods in Physics Research Section A: Accelerators, Spectrometers, Detectors and Associated Equipment, A806 (2016) 159-168

- J. Ebert, ..., D. Gehre, et. al
  Pulse-shape discrimination of surface events in CdZnTe detectors for the COBRA experiment,
  Nuclear Instruments and Methods in Physics Research Section A: Accelerators, Spectrometers, Detectors and Associated Equipment, A749 (2014) 27-34

- J. Ebert, ..., D. Gehre, et. al
  Current Status and Future Perspectives of the COBRA Experiment,
  Advances in High Energy Physics Volume 2013 (2013), Article ID 703572

Bibliography

[A+02] Q. R. Ahmad et al. Direct evidence for neutrino flavor transformation from neutral-current interactions in the sudbury neutrino observatory. *Phys. Rev. Lett.*, 89(1):011301, 2002. 6

[A+12] M. Auger et al. Search for neutrinoless double-beta decay in ^{136}Xe with exo-200. *Phys. Rev. Lett.*, 109:032505, Jul 2012. 11

[A+16a] C. Alduino et al. Analysis techniques for the evaluation of the neutrinoless double-β decay lifetime in ^{130}Te with the cuore-0 detector. *Phys. Rev. C*, 93:045503, 2016. 3, 11, 13

[A+16b] R. Arnold et al. Measurement of the 2 decay half-life and search for the 0 decay of ^{116}cd with the nemo-3 detector. *arXiv:1610.03226v2*, 2016. 11

[AAB+16] M. Agostini, M. Allardt, A.M. Bakalyarov, M. Balata, I. Barabanov, L. Baudis, C. Bauer, N. Becerici-Schmidt, E. Bellotti, S. Belogurov, S.T. Belyaev, G. Benato, A. Bettini, L. Bezrukov, T. Bode, D. Borowicz, V. Brudanin, R. Brugnera, D. Budjáš, A. Caldwell, C. Cattadori, A. Chernogorov, V. D'Andrea, E.V. Demidova, A. Domula, E. Doroshkevich, V. Egorov, R. Falkenstein, O. Fedorova, K. Freund, N. Frodyma, A. Gangapshev, A. Garfagnini, C. Gooch, C. Gotti, P. Grabmayr, V. Gurentsov, K. Gusev, W. Hampel, A. Hegai, M. Heisel, S. Hemmer, G. Heusser, W. Hoffmann, M. Hult, L.V. Inzhechik, L. Ioannucci, J. Janicksó Csáthy, J. Jochum, M. Junker, V. Kazalov, T. Kihm, I.V. Kirpichnikov, A. Kirsch, A. Klimenko, K.T. Knöpfle, O. Kochetov, V.N. Kornoukhov, V.V. Kuzminov, M. Laubenstein, A. Lazzaro, V.I. Lebedev,

B. Lehnert, H.Y. Liao, M. Lindner, I. Lippi, A. Lubashevskiy, B. Lubsandorzhiev, G. Lutter, C. Macolino, B. Majorovits, W. Maneschg, G. Marissens, E. Medinaceli, M. Misiaszek, P. Moseev, I. Nemchenok, S. Nisi, D. Palioselitis, K. Panas, L. Pandola, K. Pelczar, G. Pessina, A. Pullia, M. Reissfelder, S. Riboldi, N. Rumyantseva, C. Sada, M. Salathe, C. Schmitt, B. Schneider, J. Schreiner, O. Schulz, B. Schwingenheuer, S. Schönert, H. Seitz, O. Selivalenko, E. Shevchik, M. Shirchenko, H. Simgen, A. Smolnikov, L. Stanco, M. Stepaniuk, H. Strecker, C.A. Ur, L. Vanhoefer, A.A. Vasenko, A. Veresnikova, K. von Sturm, V. Wagner, M. Walter, A. Wegmann, T. Wester, C. Wiesinger, H. Wilsenach, M. Wojcik, E. Yanovich, P. Zavarise, I. Zhitnikov, S.V. Zhukov, D. Zinatulina, K. Zuber, and G. Zuzel. Search of neutrinoless double beta decay with the gerda experiment. *Nuclear and Particle Physics Proceedings*, 273:1876 – 1882, 2016. 37th International Conference on High Energy Physics (ICHEP). 3

[ALL02] Mark Amman, Julie S. Lee, and Paul N. Luke. Electron trapping nonuniformity in high-pressure-bridgman-grown cdznte. *Journal of Applied Physics*, 92(6):3198–3206, 2002. 53

[ALL06] M. Amman, J. S. Lee, and P. N. Luke. Temperature Study of CdZnTe Coplanar-Grid Detectors. *IEEE Transactions on Nuclear Science*, 53(5):3035–3040, Oct 2006. 43, 123

[AMC+10] S.A. Awadalla, J. Mackenzie, H. Chen, B. Redden, G. Bindley, M.C. Duff, A. Burger, M. Groza, V. Buliga, J.P. Bradley, Z.R. Dai, N. Teslich, and D.R. Black. Characterization of detector-grade cdznte crystals grown by traveling heater method (thm). *Journal of Crystal Growth*, 312(4):507 – 513, 2010. 17

[Arl17] M. Gerhardt C. G"ossling D. Gehre R. Klingenberg K. Kr"oninger C. Nitsch T. Quante K. Rohatsch J. Tebr"ugge R. Temminghoff R. Theinert S. Zatschler K. Zuber J.H. Arling. Suppression of alpha-induced lateral surface events in the cobra experiment using cdznte detectors with an instrumented guard-ring electrode. *arXiv*, Prepared for submission to JINST, 2017. 137

[AZM67] W. Akutagawa, K. Zanio, and J.W. Mayer. Cdte as a gamma detector. *Nuclear Instruments and Methods*, 55:383 – 385, 1967. 4

[Bar15] A. S. Barabash. Average and recommended half-life values for two neutrino double beta decay. *Nucl. Phys.*, 935:52–64, 2015. 9

[BBB+12] G. Bellini, J. Benziger, D. Bick, G. Bonfini, D. Bravo, M. Buizza Avanzini, B. Caccianiga, L. Cadonati, F. Calaprice, C. Carraro, P. Cavalcante, A. Chavarria, A. Chepurnov, D. D'Angelo, S. Davini, A. Derbin, A. Etenko, F. von Feilitzsch, K. Fomenko, D. Franco, C. Galbiati, S. Gazzana, C. Ghiano, M. Giammarchi, M. Goeger-Neff, A. Goretti, L. Grandi, E. Guardincerri, C. Hagner, S. Hardy, Aldo Ianni, Andrea Ianni, D. Korablev, G. Korga, Y. Koshio, D. Kryn, M. Laubenstein, T. Lewke, E. Litvinovich, B. Loer, F. Lombardi, P. Lombardi, L. Ludhova, I. Machulin, S. Manecki, W. Maneschg, G. Manuzio, Q. Meindl, E. Meroni, L. Miramonti, M. Misiaszek, D. Montanari, P. Mosteiro, V. Muratova, L. Oberauer, M. Obolensky, F. Ortica, K. Otis, M. Pallavicini, L. Papp, L. Perasso, S. Perasso, A. Pocar, R.S. Raghavan, G. Ranucci, A. Razeto, A. Re, A. Romani, A. Sabelnikov, R. Saldanha, C. Salvo, S. Schönert, H. Simgen, M. Skorokhvatov, O. Smirnov, A. Sotnikov, S. Sukhotin, Y. Suvorov, R. Tartaglia, G. Testera, D. Vignaud, R.B. Vogelaar, J. Winter, M. Wojcik, A. Wright, M. Wurm, J. Xu, O. Zaimidoroga, S. Zavatarelli, and G. Zuzel. Cosmic-muon flux and annual modulation in borexino at 3800 m water-equivalent depth. *Journal of Cosmology and Astroparticle Physics*, 2012(05):015, 2012. 114

[BBC+09] P. Belli, R. Bernabei, F. Cappella, R. Cerulli, F.A. Danevich, B.V. Grinyov, A. Incicchitti, V.V. Kobychev, V.M. Mokina, S.S. Nagorny, L.L. Nagornaya, S. Nisi, F. Nozzoli, D.V. Poda, D. Prosperi, V.I. Tretyak, and S.S. Yurchenko. Search for double beta decay of zinc and tungsten with low background znwo4 crystal scintillators. *Nuclear Physics A*, 826(3):256 – 273, 2009. 13

[BBD+07] T. Bloxham, A. Boston, J. Dawson, D. Dobos, S. P. Fox, M. Freer, B. R. Fulton, C. Gößling, P. F. Harrison, M. Junker, H. Kiel, J. McGrath,

B. Morgan, D. Münstermann, P. Nolan, S. Oehl, Y. Ramachers, C. Reeve, D. Stewart, R. Wadsworth, J. R. Wilson, and K. Zuber. First results on double β-decay modes of cd, te, and zn isotopes. *Phys. Rev. C*, 76:025501, Aug 2007. 115

[BCH49] O. Bunemann, T.E. Cranshaw, and J.A. Harvey. Design of Grid Ionization Chambers. *Canadian Journal of Research*, 27:191–206, 1949. 18

[BDLA93] J.F. Butler, F.P. Doty, C. Lingren, and B. Apotovsky. Cadmium Zinc Telluride Detectors for Industrial Radiation Measurement. *Applied Radiation and Isotopes*, 44(10/11):1359–1366, 1993. 17

[Bea07] P. Belli and et al. Investigation of β decay of ^{113}Cd. *Phys. Rev. C*, 76:64603/1 – 64603/10, 2007. `http://link.aps.org/doi/10.1103/PhysRevC.76.064603`. 81

[BGS+17] Mihály Braun, Yordan M. Georgiev, Tommy Schönherr, Heinrich Wilsenach, and Kai Zuber. A new precision measurement of the -decay half-life of 190pt. *Physics Letters B*, 768(Supplement C):317 – 320, 2017. 69

[BV92] F. Boehm and P. Vogel. *Physics of Massive Neutrinos*. Cambridge University Press, 1992. 6, 9

[Cen18] National Nuclear Data Center. Nuclide Chart NNDC, 2018. 71

[Col17] The GERDA Collaboration. Background-free search for neutrinoless double-decay of 76ge with gerda. *Nature*, 544(7648):47–52, 04 2017. 2, 11

[Cre17] Inc Cremat. Cr-110 charge sensitive preamplifier. *http://www.cremat.com/CR-110.pdf*, Feb. 2017. 126

[Cro04] J. Crocco. Influence of dynamic temperature adjustments during growth on the material properties of CZT radiation devices. *Journal of Crystal Growth*, 361:66–72, 2004. 17

[CVH+09] V. Carcelen, N. Vijayan, P. Hidalgo, J. Rodriguez-Fernandez, J. Piqueras, N.V. Sochinskii, J.M. Perez, and E. Dieguez. Influence of thermal environments on the growth of bulk cadmium zinc telluride (CZT) single crystals. *Journal of Crystal Growth*, 311:264–1267, 2009. 17

[CZT93] Proceedings of material research society symposium. In P. Siffert R. B. James, T. E. Schlesinger and L. Franks, editors, *Semiconductors for Room-Temperature Radiation Detector Applications*, volume 302. Materials Research Society, Pittsburgh, PA, 1993. 4

[DGJ+09] J. V. Dawson, C. Goessling, B. Janutta, M. Junker, T. Koettig, D. Muenstermann, S. Rajek, C. Reeve, O. Schulz, J. R. Wilson, and K. Zuber. Experimental study of double-β decay modes using a cdznte detector array. *Phys. Rev. C*, 80:025502, Aug 2009. 115

[DMR+09] J.V. Dawson, C. Montag, C. Reeve, J.R. Wilson, and K. Zuber. An Investigation on Cooling of CZT Co-Planar Grid Detectors. *Nuclear Instruments and Methods in Physics Research Section A: Accelerators, Spectrometers, Detectors and Associated Equipment*, 599(2–3):209 – 214, 2009. 43, 123

[Do16] F A Danevich and other. Search for double beta decay of 116 cd with enriched 116 cdwo 4 crystal scintillators (aurora experiment). *Journal of Physics: Conference Series*, 718(6):062009, 2016. 11

[DRW+09] J.V. Dawson, C. Reeve, J.R. Wilson, K. Zuber, M. Junker, C. Gössling, T. Köttig, D. Münstermann, S. Rajek, and O. Schulz. An investigation into the 113cd beta decay spectrum using a cdznte array. *Nuclear Physics A*, 818(3):264 – 278, 2009. 81, 115

[DRZ11] A. Dueck, W. Rodejohann, and K. Zuber. Neutrinoless double beta decay, the inverted hierarchy and precision determination of teta12. *Physics Review D*, 83, 2011. 10

[EFG+16] J. Ebert, M. Fritts, D. Gehre, C. Gößling, C. Hagner, N. Heidrich, R. Klingenberg, K. Kröninger, C. Nitsch, C. Oldorf, T. Quante, S. Rajek, H. Rebber, K. Rohatsch, J. Tebrügge, R. Temminghoff, R. Theinert, J. Timm, B. Wonsak, S. Zatschler, and K. Zuber. Results of a search for neutrinoless double-β decay using the cobra demonstrator. *Phys. Rev. C*, 94:024603, Aug 2016. 11, 16

[EGG+11] J. Esterline, V.M. Gehman, K. Gusey, T. Hossbach, R.A. Johnson, K. Kazkaz, J. Kephart, M. Kidd, G. King, M.G. Marino, A.G. Schubert,

M. Shirchenko, J. Thompson, V. Timkin, and B. White. The majorana experiment. *Nuclear Physics B - Proceedings Supplements*, 221:364, 2011. The Proceedings of the 22nd International Conference on Neutrino Physics and Astrophysics. 3

[EGG+16a] J. Ebert, D. Gehre, C. Gößling, C. Hagner, N. Heidrich, R. Klingenberg, K. Kröninger, C. Nitsch, C. Oldorf, T. Quante, S. Rajek, H. Rebber, K. Rohatsch, J. Tebrügge, R. Temminghoff, R. Theinert, J. Timm, B. Wonsak, S. Zatschler, and K. Zuber. Characterization of a large cdznte coplanar quad-grid semiconductor detector. *Nuclear Instruments and Methods in Physics Research Section A: Accelerators, Spectrometers, Detectors and Associated Equipment*, 806:159 – 168, 2016. 15

[EGG+16b] J. Ebert, C. Gößling, D. Gehre, C. Hagner, N. Heidrich, R. Klingenberg, K. Kröninger, C. Nitsch, C. Oldorf, T. Quante, S. Rajek, H. Rebber, K. Rohatsch, J. Tebrügge, R. Temminghoff, R. Theinert, J. Timm, B. Wonsak, S. Zatschler, and K. Zuber. Long-term stability of underground operated czt detectors based on the analysis of intrinsic 113cd -decay. *Nuclear Instruments and Methods in Physics Research Section A: Accelerators, Spectrometers, Detectors and Associated Equipment*, 821:109 – 115, 2016. 90

[EHM87] S. R. Elliott, A. A. Hahn, and M.K. Moe. Direct evidence for two- neutrino double-beta decay in 82se. *Phys. Rev. Lett.*, 59:2020–2023, 1987. 9

[Ein15] Albert Einstein. Erklärung der perihelbewegung des merkur aus der allgemeinen relativitätstheorie. Technical Report S. 225–261, Sitzungsberichte der Preußischen Akademie der Wissenschaften, 1915. 1

[FBC96] Richard B. Firestone, C. Baglin, and S. Y. Frank Chu. *Table of Isotopes*. John Wiley & Sons, 1996. 8, 13, 68

[Fea13] M. Fritts and et al. Analytical model for event reconstruction in coplanar grid CdZnTe detectors. *Nucl. Instr. Meth. A*, 708:1 – 6, 2013. `http://arxiv.org/abs/1211.6604`. 19, 20, 22, 49, 84

[Fea14] M. Fritts and et al. Pulse-shape discrimination of surface events in CdZnTe detectors for the COBRA experiment. *Nucl. Instr. Meth. A*, 749:27–34, 2014. `http://arxiv.org/abs/1401.5844v1`. 26, 84

[Fuk98] Y. et al Fukuda. Evidence for oscillation of atmospheric neutrinos. *PhysRevLett*, 81(8):1562–1567, 1998. 6

[Fur39] W.H. Furry. On transition probabilities in double beta-disintegration. *Physical Review*, 56:1184–1193, 1939. 9

[G+17] G.Audi et al. The ame2012 atomic mass evaluation (i). *http://amdc.impcas.ac.cn/evaluation/data2012/data/mass.mas12*, Jan 2017. 13

[Gan12] Azusa Gando. Results from KamLAND-Zen. In *Proceedings, 4th International Conference Current Problems in Nuclear Physics and Atomic Energy (NPAE-2012): Kyiv, Ukraine, September 3-7, 2012*, pages 386–389, 2012. 11

[GHMT06] Ariel Goobar, Steen Hannestad, Edvard Mörtsell, and Huitzu Tu. The neutrino mass bound from wmap 3 year data, the baryon acoustic peak, the snls supernovae and the lyman- forest. *Journal of Cosmology and Astroparticle Physics*, 2006(06):019, 2006. 2

[GJK+05] C. Goessling, M. Junker, H. Kiel, D. Muenstermann, S. Oehl, and K. Zuber. Experimental study of ^{113}cd β decay using cdznte detectors. *Phys. Rev. C*, 72:064328, Dec 2005. 115

[GM35] M. Goeppert-Mayer. Double beta-disintegration. *Physical Review*, 48.6:512–516, 1935. 8

[KHBM10] Alireza Kargar, Mark J. Harrison, Adam C. Brooks, and Douglas S. McGregor. Characterization of charge carrier collection in a cdznte frisch collar detector with a highly collimated source. *Nuclear Instruments and Methods in Physics Research Section A: Accelerators, Spectrometers, Detectors and Associated Equipment*, 620(2–3):270 – 278, 2010. 53

BIBLIOGRAPHY

[KKDB+01] H.V. Klapdor-Kleingrothaus, A. Dietz, L. Baudis, G. Heusser, I.V. Krivosheina, B. Majorovits, H. Paes, H. Strecker, V. Alexeev, A. Balysh, A. Bakalyarov, S.T. Belyaev, V.I. Lebedev, and S. Zhukov. Latest results from the heidelberg-moscow double beta decay experiment. *The European Physical Journal A - Hadrons and Nuclei*, 12(2):147–154, 2001. 2, 115

[KMZ03] H. Kiel, D. Münstermann, and K. Zuber. A search for various double beta decay modes of cd, te, and zn isotopes. *Nuclear Physics A*, 723(3–4):499 – 514, 2003. 115

[Kno00] G. F. Knoll. *Radiation Detection and Measurement.* John Wiley & Sons, 2000. 16

[Köt12] T. Köttig. *Sensitivity Studies of CdZnTe Semiconductor Detectors for the COBRA Experiment.* PhD thesis, TU Dortmund, 2012. 10, 14

[KP93] C.W. Kim and A. Pevsner. *Neutrinos in Physics and Astrophysics.* Harwood Academic Publishers, 1993. 6

[Kre17] Tom Kresse. Investigation of the temperature behavior of cdznte room temperature semiconductor detectors for the c0bra experiment. Master's thesis, TU Dresden, 2017. 46, 51

[Leo92] W. R. Leo. *Techniques for Nuclear and Particle Physics Experiments.* Springer Verlag, 1992. 16

[Luk94] P.N. Luke. Single-polarity charge sensing in ionization detectors using coplanar electrodes. *Appl. Phys. Lett.*, 65:2884–2886, 1994. 18

[Mea06] M. Mustonen and et al. Theoretical description of the fourth-forbidden non-unique decays of ^{113}Cd and ^{115}In. *Phys. Rev. C*, 73:054301/1 – 054301/9, 2006. `http://dx.doi.org/10.1103/PhysRevC.73.054301`. 81

[Mea07] M. Mustonen and et al. Microscopic quasiparticle–phonon description of beta decays of ^{113}Cd and ^{115}In using proton-neutron phonons. *Phys. Lett. B*, 657:38–42, 2007. `http://dx.doi.org/10.1016/j.physletb.2007.09.037`. 81

[Mir05] Lino Miramonti. European underground laboratories: An overview. *arXiv*, 2005. https://arxiv.org/abs/hep-ex/0503054. 114

[MNS62] Z. Maki, M. Nakagawa, and S. Sakata. Remarks on the unified model of elementary particles. *Progress of Theoretical Physics*, 28.5(870-880), 1962. 6

[Mue07] Daniel Muenstermann. *PhD*. PhD thesis, Universität Dortmund, 2007. 12, 18, 21

[New87] Isaac Newton. *Philosophiae Naturalis Principia Mathematica*. 1687. 1

[Nip04] G.D. Nipan. p–T–x–y phase diagram of the CdZnTe system. *Journal of Alloys and Compounds*, 371:160–163, 2004. 17

[Pau30] W. Pauli. *Liebe Radioaktive Damen und Herren!* Open letter to the group of *Radioactive People* at the Gauverein meeting in Tübingen, Dec 1930. 5

[PDB+05] B. Pelliciari, F. Dierre, D. Brellier, L. Verger, F. Glasser, and B. Schaub. A new growth method for CdTe: A breakthrough toward large areas. *Journal of Electronic Materials*, 34:693–698, 2005. 17

[Pon57] B. Pontecorvo. Mesonium and anti-mesonium. *Soviet Physics JETP*, 6:429, 1957. 6

[Ram39] S. Ramo. Currents Induced by Electron Motion. *Proceedings of the I.R.E.*, 27:584–585, 1939. 18

[RC56] F. Reines and C.L. Cowan. The neutrino. *Nature*, 178:446, 1956. 5

[Reb15] Henning Rebber. Discrimination of alpha particles in cdzete detectors with coplanar grid. Master's thesis, Universität Hamburg, 2015. 96

[REE+11] S. Rahaman, V.-V. Elomaa, T. Eronen, J. Hakala, A. Jokinen, A. Kankainen, J. Rissanen, J. Suhonen, C. Weber, and J. Äystö. Double-beta decay Q-values of ^{116}Cd and ^{130}Te. *Physics Letters B*, 703(4):412 – 416, 2011. 13

BIBLIOGRAPHY

[Roh16] Katja Rohatsch. Charakterisierung von großvolumigen cdznte-detektoren mit segmentierter cpg-anodenkonfiguration fuer das cobra-experiment. Master's thesis, TU Dresden, 2016. 135, 137

[S+09] N. D. Scielzo et al. Double-beta decay Q-values of ^{130}Te, ^{128}Te, and ^{120}Te. *https://arxiv.org/abs/0902.2376*, 2009. 13

[S+12] C. Smorra et al. Direct mass measurements of cadmium and palladium isotopes and their double-beta transition q-values. *https://arxiv.org/abs/1201.4942*, 2012. 13

[Sch97] N. Schmitz. *Neutrinophysik*. Teubner, Stuttgart, 1997. 6, 9

[Seg16] Laura Segui. The sno+ project. *Nuclear and Particle Physics Proceedings*, 273:2654 – 2656, 2016. 37th International Conference on High Energy Physics (ICHEP). 3, 13

[STY+01] T.E. Schlesinger, J.E. Toney, H. Yoon, E.Y. Lee, B.A. Brunett, L. Franks, and R.B. James. Cadmium Zinc Telluride Detectors for Industrial Radiation Measurement. *Materials Science and Engineering*, 32:103–189, 2001. 17, 52

[The17] R. Theinert. Characterization of a large cdznte detector with a coplanar quad-grid design. *Nuclear Instruments and Methods in Physics Research Section A: Accelerators, Spectrometers, Detectors and Associated Equipment*, 845:181 – 184, 2017. Proceedings of the Vienna Conference on Instrumentation 2016. 137

[Wes12] Thomas Wester. Characterization of CdZnTe Coplanar Grid Detectors and Pulse Shape Analysis for the C0BRA Experiment. Master's thesis, TU Dresden, 2012. 37, 55

[WJRvF04] H. Wulandari, J. Jochum, W. Rau, and F. von Feilitzsch. Neutron flux at the Gran Sasso underground laboratory revisited. *Astroparticle Physics*, 22:313–322, 2004. 114, 115

[Zat14] Stefan Zatschler. Identification of multi-site events in coplanar-grid cdznte-detectors for the cobra-experiment. Master's thesis, TU Dresden, 2014. 16, 24, 26, 36, 53, 61, 63, 66

[Zub01] K. Zuber. Cobra: Double beta decay searches using CdTe detectors. *Phys.Lett.B*, 519:1–7, 2001. http://arxiv.org/abs/nucl-ex/0105018. 4, 12, 115

[Zub11] K. Zuber. *Neutrino Physics*. CRC Press, Taylor und Francis Group, 2011. 6, 9, 10

Declaration

Die vorliegende Dissertationsarbeit wurde unter wissenschaftlicher Betreuung von Herrn Prof. Dr. Kai Zuber, Institut für Kern- und Teilchenphysik der Technischen Universität Dresden, im Zeitraum von Oktober 2009 bis September 2015 durchgeführt.

Hiermit versichere ich, dass ich die vorliegende Arbeit ohne unzulässige Hilfe Dritter und ohne Benutzung anderer als der angegebenen Hilfsmittel angefertigt habe; die aus fremden Quellen direkt oder indirekt übernommenen Gedanken sind als solche kenntlich gemacht. Die Arbeit wurde bisher weder im Inland noch im Ausland in gleicher oder ähnlicher Form einer anderen Prüfungsbehörde vorgelegt.

Weiterhin bestätige ich hiermit, dass ich die Promotionsordnung der TU Dresden vom 23. Februar 2011 anerkenne.

Daniel Gehre
Dresden, Dezember 2017

Acknowledgements

First of all, I would like to thank Prof. Dr. Kai Zuber for giving me the opportunity to conduct this work. It was a great pleasure to manage the build up of the detector laboratory, to analyze the detectors and support the installation and operation of the COBRA Demonstrator setup at the LNGS in Italy.
Special thanks go to Stefan Zatschler for the fruitful discussions, the trouble shootings and for the continuous support with his programming skills. Stefan had a big share on the success of the build up of the laboratory, the detector investigations and the experiment in Italy.
The setup and the operation of the COBRA Demonstrator would not have been possible without the tremendous amount of work performed from our colleagues at Technische Universität Dortmund. It was a great honor to work with Prof. Dr. Claus Gößling and the group around him.
Further thanks go to Privatdozent Dr. Jürgen Henniger, who taught me all the radiation protection skills I needed to test the detectors and to operate the TU Dresden Neutron-Generator at the Research Center Dresden-Rossendorf. He was a continuous supporter in all questions concerning radiation safety and the administration at the TU Dresden.
And – last but not least – warm thanks go to my wife Kerstin for her enduring support, her patience and for her encouragement to finish this work.

Appendix A

The Experimental Setup of the COBRA Demonstrator

A.1 The Laboratori Nazionali del Gran Sasso

The setup of the COBRA Demonstrator is installed in the *Laboratori Nazionali del Gran Sasso* (LNGS) in the italian *Abruzzo Massif*, near to L'Aquila in middle Italy. The LNGS is an institution of the *Instituto Nazionale di Fisica Nucleare* (INFN). It is the largest underground laboratory worldwide and was built to allow for large volume underground experiments. The LNGS hosts experiments for dark matter search (DAMA, XENON), astroparticle experiments (BOREXINO, ICARUS, OPERA) and $\beta\beta$-experiments (GERDA, CUORE, COBRA) and many other experiments that require ultra low background conditions in terms of cosmic radiation. A schematic floor-plan of the underground laboratory is given in figure A.1.

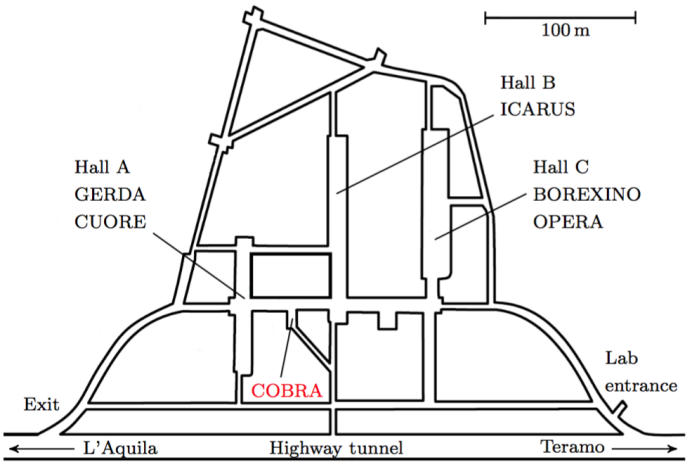

Figure A.1: Floorplan of the LNGS underground facility with the positions of the major experiments and the COBRA Demonstrator setup

A. THE EXPERIMENTAL SETUP OF THE COBRA DEMONSTRATOR

Primary cosmic radiation mainly consist of protons (87%), alpha-particles (12%), heavier ionized nuclei (1%), electrons, photons and neutrinos. The energy of all particles is spread over a wide energy range, reaching up to some TeV. Besides the hardly interacting neutrinos, muons are the main component of the secondary cosmic radiation present at ground level. The highly relativistic muons are created in the earth's atmosphere at energies of up to several GeV. Muons can interact directly or indirectly with experiments. If a muon directly strikes a charge sensitive detector, charge is generated and, depending on detector size and incoming direction, muons can cause saturation of readout electronics or light up scintillation experiments. Muons also generate background by secondary nuclear reactions in the vicinity of experiments. Inelastic scattering of muons in shielding material can generate high energetic neutrons or even charged particle cascades that may interact differently with underground experiments. Hence, for ultra low background experiments a massive shielding of muons is mandatory and an active muon vetoing is advised.
The experimental halls at LNGS are shielded against cosmic radiation by an overburden of approximately 1400 m rock with an average density of $\rho = 2.71 \pm 0.05\,\mathrm{g/cm^3}$, which equals 3.800 m water equivalent (mwe). This results in a reduction of the cosmic muon flux of about 10^{-6} compared to surface level, bringing it down to a value of $j = 1.1\,\mu/(m^2 h)$ or $j = (3.41 \pm 0.01) \cdot 10^{-4} \mu/(m^2 \cdot s)$ [Mir05] [BBB+12].

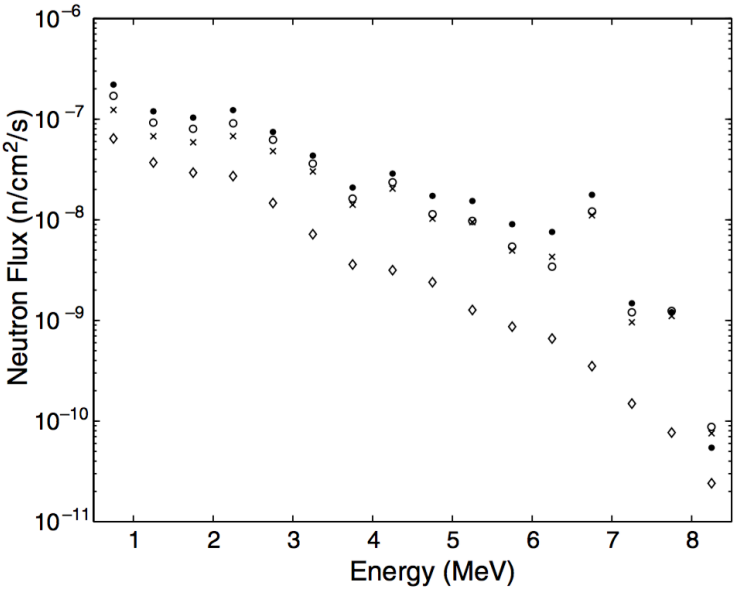

Figure A.2: Neutron flux at the Gran Sasso laboratory, •:hall A, dry concrete; ×:hall A, wet concrete; ◇:hall A, dry concrete, fission reactions only and ○:hall C, dry concrete. Each point shows the integral flux in a 0.5 MeV bin. [WJRvF04]

Despite the enhanced muon shielding, the neutron background is reduced only by 10^{-3} compared to surface level. This type of background is mostly caused by spontaneous

fission of ^{235}U, ^{238}U and ^{232}Th in the surrounding rock. Additionally, (α, n)-reactions, caused by the α-decay of uranium and thorium, generate secondary high energetic neutrons, contributing to the overall background. Neutrons are critical as they can undergo a variety of nuclear interactions with shielding or detector material. They can scatter elastically with the detector material of dark matter experiments, causing similar signatures like predicted weakly interacting massive particles (WIMPs). Furthermore, γ-rays emitted by inelastic neutron-scattering- $(n, n'\gamma)$ or neutron-capture-reactions (n, γ) with prompt or delayed deexcitation can mimic the signature of the $0\nu\beta\beta$-decay. Additionally, unstable daughter-nuclei can be produced, which may generate background in experiments searching for $\beta\beta$-decay. Hence, for neutron-sensitve experiments an adequate neutron shielding is mandatory, too. The total neutron flux is strongly energy depending, falling exponentially from about $j = 10^{-7} n/(cm^2 s)$ in the energy range below $E_n < 1\,\mathrm{MeV}$, down to about $j = 10^{-10} n/(cm^2 s)$ in the range of $E_n > 8\,\mathrm{MeV}$ (figure A.2) [WJRvF04].

A.2 Experimental Setup at the LNGS

The COBRA Demonstrator is assembled from $64\times(1.0 \times 1.0 \times 1.0)\,\mathrm{cm}^3$ CZT detectors in coplanar grid (CPG, section 2.2.3) configuration. It is installed at the LNGS between hall A and B, in the building formerly used by Heidelberg-Moscow Experiment [KKDB$^+$01]. The COBRA Demonstrator is based on the proposal of Zuber [Zub01] and is a successor of studies performed between 2003 and 2009 [KMZ03] [GJK$^+$05] [BBD$^+$07] [DRW$^+$09] [DGJ$^+$09].
In the laboratory space of the COBRA hut a basic clean-room was installed to allow for on-site detector layer assembly and clean setup of the experiment. As no active air filter system was available, the operators were required to wear overalls, face-masks and gloves and to run special procedures for bringing and returning goods into the clean room. Frequent cleaning procedures were performed to remove impurities from surfaces and to prevent contamination of the detector layer assembly station (figure A.3).
The main experiment (figure A.4) and the supply electronics are installed in the laboratory floor, the data acquisition electronics and computing systems are placed in a dedicated and air-conditioned room at the office level (second story). The air condition is needed as flash analogue to digital converters (FADCs), power supplies and computing devices dissipate roughly 3 kW of power. First attempts with the full installation of main electronics in the laboratory floor have shown, that simple radiation cooling is insufficient to keep adequate operational temperatures for the CZT detectors. Temperatures rose up to 30°C even with only 2 detector layers installed and powered. For the laboratory floor no air-condition or air-exchange with the underground laboratory environment is installed. Such an installation would require the transport of fresh air from outside of the mountain into the laboratory to prevent flushing of radon into the experimental environment.

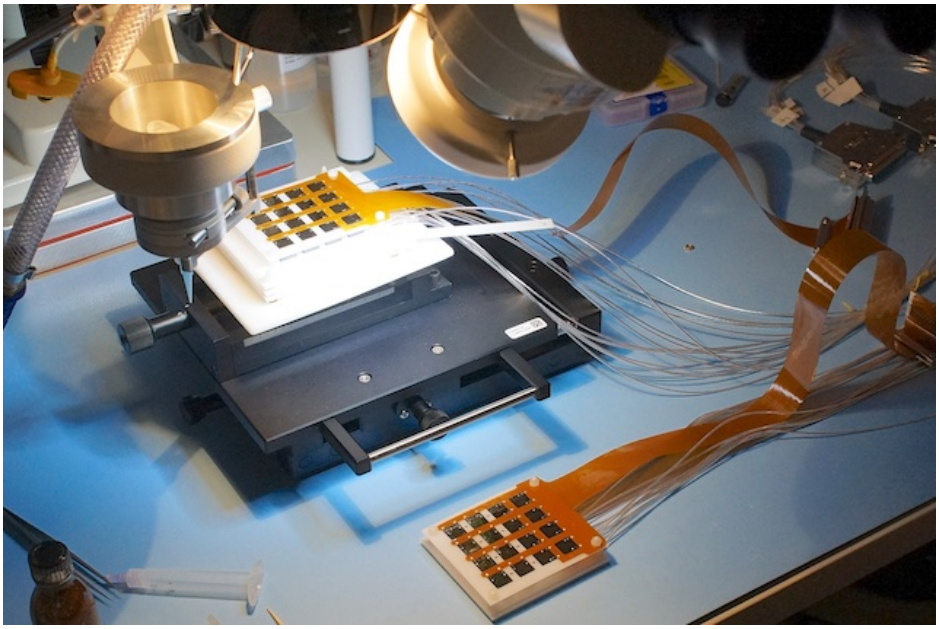

Figure A.3: Detector layer assembly station at COBRA clean room. Layer 2 (front) and Layer 3 (mounted) are under inspection prior to installation. Layer 2 is equipped with RG178 A/U coaxial high voltage supply cables (reddish color), Layer 3 is equipped with coaxial GERDA-HV cables (silver color) with improved background and noise properties.

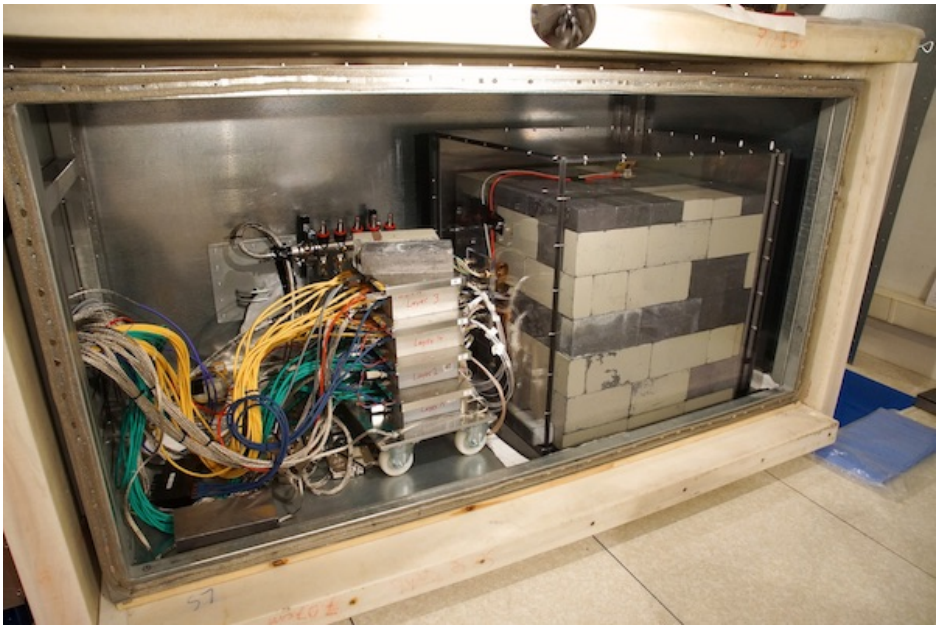

Figure A.4: The final setup of the COBRA Demonstrator experiment at LNGS after the installation of all detector layers in November 2013. The lead castle is housed in the polycarbonate box. Only the front plate of the Farraday cage and the front plate of the neutron shield is removed.

A.3 Shielding of the COBRA Demonstrator Setup

The COBRA Demonstrator comprises a complex shielding structure, consisting of multiple layers for shielding of different particles. The innermost constructional and shielding assembly of the COBRA Demonstrator is the Nest (figure A.5). The Nest contains

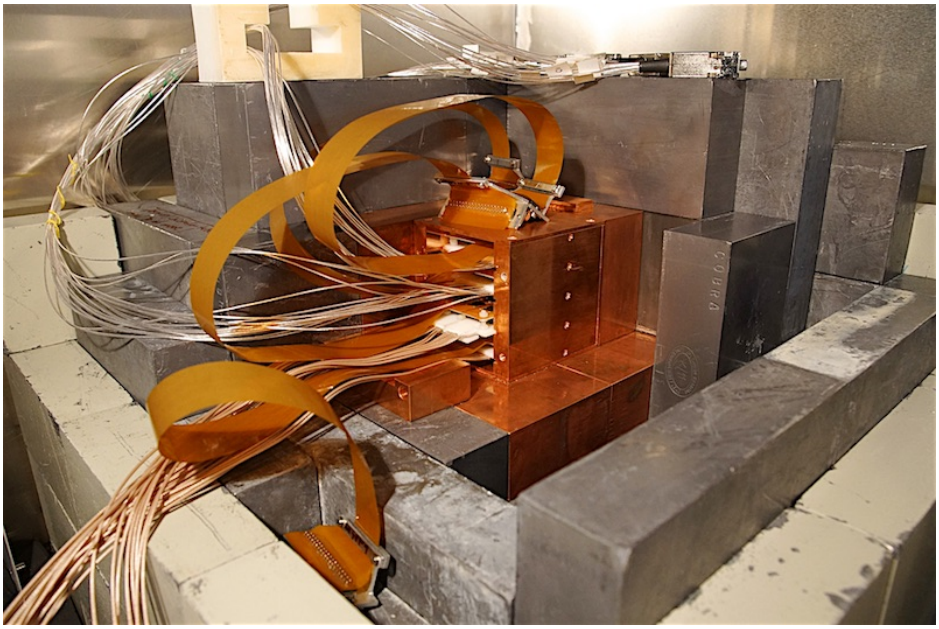

Figure A.5: View of the Nest with all four detector layers in place. The lead castle and copper shielding is partially dismantled. The flat brown cables are the signal carrying Kapton wires. The high voltage is supplied by thin coaxial cables.

the 64 detectors, that are installed in 4 layers, equipped with 16 detectors, each, and screens it from γ- and X-rays. The detector layer holding structure in the Nest is made of *ultra-pure oxygen-free high conductivity* (OFHC) electroplated copper as it is an intrinsic radio-pure material of great stability and good mechanical properties for fabrication. The first shielding layer around the Nest is made of 5 cm thickness OFHC copper, too. The copper is used to absorb the $E^{Pb}_{K\alpha1} = 74\,\text{keV}$ X-ray emission of lead generated by numerous ionizing interactions in the lead castle. The $E^{Pb}_{K\alpha1}$ lies clearly above the COBRA Demonstrator detection threshold of $E_{det} \sim 60\,\text{keV}$ and can affect the measurement of the low energetic ^{113}Cd spectrum. Copper effectively screens X-rays originating from ionizing radiation interacting in the lead castle, while copper itself emits low energetic X-rays at $E^{Cu}_{K\alpha1} = 8\,\text{keV}$.
The Nest is installed in the $(60\times60\times60)\,\text{cm}^3$ lead castle, which acts as a massive γ-shield. The lead castle is made from different lead qualities, contains a cable feed trough chicane and calibration tubes for calibration purposes feeding into the copper Nest. The innermost lead layer is made of 5 cm thick *ultra low activity lead* (ULA-lead) that contains less than $A = 3\,\text{Bq/kg}$ of ^{210}Pb. The three outermost layers are made of

15 cm thick standard lead that has been stored underground for decades and has been used at Heidelberg-Moscow experiment already (figure A.6). To prevent open lines of

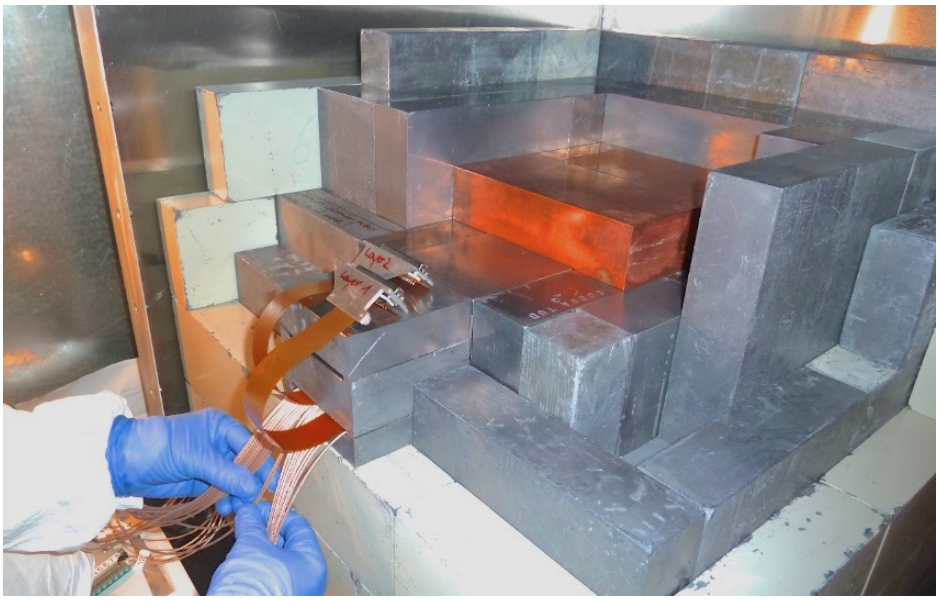

Figure A.6: Partly assembled lead castle with Layer1 and Layer2 installed. Signal and high voltage cables are fed trough the γ-chicane.

sight, the lead bricks are moved by half a pitch from layer to layer, which allows to screen the hems with the subsequent shielding layer. In this setup, the thickness of the shielding is at least 20 cm lead plus 5 cm copper in each direction. The cable feed trough chicane for high voltage supply and data output is made from two s-shaped chicaneries that effectively screen direct photon interaction from the outside.
For calibration purpose five calibration tubes are implemented as well. The tubes consist of five 4 mm Teflon-tubes that are placed above, between and below the detector layers. The feed trough of the tubes is complex as it must be accessible from the laboratory environment and has to reach right into the Nest without deterioration of the different shielding structures. Therefor, it has to pass the neutron shield, the electromagnetic shielding (described below), the lead and copper shielding on a curved way and finally ends between the detector layers. During installation it had to be assured, that the bending radius of the tubes was not exceeded as kinking the tubes would have created an impassable point for the cable mounted calibration sources (figure A.7). For calibration purposes ^{228}Th and ^{22}Na sources were used.
Another important part of the complex shielding structure of the COBRA Demonstrator is the radon shield. Radon is a noble gas that diffuses easily through many materials and it can reach the COBRA detectors, even in the Nest, if no precaution is held. The radioactive ^{222}Rn is part of the natural ^{238}U decay chain and, hence, all over present in nature. The half-life of ^{222}Rn is $T_{1/2} = 3.8$ d, its Q-value is $Q_{222Rn} = 5.59$ MeV and it decays by α-emission. It decays via ^{218}Po, ^{214}Pb, ^{214}Bi, ^{210}Tl, ^{210}Pb, ^{210}Bi, ^{210}Po and

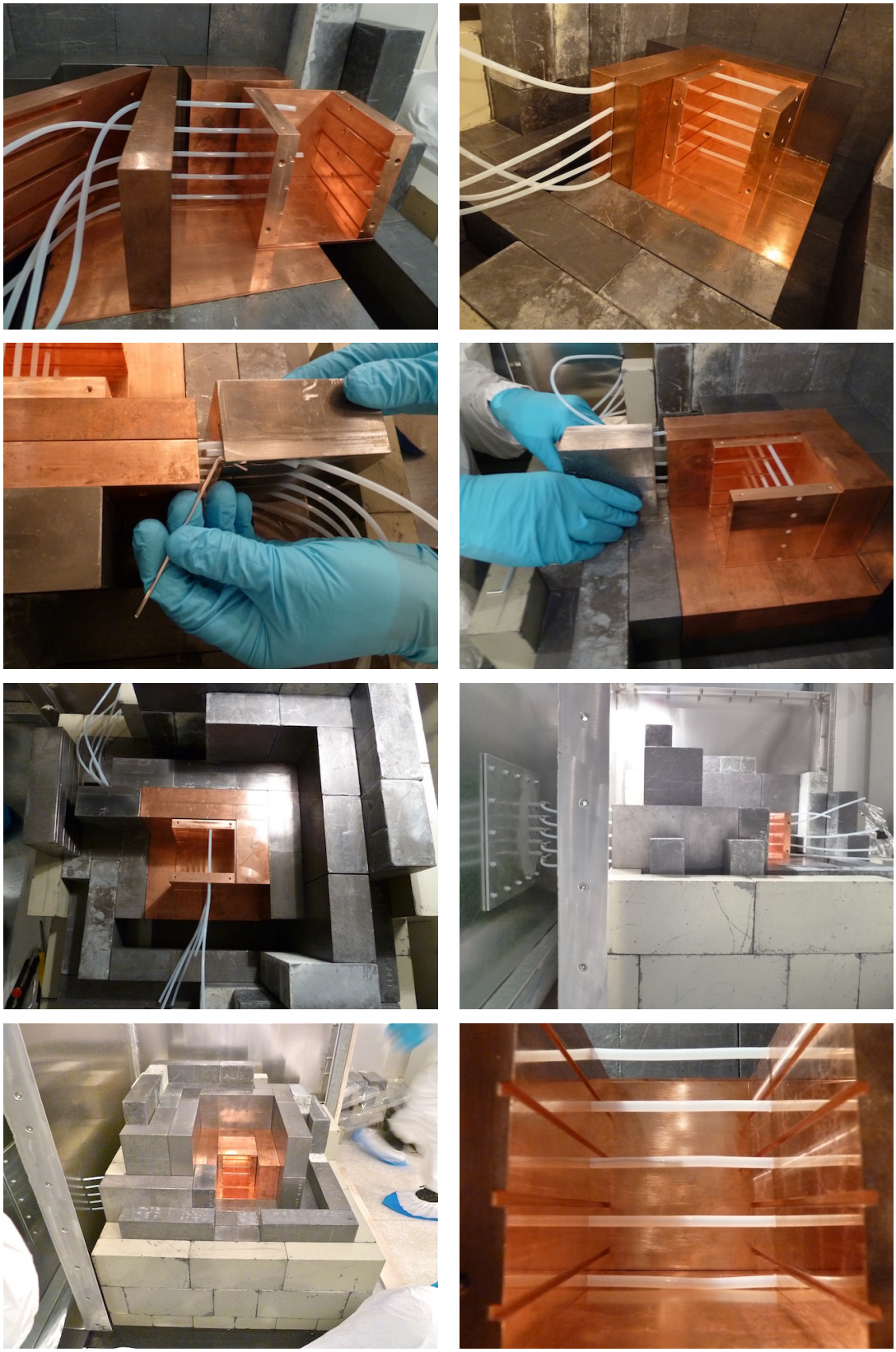

Figure A.7: Installation of the calibration tubes at COBRA Demonstrator. Lower right: calibration source in center position inserted.

^{206}Tl to stable lead ^{206}Pb. As all mentioned isotopes but the ^{206}Pb are radioactive, too, they generate background in the vicinity of the detectors, and it must be prevented that ^{222}Rn gets into the Nest and onto the detectors. To avoid radon diffusion into the COBRA Demonstrator, two different approaches are used. The first approach was to weld the whole lead castle into a radon tight, metallized foil and to continuously flush the setup with evaporated nitrogen. The liquid nitrogen is supplied by a dewar vessel, which is placed outside of the laboratory environment and has to be refilled regularly, roughly every two weeks. The liquid nitrogen is evaporated at a typical rate of 5 l/min and is fed by tubes into the COBRA Demonstrator setup. To avoid infiltration of radon into the setup if the nitrogen supply fails, a glycerin bubbler is installed in the tubing. The evaporation of the nitrogen can be adjusted by a remote controlled heater element in the dewar. The setup proved to be very airtight, as even the low flux of the nitrogen evaporation was sufficient to inflate the foil to a significant pressure (figure A.8).

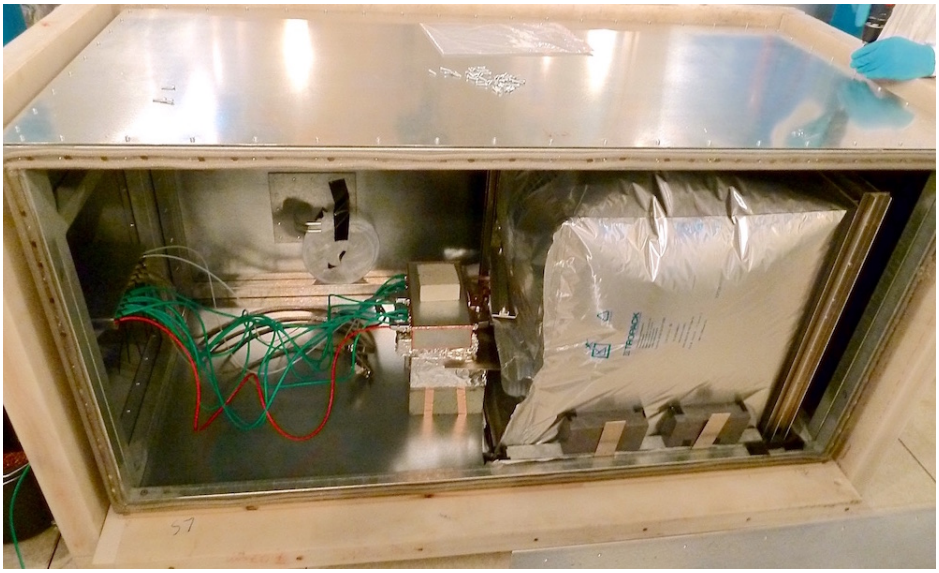

Figure A.8: View into the COBRA Demonstrator setup after installation of Layer1 in September 2011. The first version of the radon shield is based on metallized, gas tight foil. Inflation of welded foil due to nitrogen flushing. The galvanized steel sheets forming the electromagnetic shielding of the setup.

Nevertheless, the metallization of the foil and the feed through of the unshielded signal cables formed a capacitance that caused electrostatic noise at the very sensitive signal path between the detectors and the preamplifiers. With the installation of Layer3, it was decided to dismiss the foil approach and to install a polycarbonate radon shielding (figure A.4). To avoid similar charging problems of the polycarbonate sheets, an anti-static version of the base material was installed. The great advantage of this setup over the foil based version is the transparent and easily accessible cable feed trough. It also scaled much better for the supply of the 64 high voltage cables and secured the Kapton wires, that are now fixed at the polycarbonate door. It is necessary to mechanically

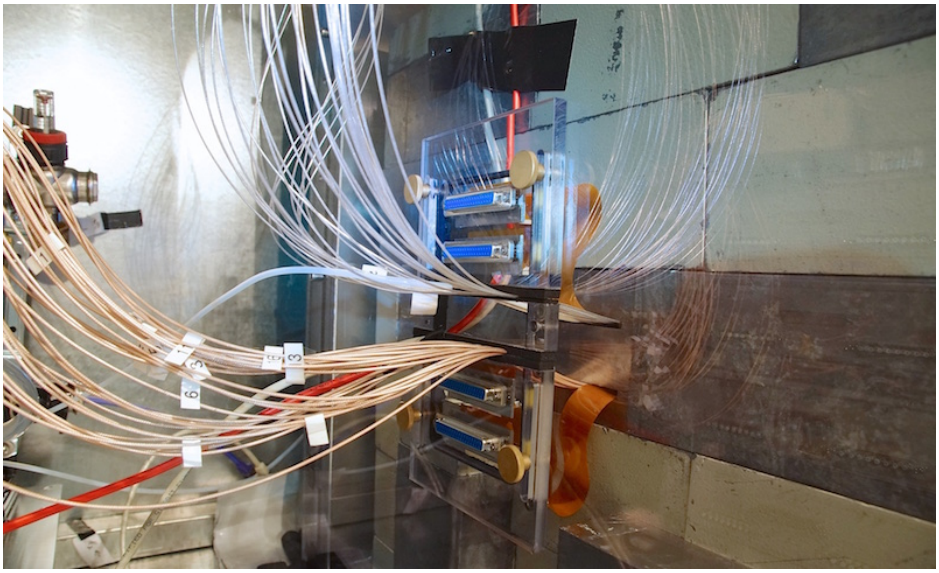

Figure A.9: The cable feed trough of the polycarbonate radon shield. The installation allows to mechanically secure the signal cables that are directly connected to the detector layers from tensile stress. The preamplifier boxes are connected with extension cables to the DC37 connectors (blue ports). The red cable is connected to a temperature, pressure and humidity detector inside the polycarbonate shielding. The Teflon tubing is used to flush the detectors with dry nitrogen.

fixate the Kapton wires, as there is a risk of moving the detector layers by putting tensile stress on the signal wires (figure A.9). However, with the polycarbonate box the air tightness of the welded foil could not be reached again. This can be deduced from the installed humidity sensors that are used to keep track of the nitrogen concentration in the setup. The flushed nitrogen replaces the air and the humidity in the setup. With the fail based radon shield a relative humidity level of $<5\%$ could be reached easily, whereas with the polycarbonate shield only 10% or higher relative humidity is achieved. Nevertheless, the effectiveness of flushing the setup is evident, if the regular refilling of the dewar failed. In this case the background rate rises significantly due to the in-diffusion of radon into the setup and data of runs of such periods have to be dismissed for ultra low background analysis. This proves, that flushing the setup to prevent radon from diffusing into the experiment and to assure ultra low background conditions is mandatory. Furthermore, it is necessary to dry the setup with the permanent nitrogen flushing prior to cool-down, to prevent condensation at the cooling plates (described below) and the preamp boxes.
The COBRA Demonstrator setup has to be shielded from electromagnetic interferences (EMI) as well. The most susceptible part for EMI is the unshielded connection between the CZT detectors and the remote installed preamplifier boxes. The connection between the detectors and the preamplifier boxes is realized by an approximately 50 cm long, plain Kapton wire, that carries the signals of all 16 detectors of a layer in 32 parallel

lines (figure A.3 or A.5). At this Kapton wire, no active amplification is used and the signal can be altered easily as its amplitude is very low. To prevent the signals from the impact of EMI, a massive electromagnetic shielding (EM shielding) is necessary and is installed at COBRA Demonstrator. The EM shielding consists of 2 mm thick galvanized steel sheets that are screwed onto a grounded steel frame (figure A.8). The cable feed through is realized by a chute that is filled with a fine copper granulate to ensure good electric contact to the isolation dismantled cable (figure A.10). The inlet and outlet of the nitrogen flushing and the cooling pipes are also fed through the chute. After the transformation of the charge burst signal into an equivalent voltage amplitude and the amplification of this signal in the preamplifier box, the signal is transmitted to the fast linear amplifier in the upper hut. To prevent EMI during the transmission, the signal is transmitted as a differential signal. The differential signal transmission allows for a correction of electromagnetic disturbances that are injected during transmission.

Figure A.10: The copper chute of the COBRA Demonstrator setup. The electrical isolation of the cables is removed down to the electromagnetic shielding of the cable to ensure good electric contact to the copper granulate. The green and yellow CAT6 cables are used for differential signal transmission of the detector signals, the steel meshed cables carrying the 64 high voltages and grid bias cables for the detector supply. Furthermore, supply cables for the preamplifier boxes, the cable for the pulser signals, for environmental monitoring and the cooling pipes are fed through the chute, too. The neutron shield is removed for this picture.

Another long ranging particle with high potential for background generation is the neutron. Shielding neutrons is necessary, as the COBRA detectors currently are made from natural abundant cadmium. Natural cadmium contains 12.22% of ^{113}Cd, with a cross section of $\sigma \sim 20.000$ barn for thermal neutron capture. The resulting ^{113}Cd(n,γ)^{114}Cd

reaction releases a deexcitation γ-cascade with a total energy release of $E_\gamma = 9042.9\,\text{keV}$. This high energetic γ-radiation is produced in the COBRA detector itself, which clearly has to be avoided. To shield neutrons, the setup is covered with 7.25 cm thick borated polyethylene sheets as outermost shielding layer (figure A.11). The hydrogen

Figure A.11: Removed front plate of neutron shield. Faraday cage is exposed.

rich polyethylene thermalizes high energetic neutrons and the $^{10}\text{B}(n,\alpha)^7\text{Li}$ reaction is used to capture the slowed-down neutrons. ^{10}B has a thermal neutron capture cross section of $\sigma_{(n,\alpha)} \sim 3850\,\text{barn}$. With a relative probability of 80%, the $^{10}\text{B}(n,\alpha)^7\text{Li}$ reaction ends at the ground state, releasing only charged particles from this reaction, whereas with a relative probability of 20% the reaction goes to the first excited state, deexciting with a single $E = 477\,\text{keV}$ γ-photon, which has to be shielded as well.
Another important feature of the COBRA Demonstrator setup is the installation of a dedicated cooling device. The cooling is necessary as the four preamplifier boxes are generating roughly $p = 40\,\text{W}$ of heat next to the lead castle. Since the $d = 7.25\,\text{cm}$ thick polyethylene neutron shield isolates the setup thermally from the lab environment, a slow but continuous build up of heat is observed, such, that the mean temperature of the detectors was higher than the temperature of the laboratory level. Additionally, during operation of Layer1 and Layer2 the main electronics and FADCs was installed in the lower hut, too. The FADCs are a main source of heat dissipation, which led to a significant temperature boost in the lab environment. With the installation of Layer3 it was decided, to move the main electronics to the upper hut into an air-conditioned room. Nevertheless, cooling became necessary, as the detector performance is clearly temperature dependent. First measurements have shown, that the optimum performance in terms of energy resolution can be found around $T_{det} \sim 5\,^\circ\text{C}$ [DMR$^+$09] [ALL06]. For more details on cooled detector performance see section 3.3. The main chiller is placed

outside the lower hut to dissipate the heat into the tunnel environment. The coolant is transferred via isolated pipes into the setup and split to four separate cooling plates. The cooling plates are placed between the preamplifier boxes to remove the generated heat (figure A.12).

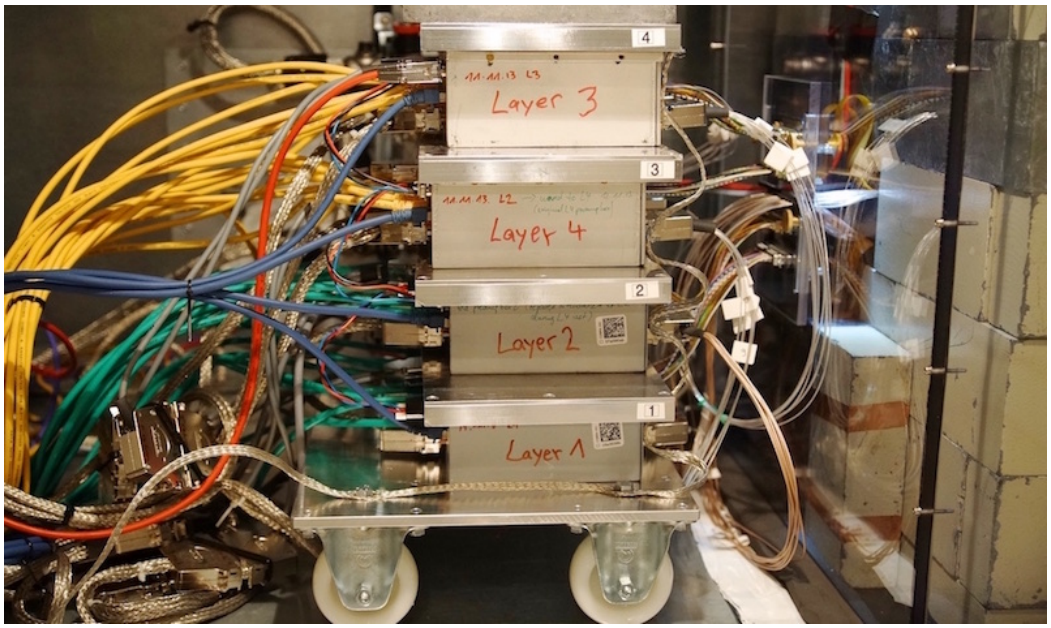

Figure A.12: Stack of the preamplifier boxes (manually labeled) with cooling plates (printer labeled) in between. The preamplifier boxes Layer3 and Layer4 are swapped on purpose. For operational and weight reasons the whole stack is mounted on a roller-board.

Even though, the installation at the LNGS reduces the impact of cosmic muons by a factor of 10^6 compared to surface muon flux, muons are still present and can be detected. The high energy of the muon makes it to a minimum ionizing particles (MIP). A MIP can pass the whole experiment without a major interaction and still generate signal along its path. The granularity of COBRA allows to identify and discard muon interactions as time-coincident signals in multiple detectors. To identify such time-coincident multi detector interactions, the data readout between the detectors has to be time-synchronous at the ns-time scale. In an upgrade of the experiment a pulser system was installed, injecting time synchronization pulses simultaneously into all preamplifiers of the setup. These pulses are used to synchronize the slightly drifting clocks of the FADCs during data acquisition. With time synchronous data of all detectors the experiment itself can act as its own active muon veto system.

A.4 The Electronics of the COBRA Demonstrator Setup

The readout electronics of the COBRA Demonstrator setup basically consist of three parts: the preamplifier, the linear amplifier and the digitizer. The preamplifier circuits are commercially available CREMAT CR110 charge sensitive preamplifiers that covert the charge burst signal of the detector into a voltage equivalent signal. The simplified equivalent circuit diagram and the pin-out of the preamplifier are shown in figure A.13.

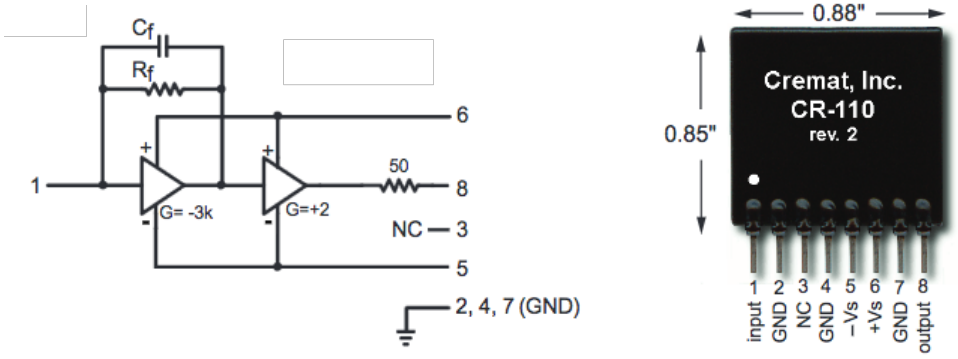

Figure A.13: Cremat CR110 simplified equivalent circuit diagram

The CR110 features an amplification of $A = 1.4\,\mathrm{V/pC}$, requiring a post amplification for input range matching of the digitizers. The noise of the CR110 is $C = 0.03\,\mathrm{fC}$ which equals $\delta E = 2.4\,\mathrm{keV}$ (FWHM) for an attached CZT detector, which is about 8% the energy resolution of the best CZT detectors in use. The CR110 specifications are listed in figure A.14. The best detectors in use show an energy resolution of about 30 keV at 2.8 MeV, hence, the peak widening due to preamplifier noise is low. The preamplifier boxes are designed to support a fully equipped detector layer with 16 detectors. To support a full detector layer, 32 CR110 devices for 16 CA and 16 NCA channels, 16 independent grid bias voltages and 16 independent high voltages are required. To suppress cross talk between the preamplifiers a special metal shielding is installed (figure A.15).
The high voltages and grid biases are also supplied via the preamplifier box, whereas the high voltages are additionally filtered by an RC low-pass filter. For signal integrity reasons a floating, differential transmission of the signal between the preamplifiers and the linear amplifiers is used. The connection between the preamplifier boxes and the linear amplifiers, is established via conventional CAT6 network cables with RJ45 jacks. CAT6 cable is designed for high frequency signal transmission of up to f=250 MHz on four independently, shielded twisted pair wires per cable. This allows for the transport of four individual CA and NCA signals per cable and, hence, the support of two independent detectors. The linear amplifiers are installed in a 19 inch standard NIM rack in the upper hut, that also houses the suplementary electronics (figure A.20). The amplification factor of the linear amplifiers is remotely adjustable via serial peripheral

Specifications

Assume temp =20 °C, V_s = ±6.1V, unloaded output

	CR-110	units
Preamplification channels	1	
Equivalent noise charge (ENC)*		
ENC RMS	200	electrons
	0.03	femtoCoul.
Equivalent noise in silicon	1.7	keV (FWHM)
Equivalent noise in CdZnTe	2.4	keV (FWHM)
ENC slope	4	elect. RMS /pF
Gain	1.4	volts / pC
	62	mV / MeV(Si)
Rise time **	7	ns
Decay time constant	140	µs
Unsaturated output swing	-3 to +3	volts
Maximum charge detectable per event	1.3×10^7	electrons
	2.1	pC
Power supply voltage (V_s)		
maximum	V_s = ±13	volts
minimum	V_s = ±6	volts
Power supply current (pos)	7.5	mA
(neg)	3.5	mA
Power dissipation	70	mW
Operating temperature	-40 to +85	°C
Output offset	+0.2 to -0.2	volts
Output impedance	50	ohms

* Measured with input unconnected, using Gaussian shaping amplifier with time constant =1 µs. With a detector attached to the input, noise from the detector capacitance, leakage current, and dielectric losses will add to this figure.

** Pulse rise time (defined as the time to attain 90% of maximum value) has a linear relationship with input capacitance. Value cited in the table assumes zero added input capacitance. To calculate pulse rise time for practical situations, use the equation: $t_r = 0.4\ C_d + 7$ ns, where t_r is the pulse rise time in ns, and C_d is the added capacitance (e.g. detector capacitance) in pF. Keep in mind that others factors within the detection system may further limit this value.

Figure A.14: Cremat CR110 specifications [Cre17]

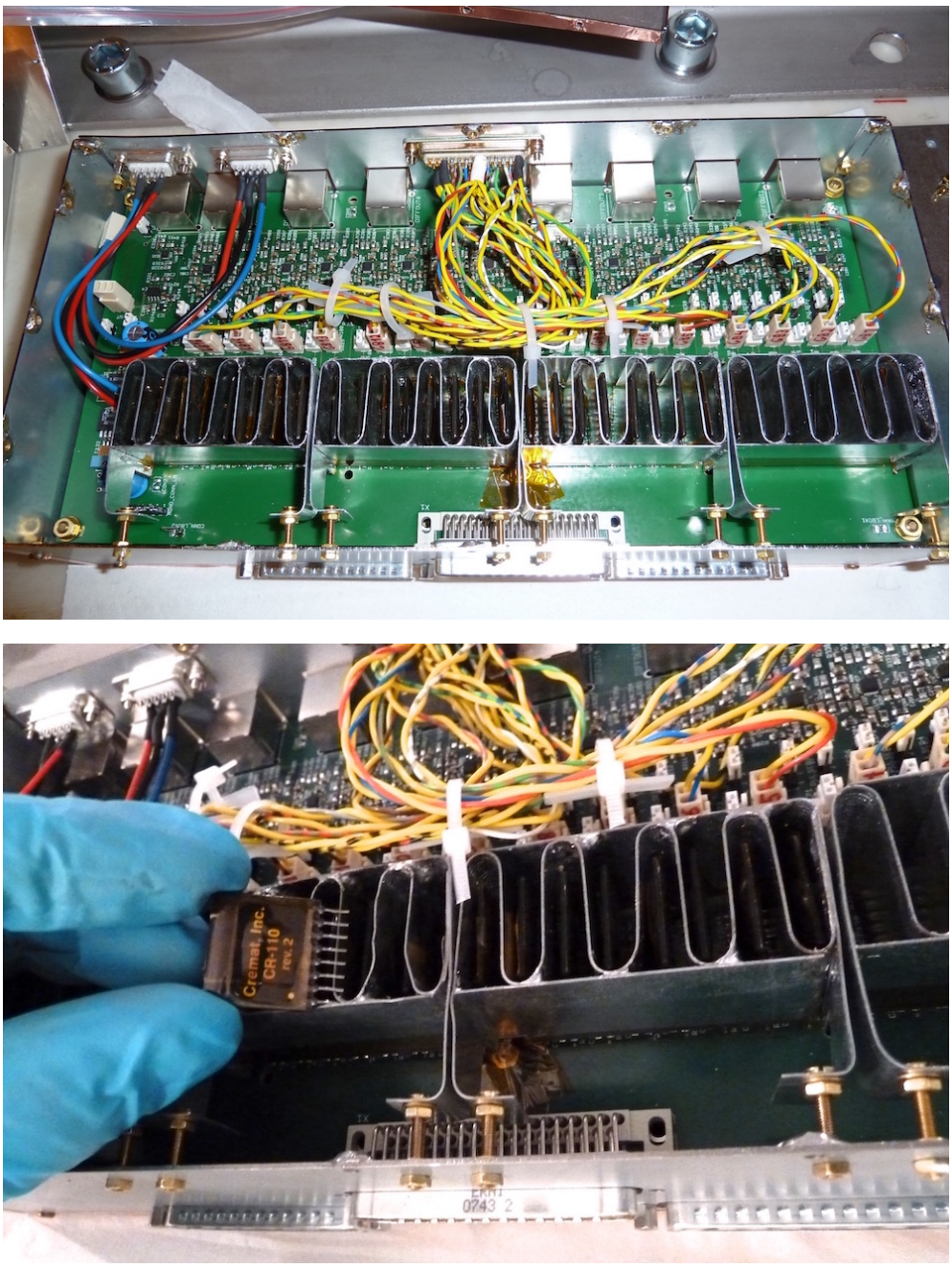

Figure A.15: Above: Opened and fully equipped preamplifier box. Yellow cables are for grid bias supply. The shielded cubes at the upper end are the RJ45 jacks. Below this PCB, the RC low pass filter for the high voltage supply is installed (not to be seen). Below: Installing CR110 into cross talk shielding.

interface (SPI) controller. This allows for a precise adjustment of the linear amplifier output to the input range of the digitizers.
For synchronization and stability tracking an external high precision pulser *Berkeley Nucleonics PB5* is installed. The pulser signal is multiplied, differentially transmitted to lower hut, fed into the preamplifier boxes and capacitively coupled to the inputs of each CR110 preamp. The output of the pulser is script controlled and periodically injects synchronization and stability tracking pulses into the preamplifiers. To avoid a misinterpretation of the pulser signal, the injected pulses are tagged as `flag_injected_pulse` in the recordings. The synchronization pulse is injected every 10 minutes, the stability tracking pulses are injected every 230 min. This frequency was chosen, as the runs are typically 4 hours long and the pulser system is not synchronized with the data acquisition system (DAQ). With the 230 min approach it is guaranteed, that at least one stability tracking burst is injected into each single run. The stability tracking pulses are bursts of 100 injections in a short time window ($t < 10\,\text{sec}$), the time synchronization pulse is a single injection (figure A.16).

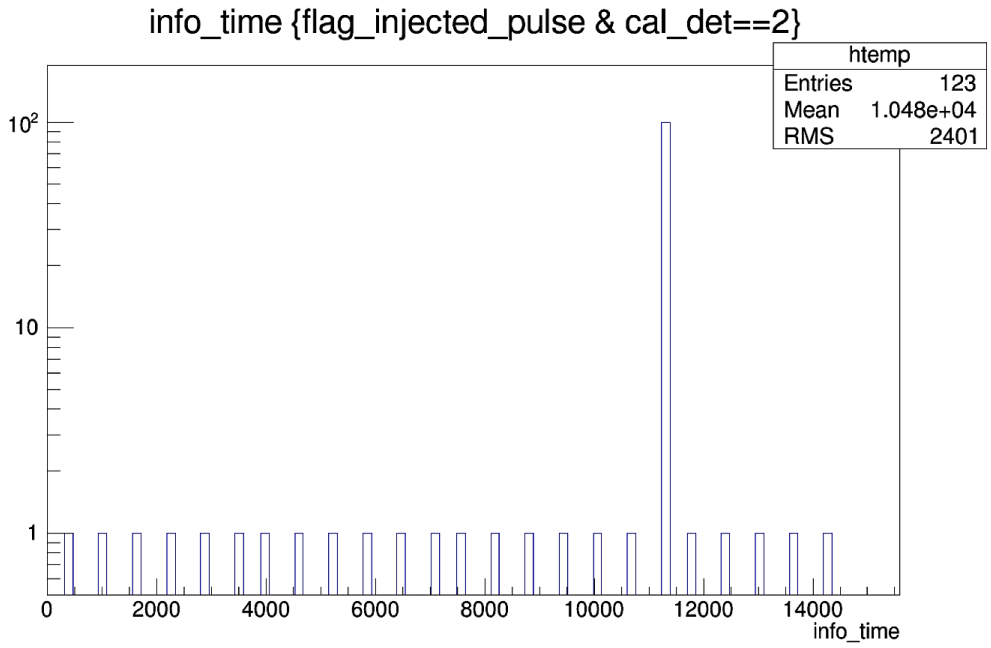

Figure A.16: The pulser timing used for data taking periods on COBRA Demonstrator. Every 10 min a single injection is performed for time synchronization purposes. Every 230 min a burst of 100 injections is performed for stability tracking purposes.

For digitalization of the analogue input signals, the COBRA Demonstrator DAQ system is equipped with 16 *Struck SIS 3300* flash analogue to digital converter devices (FADC, figure A.17). Each FADC features eight single ended input channels with alternating inputs for the CA and NCA channels. The channel assignment is hard coded and must be double checked prior to data taking. A check of the assignments is necessary, as the CA and NCA channels of some detectors are swapped, such, that energy resolu-

tion is best. The FADC modules are installed in Versa Module Eurocard bus crates (VMEbus) and are controlled by a VME controller system that provides the digitized data to the COBRA-DAQ system via ethernet. The sampling rate of the FADCs is

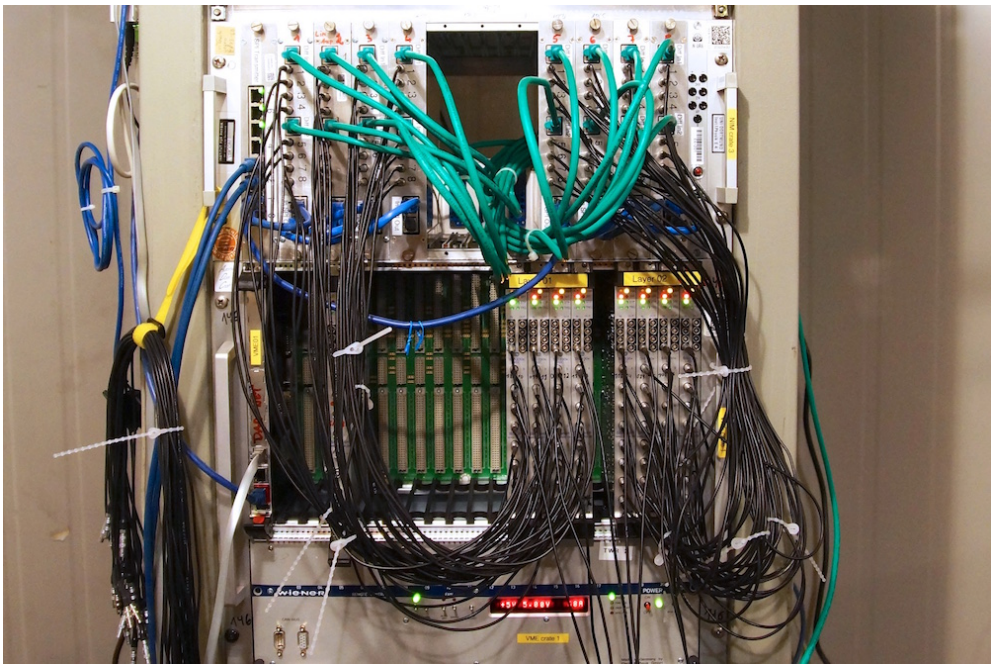

Figure A.17: Linear amplifiers (upper row) and corresponding FADCs for Layer1 and Layer2 support. Connection between linear amplifiers and FADCs is established with coaxial Lemo cables (connector: LEMO FFA.00.250.CTAC29, RG174 cable).

$f_s = 100\,\text{MHz}$, the physical resolution is 12-bit and a triggered event is recorded for 1024 samples. The FADCs are continuously sampling the inputs. If the individually adjusted trigger threshold is exceeded, 512 samples before and 512 samples after the trigger are stored. At 100 MHz sampling frequency this results in a 10.24 µs record per event, which guarantees enough head space for pre- and post-trigger baseline sampling. The longest rise time of a detector signal is in the order of 1 µs, a decay correction for the post-trigger level is applied in the evaluation routines. The pulse shape records are stored on the COBRA-DAQ server. The COBRA-DAQ server is the pivot of the whole experiment. It provides remote access and control abilities for every subsystem of the COBRA Demonstrator experiment. For security reasons it runs in a virtual machine, such, that regular backups of the machine can be stored. During data taking, recorded data is stored on mirrored COBRA-DAQ hard discs. Between data taking runs, the raw data is copied to external servers for backup and processing.
The high voltage, grid bias and low voltage power supply for the COBRA Demonstrator setup is performed with a WIENER-MPOD-crate (figure A.18) and dedicated power supply modules. The MPod is a universal infrastructure to support remote controlled

power supplies for nuclear physics experiments. For the COBRA Demonstrator experiment it houses three types of modules (table A.1).

Figure A.18: MPod crate with installed high voltage modules (EDS 20 130n, slot 1 & 2), grid bias modules (EDS 20 005n, slot 4 & 5) and low voltage modules (Wiener-LV-Modul 8008). Low voltage module supplies the preamplifier boxes and the dewar heater.

Table A.1: Power supply modules installed in MPod crate at laboratory level

slot	device	support	description
1	ISEG EDS 20 130n	high voltage	32×(-3) kV/500 μA, Layer1 & Layer2
2	ISEG EDS 20 130n	high voltage	32×(-3) kV/500 μA, Layer3 & Layer4
3	Wiener-LV-Modul 8008	low voltage	8×8 V/5 A, voltage ripples <3 mVpp
4	ISEG EDS 20 005n	grid bias	32×(-500) V/1 mA, Layer1 & Layer2
5	ISEG EDS 20 005n	grid bias	32×(-500) V/1 mA, Layer3 & Layer4

The adaptation of the 40-pin REDEL connector of the ISEG EDS 20 130n and ISEG EDS 20 005n modules to the 4×8W8-connectors of the custom made high voltage and grid bias cables is performed in electromagnetically shielded converter boxes. Those *golden boxes* are successors of less shielded aluminum boxes, that were replaced because of its high voltage ripple injection that affected the data quality (figure A.19). The applied high voltages and grid biases are adjusted remotely and can be set independently for each detector. The specific operating voltages are determined prior the installation in laboratory experiments for each detector, accordingly. The mains connection of the experimental setup is completely backed up with uninterruptible power supplies (APC Smart UPS RT1000 & RT 3000). The UPS are implemented as online UPS, which

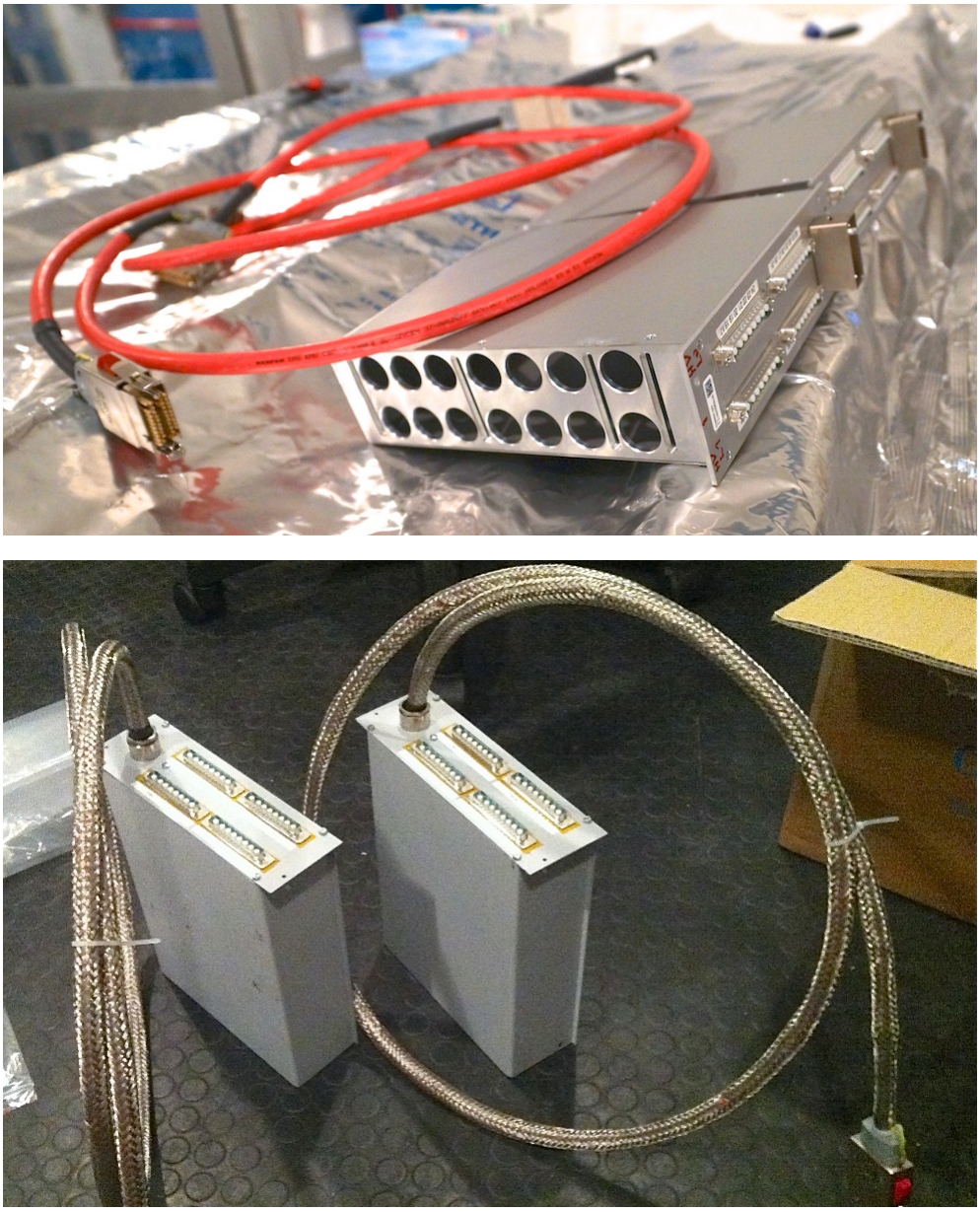

Figure A.19: Upper picture: first version of 40-pin REDEL to 4×8W8-connectors converter box that were replaced because of bad EMI shielding properties. The aluminum housing and open panel sheets allowed electronic interferences to couple into the high voltage supply and to deteriorate the detector signal. Lower picture: The replacement boxes (*golden boxes*) feature a massive EMI shielding that improved the signal quality greatly. The 40-pin REDEL connector is removed and the high voltage cables are now directly connected to the 8W8 outlet. Furthermore, the completely closed housing was made from galvanized steel to shield electromagnetic interferences.

means, that the mains input is in a first step rectified and charged to the batteries. In a second step, an alternating voltage is generated from the direct current of the batteries and supplied to the experimental equipment. This ensures a galvanic separation of the experimental setup from the mains connection of the LNGS and a high quality of supplied power, as voltage spikes or dropouts of the mains supply are completely filtered by the UPS. Several complete mains fails at the LNGS could be bridged by means of the installed UPS with no effect on the running measurement. In such cases the high power consumption of the whole setup of about 3 kW is critical. The installed three UPS units are designed to bridge a mains dropout of roughly 30 minutes. The operators are informed via email of power interruptions, such, that counter measures can be taken. Voltage dropouts are critical, as prior and after data taking periods pre- and post-calibration runs are necessary, to keep track of possible drifts during the runs. All supplied devices are connected to an APC Switched Rack PDU, a remote controlled power distribution unit. This allows for a precise power consumption tracking of the devices and offers the ability to remotely shutdown and restart devices in case of fails. To assure a complete galvanic separation of the experimental setup, the network connections to the LNGS network needed to be separated, too. This is done by using an additional network switch between the LNGS network (dirty switch) and the COBRA network (clean switch). The connection between both switches is established via high speed optical link.

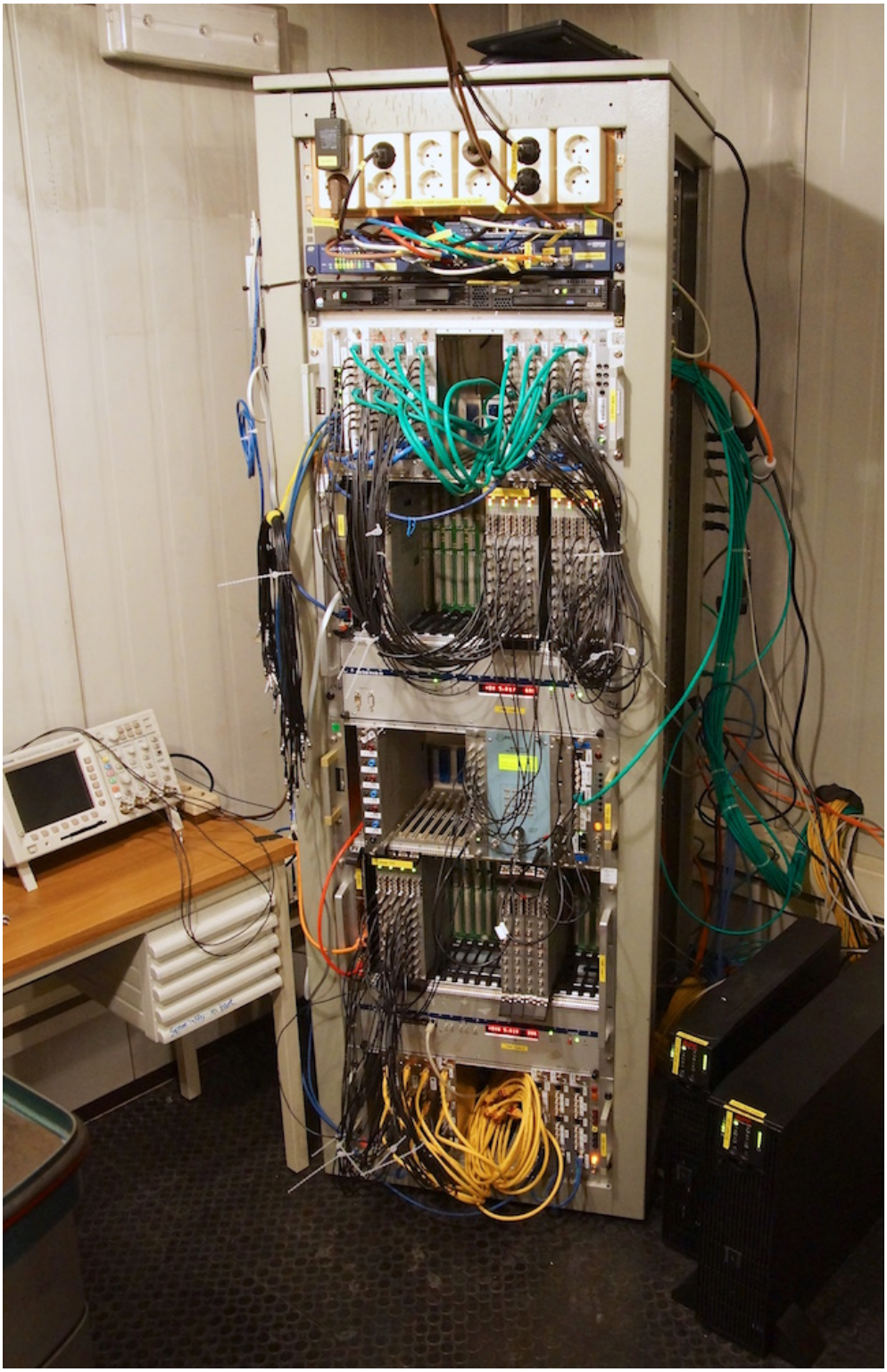

Figure A.20: The fully equipped DAQ rack in the upper hut. Installed are the linear amplifiers, digitizers, PB5-pulser, SPI controller, network switches and DAQ server system. At bottom right the uninterruptible power supplies (UPS) are installed.

A. THE EXPERIMENTAL SETUP OF THE COBRA DEMONSTRATOR

Appendix B

Follow-up Operation of the 2D-Scanning Test Rig

The 2d scanning test rig was designed to support multiple applications. The total accessible range of the X-Y-motors is about 10×10 cm, allowing for wide fields of application. The collimator is easily removable and can be replaced by other devices, needing precise positioning.

B.1 Analysis of the Localized Detector Response of the COBRA-XDEM Detectors

A very successful follow-up operation of the test rig was the investigation of the localized detector response of the (20×20×15) mm^3 quad grid detectors (figure B.1) for COBRA-XDEM and the development of new evaluation procedures for this type of detectors by Rohatsch [Roh16]. This was necessary as the design of the quad layout required a completely new evaluation procedure as the signals of the single sub-detectors have to be analyzed in a combined approach. The collimated irradiation of the 2d scanning test rig was perfectly suited for this investigation. The highly collimated γ-beam allows for a selective irradiation of a single sub-detector in a well controlled way. With this setup it is possible, to investigate the number of one-, two- and three-sector events in dependence on the point of irradiation. For this analysis, the detector is irradiated from the anode-side (top down) and the conventional COBRA DAQ was equipped with an adapted data read-out scheme. Now, all four sub-detectors are red out simultaneously, if one sub-detector triggers an event. As the detector consists of a single (20×20×15) mm^3 crystal and the sub-detectors (or sectors) are only defined by the deposited grid, the interaction of events close to the boundaries are of special interest. To analyze such events, the sub-detectors and the resulting pulse-shapes in the adjacent sectors have to be analyzed simultaneously. In figure B.2 the distribution of the intensity for one-, two- and three-sector events are displayed for two different electrical configurations of the same detector. It seems, that the number of detected two-sector events depends on

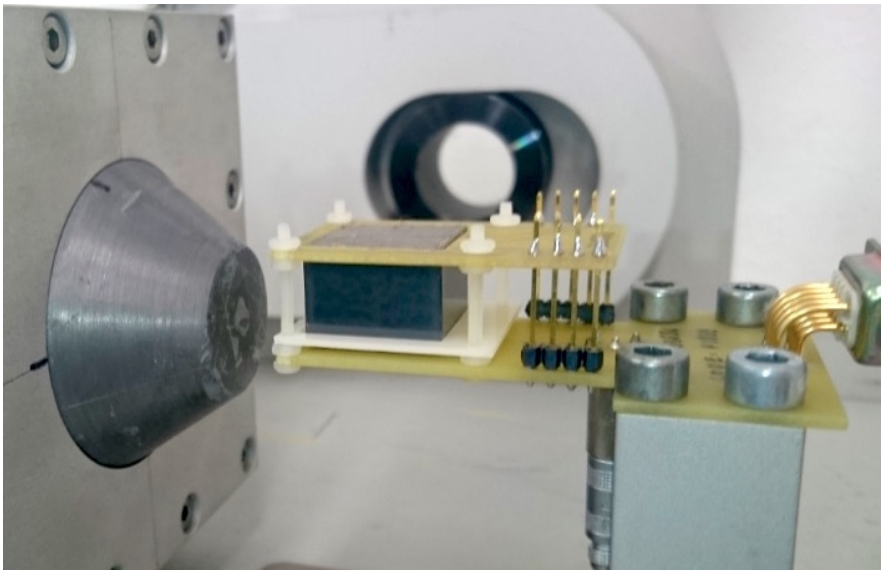

Figure B.1: The $(20\times20\times15)\,\mathrm{mm}^3$ COBRA-XDEM detector placed in front of the collimator in the 2D scanning test rig. Only an adaption of the detector mounting was necessary to support the analysis of the larger detectors.

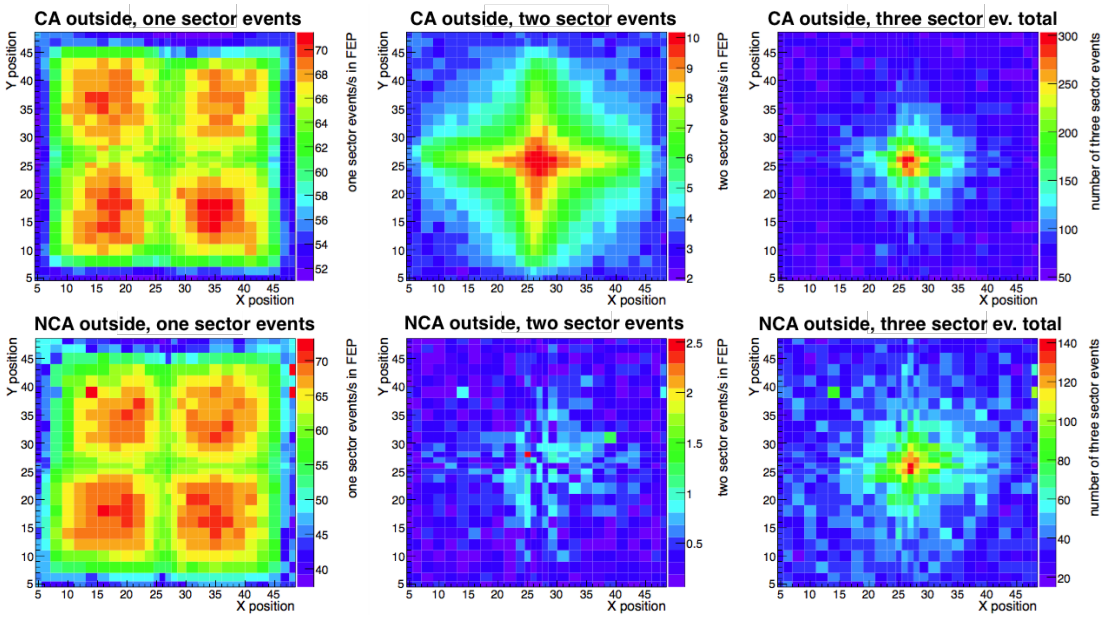

Figure B.2: Distribution of one-, two- and three-sector events for the same detector in dependence on CA/NCA orientation. Upper row: CA outside, lower row: NCA outside. Left: one-sector events, middle: two-sector events, right: total number of three-sector events.

the electrical field orientation of the grid: CA outside versus NCA outside. This result is unphysical, as the interaction of the scattered photons are independent on electrical configuration of the detector. The analysis of this effect revealed, that this behavior can be explained by charge-sharing effects at the boundaries of the four sub-grids, if the NCA is outside and the inner electrode is in CA configuration.

B.2 CCE Mapping of the COBRA-XDEM Detectors

The test rig also allows for the above described 2d-mapping of the CCE of the (20×20×15) mm^3 quad-grid detectors (figure B.3). With this mappings, the CCE performance of the

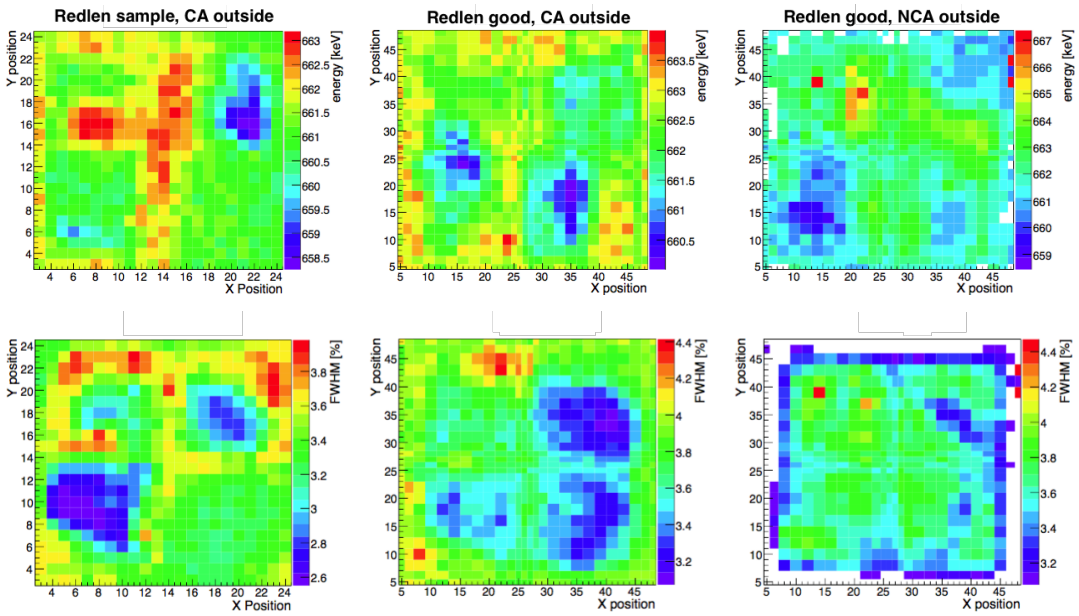

Figure B.3: CCE mappings (upper row) and corresponding energy resolution mappings of two different quad grid detectors (Redlen sample detector and Redlen good detector) in different electrical CA/NCA-configuration.

sub-detectors could be compared with the achieved energy resolution. Interestingly, the pattern of the variations of the CCE does not correlate with the pattern of the resulting energy resolution. The work on the interpretation and investigation of multiple interactions in the quad grid detectors is still ongoing [Roh16], [The17], [Arl17].